CHARACTERIZATION OF NANOSCALE REINFORCED POLYMER COMPOSITES AS ACTIVE MATERIALS

A Dissertation

by

SUJAY DESHMUKH

Submitted to the Office of Graduate Studies of
Texas A&M University
in partial fulfillment of the requirements for the degree of

DOCTOR OF PHILOSOPHY

December 2010

Major Subject: Aerospace Engineering

Characterization of Nanoscale Reinforced Polymer Composites as Active Materials

CHARACTERIZATION OF NANOSCALE REINFORCED POLYMER COMPOSITES AS ACTIVE MATERIALS

A Dissertation

by

SUJAY DESHMUKH

Submitted to the Office of Graduate Studies of
Texas A&M University
in partial fulfillment of the requirements for the degree of

DOCTOR OF PHILOSOPHY

Approved by:

Chair of Committee,	Zoubeida Ounaies
Committee Members,	Xing Cheng
	Hong Liang
	Anastasia Muliana
Head of Department,	Dimitris Lagoudas

December 2010

Major Subject: Aerospace Engineering

ABSTRACT

Characterization of Nanoscale Reinforced Polymer Composites as Active Materials.

(December 2010)

Sujay Jaysing Deshmukh, B.E., University of Pune, India;

M.S., Texas A&M University

Chair of Advisory Committee: Dr. Zoubeida Ounaies

Single walled carbon nanotube (SWNT)-based polymer nanocomposites have generated a lot of interest as potential multifunctional materials due to the exceptional physical properties of SWNTs. To date, investigations into the electromechanical response of these materials are limited. Previous studies have shown marginal improvements in the electromechanical response of already electroactive polymers (EAPs) with addition of SWNTs. However, in general, disadvantages of EAPs such as high actuation electric field, low blocked stress and low work capacity remain unaddressed.

This dissertation targets a comprehensive investigation of the electromechanical response of SWNT-based polymer nanocomposites. Specifically, the study focuses on incorporating SWNTs in three polymeric matrices: a non-polar amorphous polyimide (CP2), a polar amorphous polyimide ((β-CN) APB-ODPA), and a highly polar semicrystalline polymer (PVDF). In the first step, emergence of an electrostrictive response is discovered in the non-polar polyimide CP2 in the presence of SWNTs. Transverse and longitudinal electrostrictive coefficients are measured to be six orders of

magnitude higher than those of known electrostrictive polymers like polyurethane and P(VDF-TrFE) at less than $1/100^{th}$ of the actuation electric fields.

Next, the effect of the polymer matrix on the electrostrictive response is studied by focusing on the polar (β-CN) APB-ODPA. A transverse electrostriction coefficient of 1.5 m^2/MV^2 is measured for 1 vol% SWNT- (β-CN) APB-ODPA, about twice the value found for 1 vol% SWNT-CP2. The high value is attributed to higher dipole moment of the (β-CN) APB-ODPA molecule and strong non-covalent interaction between the SWNTs and (β-CN) APB-ODPA matrix.

Finally, polyvinylidene fluoride (PVDF) matrix is selected as a means to optimize the electrostrictive response, since PVDF demonstrates both a high dipole moment and a strong non-covalent interaction with the SWNTs. SWNT-PVDF nanocomposites fared better than SWNT-CP2 nanocomposites but had comparable response to SWNT-(β-CN) APB-ODPA nanocomposites. This was attributed to comparable polarization in both the polar nanocomposite systems. To maximize the SWNT-PVDF response, SWNT-PVDF samples were stretched leading to increase in the total polarization of the nanocomposite samples and decrease in the conductive losses. However, the dielectric constant also decreased after stretching due to disruption of the SWNT network, resulting in a decrease of the electrostrictive response.

DEDICATION

To my family, friends and well-wishers

ACKNOWLEDGEMENTS

I would like to take this opportunity to acknowledge all the people who have made this dissertation possible. The first person that deserves a big acknowledgement is my advisor Dr. Zoubeda Ounaies. She has been an exceptional mentor and guide through the last six years of my graduate studies. A supportive and knowledgeable advisor is essential for success in research for a graduate student. Dr. Ounaies has advised me over the years with patience and unwavering support and I will always be indebted to her for that.

I would also like to acknowledge all the past and present members of the electroactive materials characterization laboratory: Sumanth Banda, Atheer Almasri, Dr. Ricardo Perez, Sanjay Kalidindi, Amira Barhoumi, Payam Khodaparast, Hessene Ben Atitallah, Nirmal Shankar, Junjia Li, Jessica Dowden, Alex Pankonien, Casey Whalen, Ehsan Moghbelli, and Steven Shepherd. I also thank National Aeronautics and Space Administration, Air Force Office of Scientific Research and National Science Foundation for their financial support towards this research work.

I have been extremely privileged to find friends who have also been mentors, teachers and sources of inspiration at different stages of my life. My graduate studies have been no different; I would like to thank Dr. P. J. Guruprasad for his support during my stay in College Station. I would also like to thank Shreyas, Shyam and Chandraveer for their great company. Finally, I would like to thank my parents and all my family for making this achievement possible.

NOMENCLATURE

CNTs	Carbon nanotubes
MWNTs	Multi walled carbon nanotubes
SWNTs	Single walled carbon nanotubes
ε_{33},ε’	Dielectric constant
ε_0	Permittivity of free space
ε’’	Dielectric loss
$\Delta\varepsilon$	Dielectric relaxation strength
T_s	Stress
M	Bending moment
E	Electric field
E_m	Elastic modulus
E_s	Storage modulus
w	Tip displacement
t	Thickness
Δt	Thickness change
L	Length
Z	Impedance
U_0, V	Voltage
σ	Conductivity
C	Capacitance
C_0	Capacitance of free space

D_f	Loss factor
$\tan(\delta)$	Loss tangent
G_p	Conductance
P_i	Polarization
M_{ijkl}	Coefficient of electrostriction associated with electric field
Q_{ijkl}	Coefficient of electrostriction associated with polarization
S_{ij}	Strain
s_{ijkl}	Compliance
d_{ijk}	Piezoelectric strain coefficient
T	Temperature
T_g	Glass transition temperature
FTIR	Fourier transform infrared spectroscopy
ATR	Attenuated total reflection
SEM	Scanning electron microscopy
TMA	Thermo-mechanical analysis
DMA	Dynamic mechanical analysis
α_{ij},CTE	Coefficient of thermal expansion
DSC	Differential scanning calorimetry
TSC	Thermally stimulated current
EAPs	Electroactive polymers

TABLE OF CONTENTS

Page

Page

Page

LIST OF FIGURES

FIGURE Page

FIGURE Page

FIGURE Page

FIGURE Page

FIGURE Page

FIGURE Page

FIGURE Page

LIST OF TABLES

1.INTRODUCTION

1.1 Problem statement

Carbon nanotubes (CNTs) possess excellent mechanical, electrical and electromechanical properties. Various researchers have tried to take advantage of this impressive suite of properties by incorporating the CNTs in polymers. Enhancements in mechanical properties of the resulting nanocomposites have been promising but fall well short of the exceptional properties demonstrated by CNTs. The improvements in electrical properties have been substantial and CNT-polymer nanocomposites exhibit percolation thresholds below 0.1 vol% - a fraction of what has earlier been achieved with micron-scale inclusions like carbon black. Similarly, orders of magnitude improvement in the dielectric constant has been observed in these nanocomposites.

Polymers that demonstrate an electromechanical coupling, called electroactive polymers (EAPs), suffer disadvantages like high actuation electric field, low blocked stress and low work density. Improved mechanical, electrical and dielectric properties in CNT-polymer nanocomposites coupled with the critical parameters such as high interfacial area, large number of CNTs per unit volume, high aspect ratio of CNTs and CNT-polymer interaction are compelling reasons to investigate these multifunctional nanocomposites for their electromechanical or active properties. To date, the research targeted at addressing improved electromechanical properties of polymers using CNTs has concentrated on improving the electroactive properties of piezoelectric polymers. Levi et al[1] and Kang et al[2] have demonstrated marginal improvements in piezoelectric strain coefficients of poly(vinylidene fluoride trifluoroethylene) P(VDF-TrFE) and (β-CN) APB ODPA polymide respectively. Levi et al[1] observed an increase in the d_{31} value from 20 pC/N for the pure P(VDF-TrFE) film to 25 pC/N for 0.1wt% SWNT content composite. Kang et al[2] have demonstrated an increase in d_{31} normalized by poling voltage from a value of 1 for pure polyimide to 1.2 for polyimide with 0.02 wt% SWNT content.

This dissertation follows the style of *Macromolecules*

Other studies have demonstrated increase in the polar crystalline microstructure responsible for the piezoelectric properties of PVDF[3-5]. Zhang et al[6] have demonstrated enhanced electrostrictive response in poly(vinylidene fluoridetrifluoroethylene-chlorofluoroethylene) P(VDF-TrFE-CFE) due to multiwalled carbon nanotubes (MWNTs), but they only focused on a couple of CNT concentrations and no improvement was seen in the high magnitude of actuation electric fields. Furthermore, till date, the critical drawback of high actuation electric field required for the strain response of electronic polymers has not been addressed. Specifically, the questions that need to be addressed are:

A) Can presence of CNTs in electroactive polymers address current challenges such as increasing strain and lowering electric field?

B) What is impact of CNT content and polarity of polymer on resulting electromechanical performance?

C) What is the role of the CNT-polymer interaction on the electromechanical response of polymers?

These questions are considered and addressed in this dissertation. The effect of SWNT content, polymer matrix dipoles and SWNT-polymer interaction on the electromechanical response of SWNT-polymer nanocomposites is investigated and strategies are developed to enhance and optimize this response.

In the first step we investigate the electromechanical actuation response resulting from adding single walled carbon nanotubes (SWNTs) to a non-polar polyimide (CP2). The polyimide CP2 does not show any electromechanical response in the absence of SWNTs but the SWNT-CP2 nanocomposites demonstrate a polarization-driven electromechanical response. Contributions to the electromechanical response from the polyimide matrix, SWNTs and SWNT-polyimide interaction are investigated.

In the second step we investigate the actuation response in a SWNT - polar polyimide (β-CN) APB-ODPA nanocomposite. The polyimide used is similar in

structure and properties to the non-polar polyimide except for the dipole moment on the polyimide chain that leads to a non-covalent interaction between the SWNTs and the polyimide matrix. This step allows us to understand the effect of polymer matrix dipole and the SWNT-polymer interaction on the polarization of the nanocomposites and ultimately the actuation response.

Finally, the quadratic electromechanical response is investigated in a SWNT – polyvinylidene fluoride (PVDF) nanocomposite. PVDF is one of the most polar polymers available and also demonstrates an interaction with the SWNTs. In this stage we try to take advantage of the findings of the first two steps and optimize the electromechanical actuation response in SWNT – polymer nanocomposites. Differences in mechanisms driving the actuation response in the amorphous systems (polyimides) and the semi-crystalline polymer (PVDF) system are also evaluated. Efforts are made to enhance the electromechanical response of SWNT-PVDF nanocomposites.

1.2 Background

1.2.1 Carbon nanotubes (CNTs)

There exists a broad and comprehensive literature on the exceptional physical properties of carbon nanotubes (CNTs). These carbon allotropes have sustained enthusiasm of researchers for almost two decades due to their potential for use in a wide range of applications from aerospace structures, medicine to microelectronics. As a result there have been both theoretical and experimental studies on CNTs to understand and quantify their properties. Carbon nanotubes are classified into single walled carbon nanotubes (SWNTs) and multi walled carbon nanotubes (MWNTs). SWNTs are often described as a single layer of graphene rolled into a seamless tube and capped by hemispheres at both ends. MWNTs can be visualized as made up of multiple layers of rolled-up graphene sheets (multiple walls). Figures 1.1(a& b) show schematics of both.

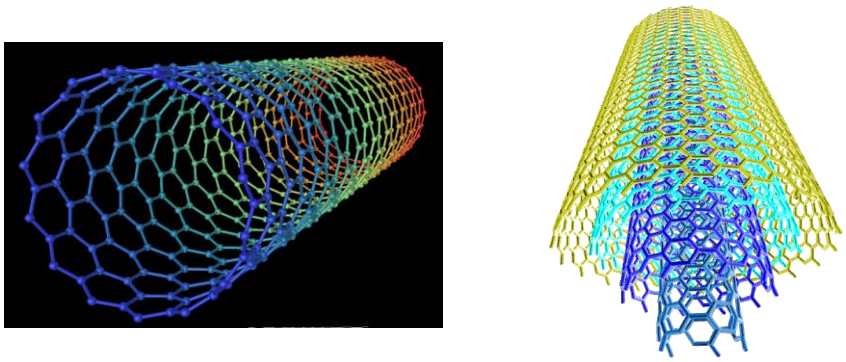

(a) (b)

Figure 1.1 (a) Single walled carbon nanotube (SWNT)[7], (b) Multi walled carbon nanotube (MWNT)[8].

The diameters of SWNTs are in the range of 1-5 nm while the lengths range from 1 μm to as high as 4cm [9, 10]. MWNTs in comparison have of around 13-50 nm and lengths on the order of 10-500 μm[9].

SWNTs have created a lot of enthusiasm because of an impressive repertoire of properties which are absent in most engineering materials. Experimental and theoretical studies of Young's modulus of SWNTs have reported values of 1-1.8 TPa, tensile strength between 3 - 30 GPa and shear modulus of about 450 GPa[11-15]. MWNTs have also shown Young's modulus of around 1.28 TPa [16]. These values reported for CNTs are comparable to those of diamond at one-third its density.

CNTs can demonstrate ballistic quantum conduction [17, 18]. Ropes made of metallic SWNTs can show a resistivity of 10^{-4} Ω-cm[19] and current density of up to 10^7 A/cm^2 which is higher than that of typical superconductors[17]. Excellent thermal conductivity of CNTs has also been reported[20].

CNTs also exhibits electromechanical properties. Kim et al[21] have demonstrated MWNT nanotweezers (Figure 1.2) that close and open on application of electric field due to electrostatic forces.

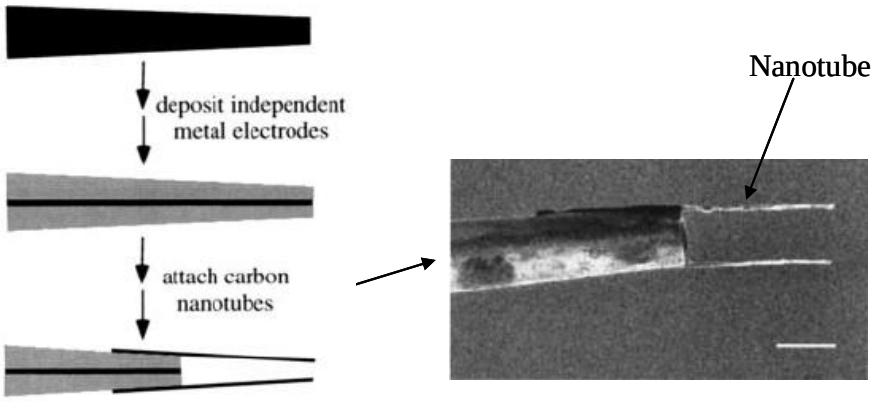

Figure 1.2 Nanotweezers using nanotubes (adapted from[21]) {scale bar is 200nm}.

Baughman et al[22, 23] have shown dimensional changes in SWNTs and bucky paper. On application of a square wave potential, an electron or electron hole is injected into the SWNT using an atomic force microscopy (AFM) tip (Figure 1.3) causing a change in the length of the tube attributed to weakening of carbon-carbon bonds. This occurs due to injection of an electron, populating states with anti-bonding character. Adding an electron hole (removal of electron) depopulates the bonding states.

In the bucky paper actuation experiment, the paper was immersed into an electrolyte as an electrode. Applied voltage injects charge into this paper, which is compensated by ions in the electrolyte resulting in a charged double layer (Figure 1.4). Electron or electron hole injection due to the formation of the double layer into the nanotubes causes dimensional changes leading to bending displacement of the bimorph in a cantilever arrangement (Figure 1.5)[23]. The bucky paper actuators are promising due to the superior mechanical and electrical properties of nanotubes along with their ability to actuate. Around 0.2% strains are achieved for an applied voltage of 0.2-0.5V with maximum predicted strains of 1% at 1V. However these materials need an electrolyte to function as actuators.

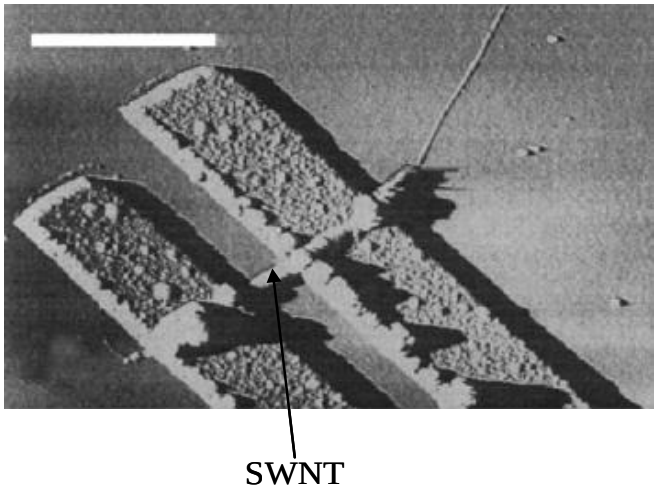

Figure 1.3 AFM image of the SWNT actuation experiment setup (adapted from[22]) {scale bar is 1μm}.

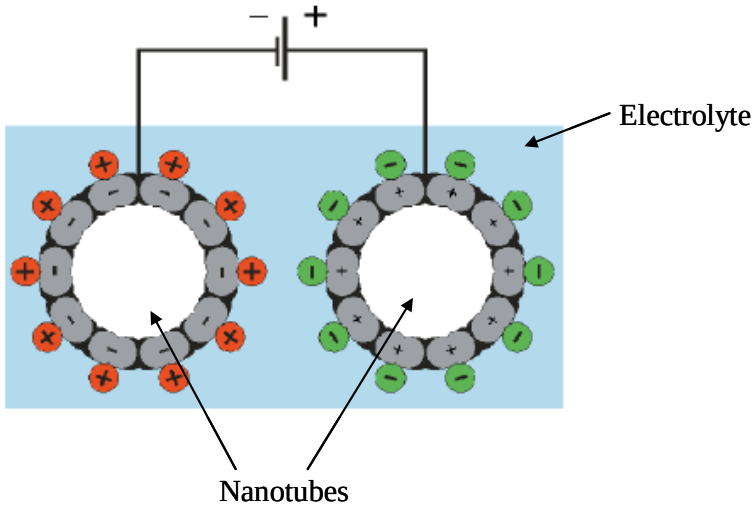

Figure 1.4 Formation of a double layer in a nanotube immersed in electrolyte. Applying a voltage to two nanotube electrodes injects charges of opposite signs which are then balanced by the ions in the surrounding electrolyte denoted by the positive and negative spheres (adapted from[23]).

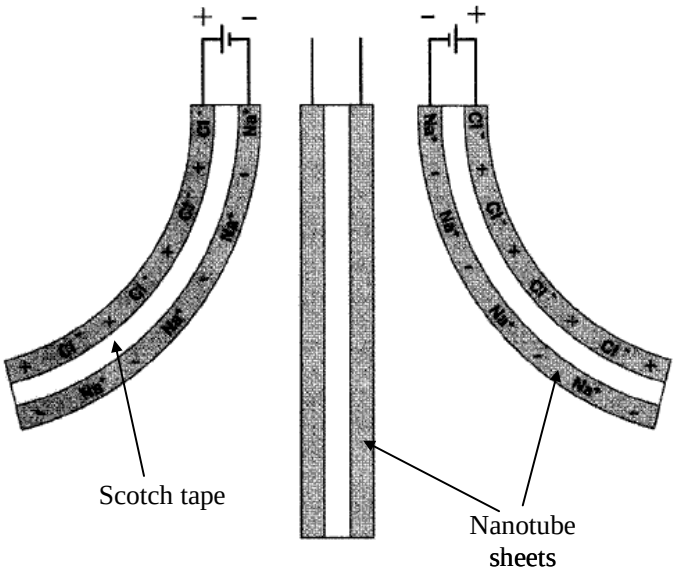

Figure 1.5 Bending of the bucky paper under an applied field. Na+ and Cl- are the ions in the electrolyte while the + and – signs denote the charges injected into the nanotube sheets(adapted from[23]).

SWNTs can also show an electrostrictive response. El-Hami et al[24] have demonstrated this quadratic response experimentally by using an AFM tip to apply the electric field and detect the dimension change as shown in Figure 1.6. This study concluded that SWNTs possess a radial electrostrictive response with an electrostrictive coefficient of 2 x 10^{-6} m^2/MV^2. Guo et al[25] have also shown the axial electrostrictive response of SWNTs using density functional quantum mechanics calculations.

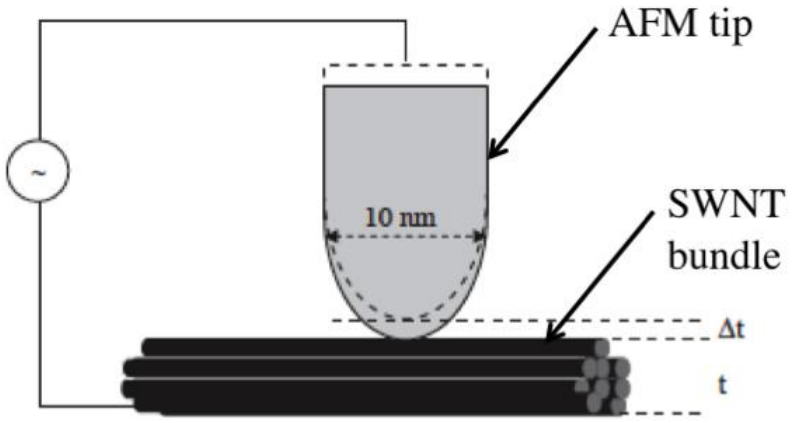

Figure 1.6 Electrostrictive response of SWNTs (adapted from [24]).

1.2.2 Multifunctional carbon nanotube (CNT)-polymer nanocomposites

Research on carbon nanotube – polymer composites has developed and gained importance due to the promise of enhanced mechanical, electrical and thermal properties by incorporating CNTs. Along with the exceptional properties of CNTs, their high interfacial area can also contribute toward enhanced properties. The interfacial region in the nanocomposites plays the important role of connecting the nanotubes and the polymer matrix. Since the nanotubes have a high aspect ratio (length/diameter ~ 1000), they possess a large surface area to volume ratio that translates into a larger interfacial region in nanotube-based nanocomposites compared to other conventional micron-scale fillers like carbon fibers.

The biggest hurdle researchers have faced to date is achieving good dispersion of CNTs in polymer. CNTs have a tendency to form agglomerates due to van der Waals attraction leading to a difficulty in separating the CNTs and dispersing them uniformly in the polymer matrix. Different processing methods have been used to address this issue. Though they may be fundamentally different in philosophy, all of the processing methods try to address issues like de-agglomeration of nanotube bundles, dispersion of CNTs and interfacial bonding between the nanotube and the polymer matrix without

destroying the integrity and aspect ratio of the CNTs[26, 27]. Pre-processing is carried out as the first stage to achieve these objectives. This step includes eliminating the catalyst residue from the CNTs through annealing and acid treatments[28, 29], de-agglomeration by ultrasonication [30] or electrostatic plasma treatment[31, 32], and in some cases, chemically functionalizing the CNTs for an enhanced interaction with the polymer[33, 34].

The next step involves processing the nanocomposites using techniques like melt mixing, solution casting and in-situ polymerization. Melt mixing is generally carried out for nanotube-thermoplastic polymer nanocomposites. Melt mixing includes processing techniques such as extrusion, injection and blow molding, and internal mixing[31]. As the concentration of nanotubes increases, more energy is required for the melt mixing to efficiently disperse nanotubes due to the increase in melt viscosity with nanotube content. Polymer composites with up to 25vol% MWNTs have been reported using high energy melt mixing techniques[35]. These processes are fast, simple, and are not solution-based. In solution processing, both thermoplastics and thermosets have been used to make nanocomposites. In this method polymer is dissolved in a solution, nanotubes are dispersed in the solution and the solution is evaporated to give a well-dispersed nanocomposite. Such nanocomposites based on epoxy[36] and polystyrene[37] polymer matrices, amongst others, have been reported using this technique. Another widely used method is i*n-situ* polymerization which is a specific technique developed using solution processing. In i*n-situ* polymerization, the polymerization of the organic constituents takes place in the presence of nanotubes. The general practice involves sonicating the nanotubes in a solution before adding to the constituents[30]. This process fares well compared to the others in terms of achieving good dispersion and better interaction between the polymer and the nanotubes.

The role of the interface in nanocomposites is critical to achieving an efficient dispersion and enhancement in properties. Vaia and Wagner[38] state six characteristics distinguishing polymer nanocomposites from traditional composites resulting from the nano-scale dimensions and high aspect ratio of the inclusions;

- Low percolation threshold (~0.1-2 vol%)
- Inclusion-inclusion interaction at low vol%
- Large density of inclusions per inclusion volume (10^6-10^8 inclusions/μm^3)
- Large interfacial area per volume of particles (10^3-10^4 m^2/ml)
- Short distances between inclusions (10-50 nm at 1-8 vol%)
- Comparable length scales between the inclusions, distance between the inclusions and relaxation volume of particle chains.

The interfacial region is usually ascribed properties different from the inclusion and the polymer matrix. This region is thought to extend into the matrix through approximately $4R_g$ distance where R_g is the radius of gyration[38]. Many important static and dynamic properties in polymers are dependent on this characteristic length. Due to large number of inclusions in nanocomposites the size of interfacial region is comparable to that of the distance between the inclusions. Good dispersion and strong interaction between the inclusions and matrix are ostensibly connected. True dispersion results in more inclusion interfacial area available and better properties; researchers have therefore concentrated their efforts on strengthening the polymer-nanotube interaction to more fully exploit the properties of CNTs.

CNT-polymer nanocomposites have the potential to be multifunctional where impact on properties goes beyond mechanical properties enhancement. For the scope of this work we will discuss briefly the literature on three main classes of CNT-polymer nanocomposite properties:

a) Mechanical
b) Electrical and dielectric, and
c) Electromechanical

1.2.2.1 Mechanical properties of polymer nanocomposites

Shaffer and Windel[39] were amongst the first to carry out an investigation into the mechanical properties of CNT-polymer composites. They did so on pristine MWNT-poly vinyl alcohol (PVA) composites made by solution processing. The axial modulus of the nanotubes used to model the experimental in plane stiffness data assuming short fiber

composites was around 150 MPa. This value was well below values predicted for MWNTs. These low values were attributed to potential defects in the nanotubes and issues with the interfacial bonding. Qian et al. [37] had better results with MWNTs and polystyrene with around 40% increase in the elastic modulus at 1wt% MWNT loading. They achieved this enhancement by using better quality nanotubes and using sonication to pre-disperse the nanotubes in a solution separately before using the solution processing method, hence most likely resulting in a good dispersion.

Gorga et al[40]. reported an increase in stiffness of poly methyl methracrylate (PMMA) from 2.7 to 3.7 GPa at 10 wt% MWNT content, 170% increase in toughness, and increase in strength from 64 to 80 MPa Meincke et al[41] have shown a 60% increase in modulus of Nylon-6 at 12.5 wt% MWNT but the gains were accompanied by a decrease in ductility. Liu et al[42] have demonstrated more than 300% increase in modulus at only 2wt% MWNT loading in Nylon-6 along with about 160% increase in yield and ultimate tensile strength as shown in Figure 1.7. This result one of the most promising ones to date and the improvements were possible due to an excellent dispersion of MWNTs and its adhesion with Nylon-6.

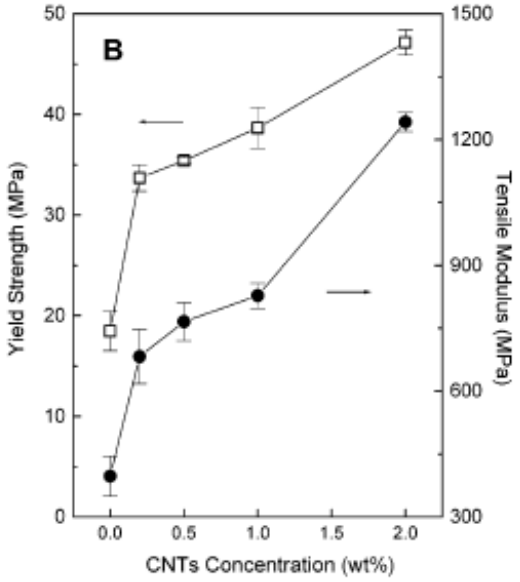

Figure 1.7 Increase in yield strength and tensile modulus of Nylon-6 with MWNT wt% [42].

Manchado et al[43] have reported an increase in modulus of polypropylene of about 40% at 0.75 wt% SWNT loading. A 60% increase in the modulus has also been reported by Park et al[30] in an in-situ polymerized polyimide CP2 in the presence of SWNTs. Other literature on this subject also reveals that including pristine nanotubes in polymer for enhancing mechanical properties is advantageous but the gains observed do not justify the use of high cost materials like CNTs. Given the reported mechanical properties of CNTs, mechanical gains reported in nanocomposites thus far fall short of expectations and most studies point to dispersion of CNTs and interfacial interaction as the dominant causes. For that reason, parallel efforts have focused on fucntionalization of CNTs to tune and control their interaction with the polymer matrix.

The walls of the carbon nanotubes are usually unreactive to most polymer matrices. Anchoring or bonding the nanotubes in the polymer matrix would help in achieving a better dispersion due to the improved interaction between the nanotubes and the polymer matrix leading to better mechanical properties. This can be done in two ways: using covalent or non-covalent functionalization. Figure 1.8 shows the different covalent and non-covalent functionalizations used in carbon nanotubes

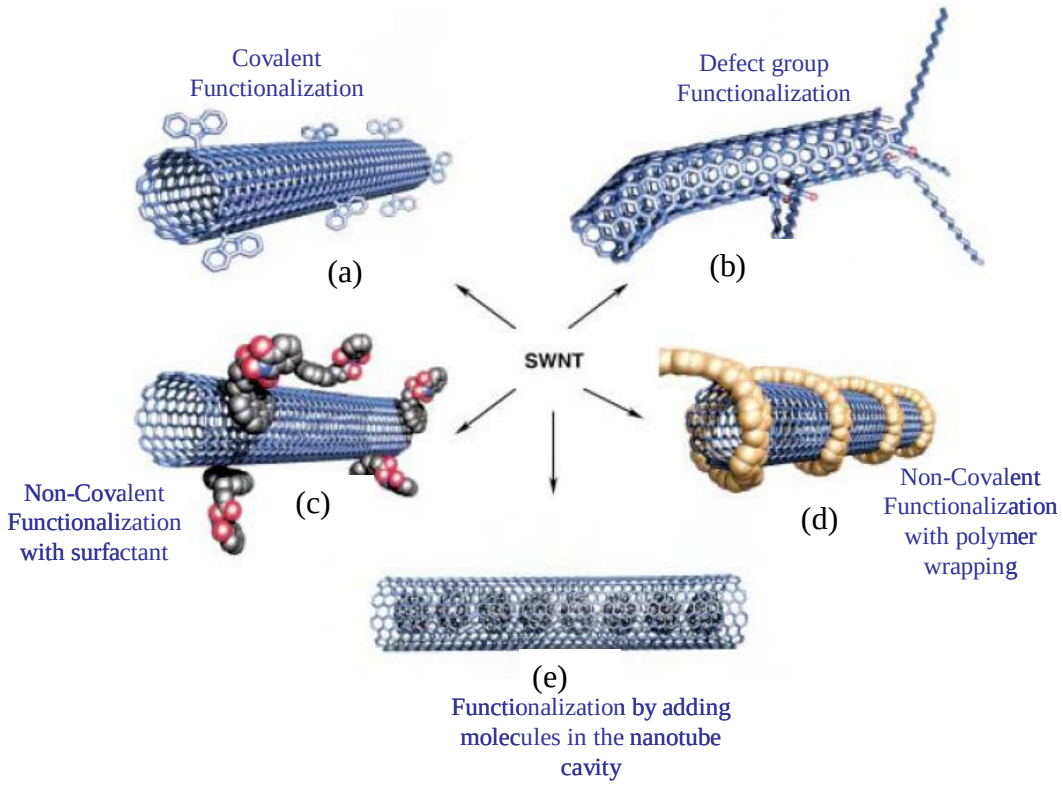

Figure 1.8 Different types of covalent and non-covalent functionalization schemes of CNTs (adapted from [34]).

Covalent functionalization involves chemically modifying the nanotubes to add a functional group to the nanotube wall to increase affinity to the polymer matrix. Covalent functionalization promises an effective interaction with the polymer matrix due to the freedom of attaching suitable groups to the nanotubes that can mechanically lock with the matrix chains or react with them. Non-covalent functionalization involves promoting interaction through physical means by avoiding chemical modification of the nanotubes and therefore, it does not involve added functional group to the nanotube.

Ramanathan et al[44] have shown an increase of 86% in the storage modulus for 1 wt% amino functionalized SWNT-poly(methyl methacrylate) (PMMA) nanocomposites compared to 48% increase in the unfunctionalized SWNT nanocomposites case. Miyagawa et al[45] have studied the properties of fluorinated SWNT-epoxy nanocomposites. An increase of 33% was seen in the storage modulus at 0.3wt% SWNT

content at room temperature due to disruption of van der Waals attraction between SWNTs by the fluorine atoms. Hwang et al[46] showed an increase in modulus of PMMA from 2.9 to 29 GPa by addition of 20 wt% PMMA-grafted MWNTs; this study is significant due to the high modulus achieved and the high SWNT content used. Covalent functionalization of CNTs does not always improve the mechanical properties of CNT-polymer composites. Using molecular dynamics simulations, Garg and Sinott[47] have shown that the mechanical strength of the nanotubes can actually decrease by around 15% due to introduction of sp3 hybridized carbon defects added by chemical functionalization. Miyagawa et al[45] have seen an increase in storage modulus at room temperature but they also report a decrease in the modulus value as a function of the fluorinated SWNT content above its T_g as shown in Figure 1.9 .

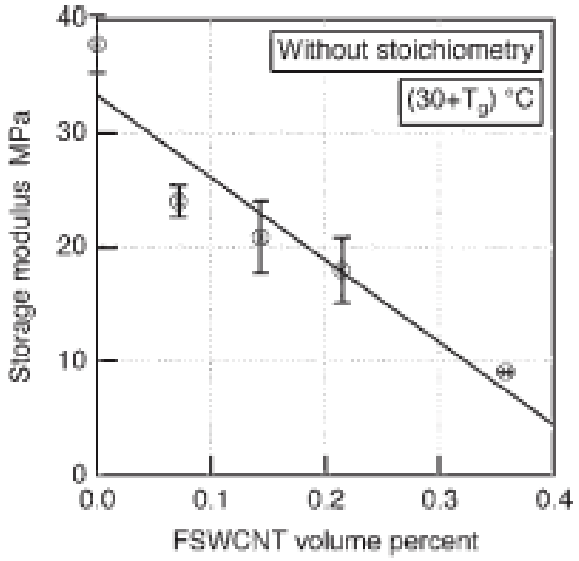

Figure 1.9 Decrease in storage modulus of Epoxy nanocomposite as a function of fluorinated SWNT content above Tg of Epoxy[45].

Other studies with functionalized nanotube polymer composites do not show appreciable enhancement in properties. Santos et al[48] have studied the properties of COOH functionalized MWNTs dispersed in PMMA by *in-situ* polymerization. An increase in tensile strength was seen for 1.5 wt% functionalized MWNT-PMMA

samples compared to 1 wt% pristine and 1 wt% functionalized nanotube-PMMA composites but no appreciable improvements were observed in the tensile strength of the composites. Thus studies on functionalized nanotube-polymer composites do not provide unequivocal evidence of the usefulness of using functionalized nanotubes in CNT-polymer nanocomposites. Furthermore, the biggest drawback in functionalizing CNTs is the dramatic changes in their electrical properties [49]. Functionalization alters the Fermi level and thus the electron energy levels of the nanotubes. This occurs due to introduction of an impurity state near the Fermi level. The addition of a covalent bond on the nanotube leads to the formation of σ bonds at the expense of the π bond. This affects the conduction band and hence the electrical conductivity of the nanotubes. Thus multifunctional applications that rely on the electrical conductivity of the nanotubes will suffer.

A unique study was carried out by Chen et al[50] to aid dispersion and mechanical property improvement of polymer-SWNT nanocomposites. They used non-covalent functionalization for efficient dispersion of the SWNTs. Rigid and conjugate macromolecules, poly(p-phenylene ethynylene)s (PPEs), were used to non-covalently functionalize and solubilize the SWNTs and attain good dispersion in the polymer (Parmax) matrices. The non-covalent interaction was attributed to a π- π interaction between the carbon nanotube walls and the backbone of PPE. This research demonstrated an enhancement of 72% in the tensile strength and twelve orders of magnitude increase in the electrical conductivity in the composites. The study was successful in tailoring the interface between the nanotube and polymer matrix by non-covalent means; improvement in mechanical properties was achieved without sacrificing the excellent electrical properties of nanotubes due to their unique electronic structure.

The review of the effects of CNTs on the mechanical properties of polymers suggests that though some studies have shown some improvements, the level of improvement shown thus far does not approach the promise that the high mechanical properties of CNTs suggest. The reasons for this discrepancy range from challenge in dispersion to types of CNTs used and compatibility between polymers and CNTs.

1.2.2.2 Electrical and dielectric properties of CNT-polymer nanocomposites

Bundles of metallic SWNTs can theoretically reach a conductivity of 10^4 S/cm [19]. Almost all commercial sources of SWNTs are a mixture of both metallic and semi-conducting. Adding the SWNTs to polymers offers an avenue to improve the conductivity of polymers and tailor the conductivity levels by controlling the CNT content. Due to the high aspect ratio of CNTs, the concentration required to achieve conductive behavior in the CNT-polymer composites is usually very low. The percolation threshold signifies the transition between insulating and conductive behavior. Figure 1.10 shows a schematic of the dependence of electrical conductivity as a function of frequency below and above the percolation threshold. Below the percolation threshold the conductivity increases with frequency while it is constant with frequency above the threshold. This transition is also accompanied by a jump in the conductivity magnitude as shown by Figure 1.11.

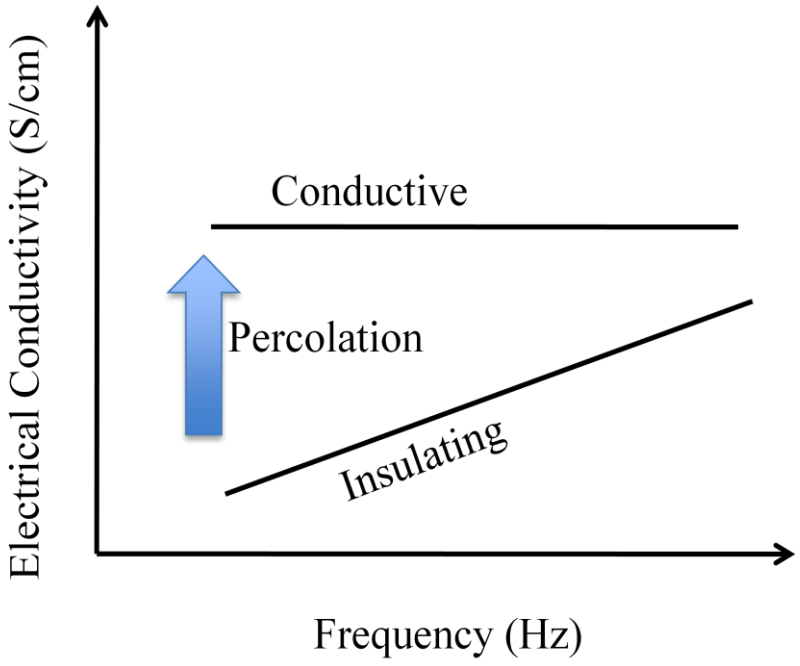

Figure 1.10 Electrical conductivity as a function of test frequency.

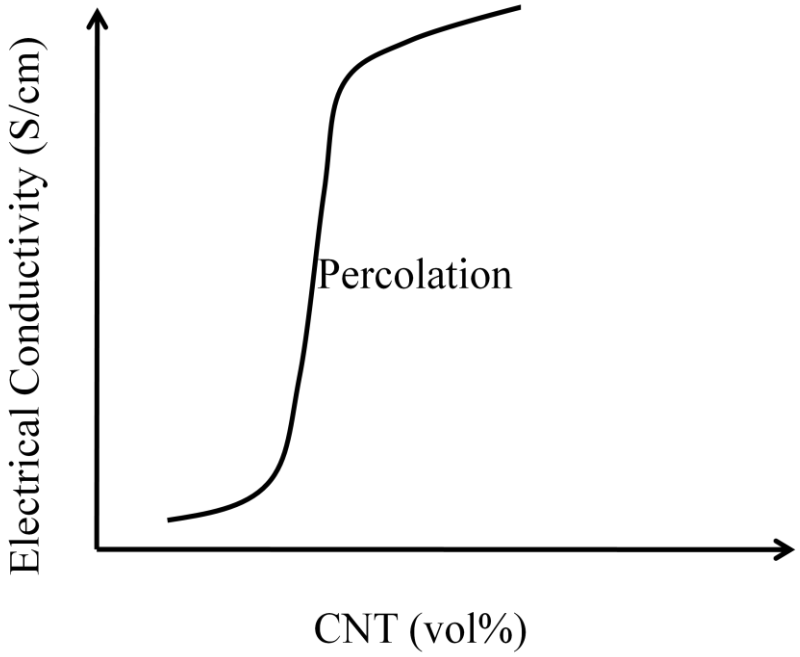

Figure 1.11 Electrical conductivity as a function of CNT loading.

A percolation threshold of as low as 0.05-0.06 vol% SWNTs has been reported in polyimide nanocomposites[30, 51, 52]. There have also been other studies that have reported percolation threshold below 0.1 wt% in a host of CNT-loaded matrices like epoxy, polycarbonate (PC), polyethylene (PE) and polymethyl methacrylate (PMMA) [53-57]. Due to their low percolation thresholds, these nanocomposites have been suggested for electrostatic discharge and electromagnetic shielding applications in aerospace structures as they combine excellent optical transparency and electrical conductivity[51]. Applications have also been suggested for use of MWNT-polyaniline composites as printable conductors for organic electronics devices [58].

Bauhofer et al[59] have compiled a comprehensive summary of the literature available on the conductivity data of CNT-polymer nanocomposites. Figure 1.12 shows a composite plot containing the conductivity values from different studies as compiled by Bauhofer et al[59]. It can be seen that conductivity values as high as 10^2 S/cm has been obtained in polymer nanocomposites. For CNT content less than 0.01 wt% conductivity

values of 10^{-5} S/cm can be obtained which are at least 7-10 magnitudes higher than those seen in pristine polymers.

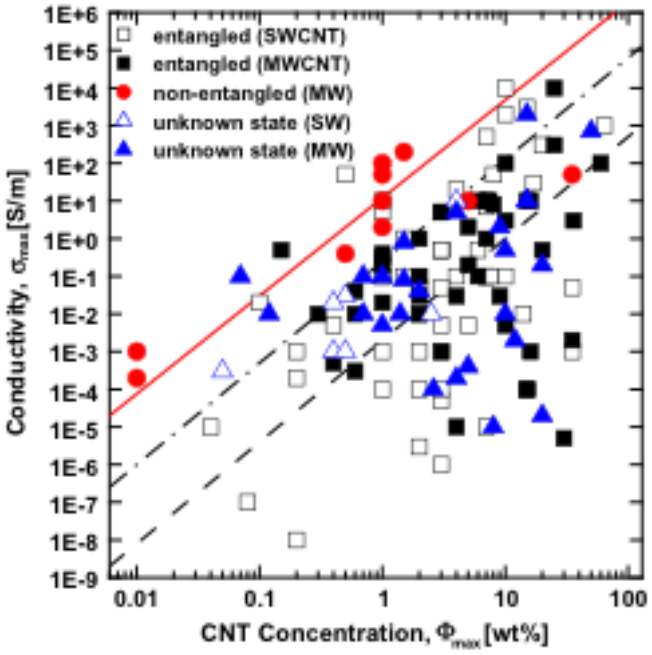

Figure 1.12 Maximum conductivity vs CNT wt% (reproduced from [59]).

The effect of CNTs on the dielectric properties of polymers has also been studied along with that on electrical conductivity by several researchers. Generally an increase in the dielectric constant has been observed with CNT content at low frequencies. Figure 1.13 shows a dielectric constant vs MWNT wt% plot from a study by Wang et al[60] on polyvinylidene fluoride (PVDF). An increase is seen in the dielectric constant with MWNT content followed by a small decrease at high vol%. Pötschke et al[61] have demonstrated an increase in the static permittivity at the percolation threshold in a polycarbonate (PC) system as seen in Figure 1.14. Figure 1.15 shows the dielectric constant of SWNT-epoxy system as a function of frequency from a study by Kim et al [62]. As can be observed, little change is seen in the values at low SWNT content. However, as the SWNT content increases a dielectric constant as high as 1000 can be observed at low frequencies. The increase in the dielectric constant is also accompanied by an

increase in the dielectric loss due, thought to result from conductive losses, as seen in Figure 1.16. The increase in the dielectric constant at the percolation threshold is attributed to interfacial polarization resulting from the differences in the conductivity of the polymer and CNTs, and also due to formation of micro-capacitors in the nanocomposites [61].

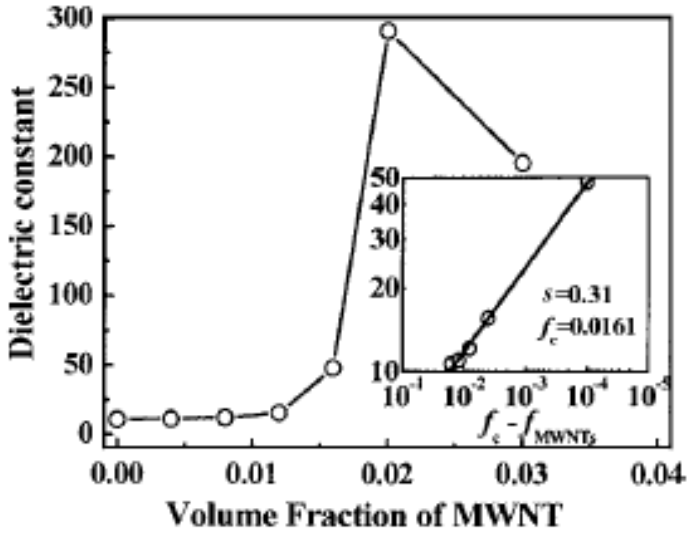

Figure 1.13 Dielectric constant of PVDF system vs MWNT wt%(reproduced from[60]).

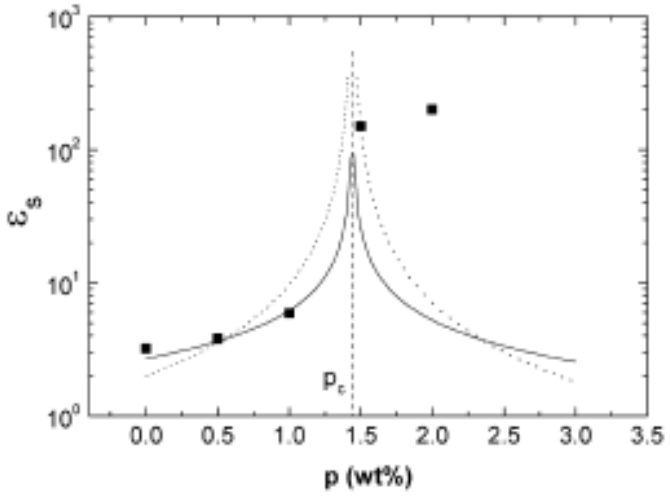

Figure 1.14 Static dielectric constant of polycarbonate system vs MWNT wt%(reproduced from[61]).

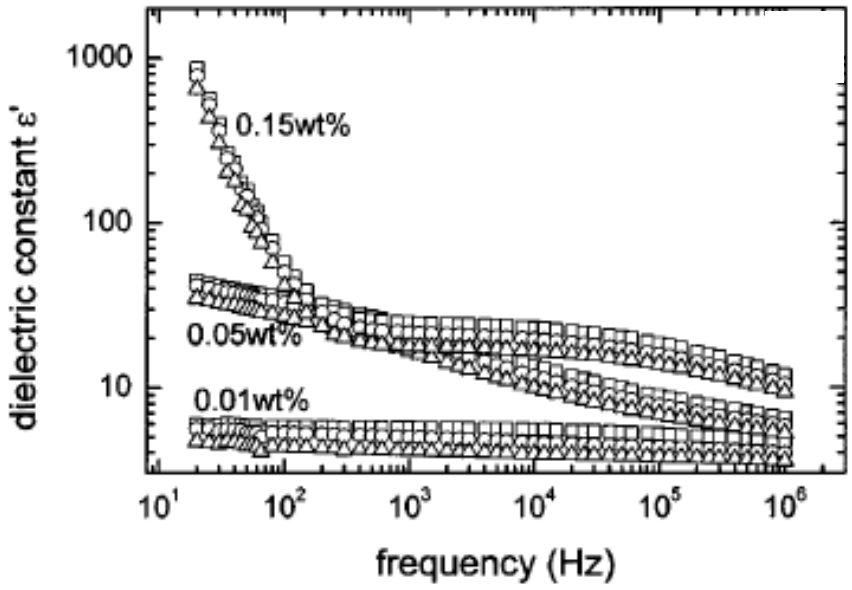

Figure 1.15 Dielectric constant of epoxy system vs SWNT wt%(reproduced from[62]).

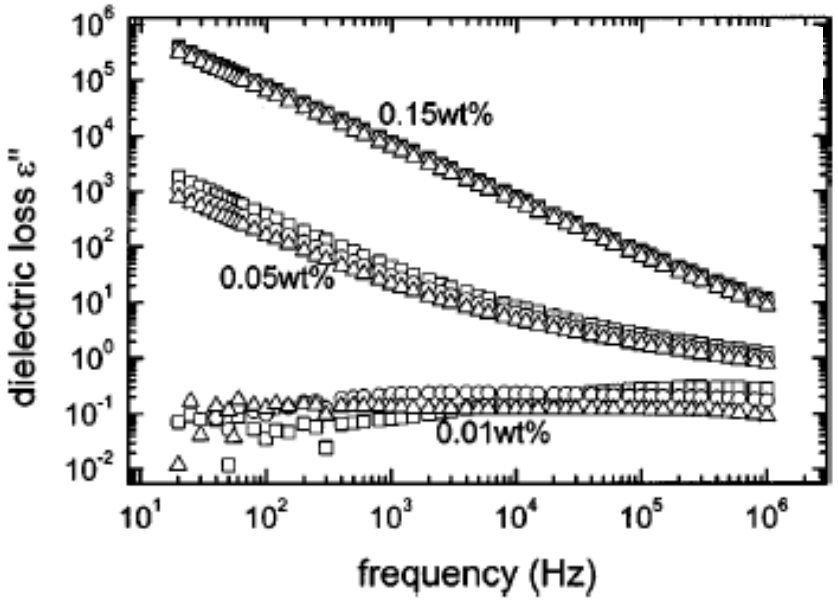

Figure 1.16 Dielectric loss of epoxy system vs SWNT wt%(reproduced from[62]).

The review of the effects of CNTs on the electrical and dielectric properties of polymers shows significant improvements in the electrical conductivity and dielectric

constant of polymers at very low CNT content. The percolation threshold achieved in polymers using CNTs is a fraction of that demonstrated by micron-scale inclusions like carbon black.

1.2.2.3 Electromechanical properties of CNT-polymer nanocomposites

Polymers that demonstrate an electromechanical response (called electroactive poymers or EAPs) have been studied exhaustively as potential actuators and sensors. However, these materials have not yet found as much widespread use as was initially envisioned. This slow impact on applications can potentially be attributed to the conflicting requirements and specifications of these materials. Electronic EAPs in particular are practical as they can function in air without the need for an electrolyte (a medium needed for ionic EAPs). However, these materials require a high actuation electric field to achieve high strains as documented in Table 1.1. Table 1.2 compares different attributes of electronic and ionic EAPs. A close look at the table reveals that electronic EAPs, like elastomers, demonstrate fast response and high strains but also show low blocking stress resulting in low work density. Ionic EAPs, in contrast, show high strains but suffer from drawbacks like low efficiency, low blocked stress, slow response and the need for an electrolyte.

Table 1.1 Comparison of some electronic electroactive polymers.

Electroactive polymer	Achieved strains (%)	Electric field (MV/m)
Polyurethane (Deerfield)[63]	11	160
Silicone (Dow Corning)[63]	32	144
PVDF based electrostrictor[64]	~4	>150
PVDF (calculated from breakdown field)	~0.7	>200

Thus there is a need to address these conflicting requirements of EAPs that hinder their widespread use. The main drawbacks in current EAPs can be summarized as follows: a) need for high driving voltages/electric fields to achieve high strains in electronic polymers, b) low blocked stress and c) low work density.The exceptional mechanical and electromechanical properties of CNTs summarized earlier coupled with the enhanced mechanical, electrical and dielectric properties of CNT-polymer nanocomposites make these materials an exciting prospect to address the current drawbacks of EAPs. Some researchers have targeted these materials for evaluating their actuation and sensing response.

Table 1.2 Comparison of different actuator specifications between electronic and ionic electroactive polymers[65].

Property	Electrostatic silicone elastomer	Ferroelectric polymers	Conducting polymers	Ionic polymer metal composites
Strain (%)	120	3.5-7	2-12	0.5-3.3
Stress (MPa)	0.3-3.2	20-45	5-34	3-15
Work Density (kJ/ m^3)	10-750	320-1000	100	5.5
Strain Rate (%/s)	34000	≥ 2000	1-12	3.3
Specific Power (W/kg)	500		150	2.56
Efficiency (%)	25-80		18	2.9

Kang et al[2] have demonstrated an enhancement in the response of a piezoelectric polyimide, (β-CN) APB-ODPA, in the presence of SWNTs. They investigated a series of poled SWNT-polyimide composites and quantified their piezoelectric response through Thermally Stimulated Current (TSC) analysis as well as by direct measurement of the in-plane piezoelectric strain coefficient, d_{31}. In general, they observed a moderate increase in d_{31} normalized by poling voltage from a value of 1 for pure polyimide to 1.2 for polyimide with 0.02 wt% SWNT content as seen in Figure 1.17.

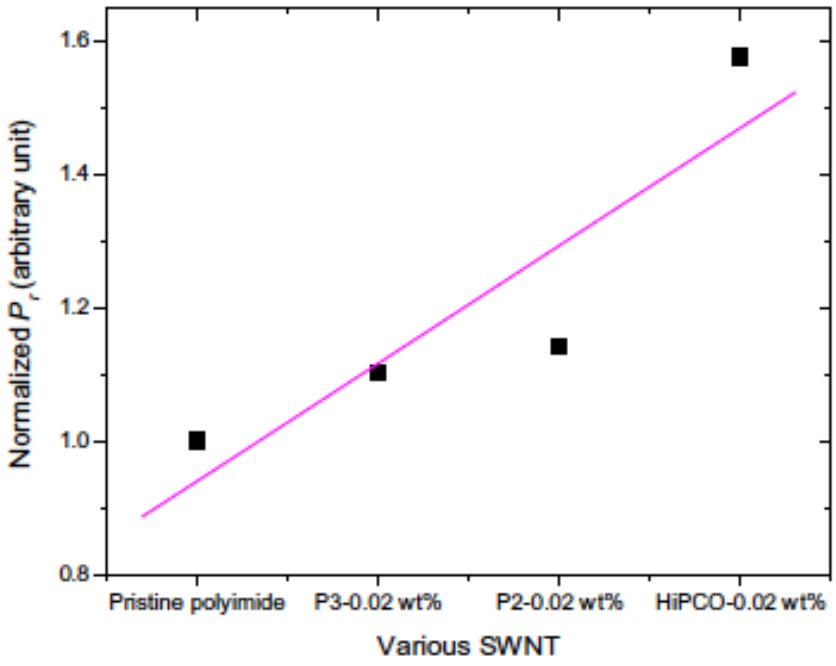

Figure 1.17 Enhanced normalized piezoelectric coefficient of a piezoelectric polyimide with SWNT wt%(reproduced from[2]).

Levi et al[1] have demonstrated an increase in the piezoelectric properties of poly(vinylidene fluoridetrifluoroethylene) (PVDF-TrFE) due to SWNTs. The researchers observed an increase in the d_{31} value from 20 pC/N for the pure polymer film to 25 pC/N for 0.1wt% SWNT content composite (Figure 1.18). This enhancement has been attributed to an increase in the piezoelectric β-phase due to addition of SWNTs.

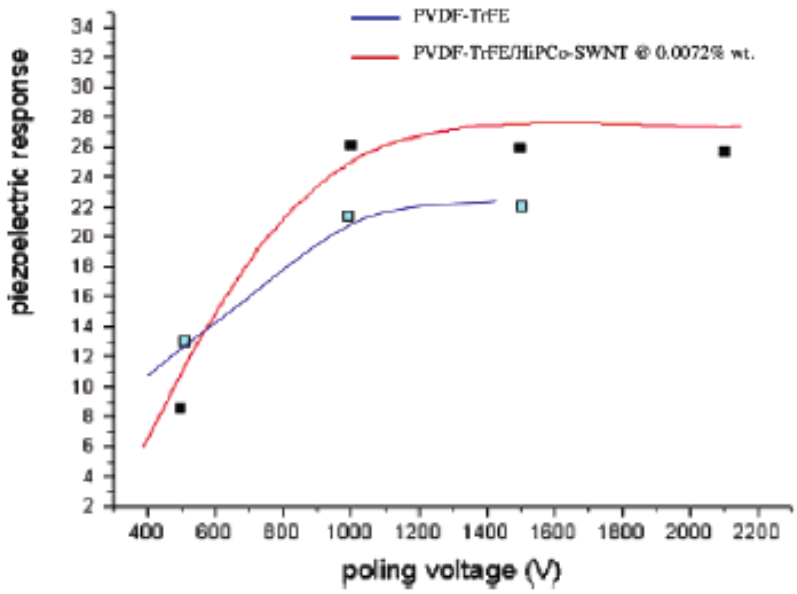

Figure 1.18 Enhanced normalized piezoelectric coefficient of P(VDF-TrFE) with SWNT wt%(reproduced from[1]).

Effect of multiwalled carbon nanotubes (MWNTs) on the actuation stress response of a polysiloxane nematic elastomers has also been studied [66]. The elastomer without MWNTs did not show any actuation stress, while an increased stress response was seen in the 0.0085wt% and 0.02wt% MWNT composites under an applied electric field. The actuation was attributed to the torque experienced by the nanotubes due to the applied field. Similarly, in a study involving ionic polymer metal composites (IPMCs), an enhancement in the actuation stress was observed for 1wt% MWNT loading above which a decrease in stress response is seen due to inhomogeneous distribution of the MWNTs [67]. In a different study, Akle et al[68] have demonstrated an increase in the strain and strain rate of a hybrid IPMC actuator by incorporating SWNTs in the electrodes, taking advantage of their conductive nature. Zhang et al[6] have demonstrated enhancement in the electrostrictive response of MWNT- poly(vinylidene fluoride-trifluoroethylene-chlorofluoroethylene) composites compared to the pure copolymer, with MWNT content of 0.5wt% and 1wt% seen in Figure 1.19. The authors reported an increase in both the mechanical and dielectric properties of these composites, which led

to the enhanced strain response at a reduced electric field. The polar β phase is the source of the piezoelectric response in PVDF. Various studies have demonstrated the formation of a polar β phase in PVDF due to MWNTs[4, 69]. Yu et al[69] have reported formation of the β phase in the presence of MWNTs. They have attributed the β phase formation to absorption of the PVDF trans-trans conformation, formed due to sonication, onto the MWNTs. Manna et al[4] have also demonstrated formation of the β phase due to interaction between the functionalized MWNTs and PVDF. Similar observations of MWNT induced β phase formation in PVDF have been reported by other researchers[3-5].

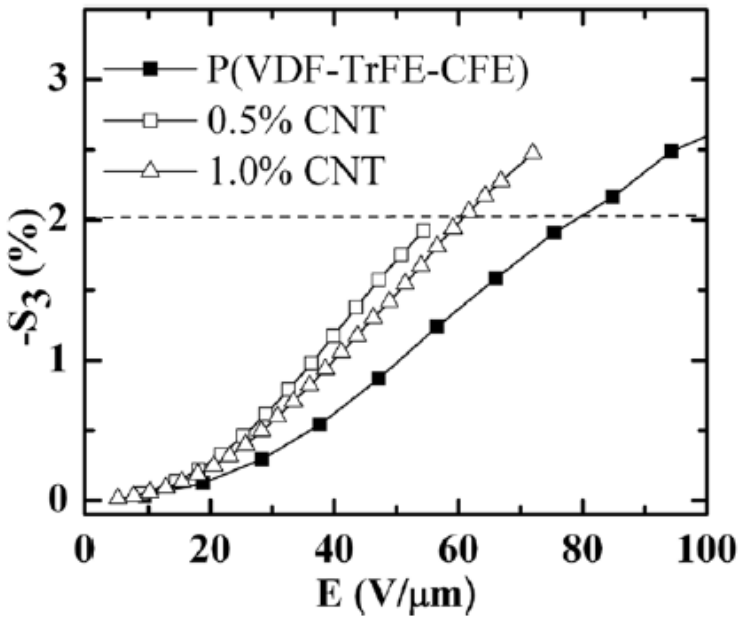

Figure 1.19 Enhanced electrostrictive response of P(VDF-TrFE-CFE) with MWNT wt%(reproduced from[6]).

Review of the open literature on the electromechanical response of CNT-polymer nanocomposites reveals a lack of an exhaustive study on impact of CNTs on effective coupled response in the nanocomposites. The increase in electromechanical properties of polymers due to addition of CNTs has been promising thus far but modest. Also the addition of CNTs has not made significant impact on the high magnitude of electric field

required for driving the actuation response in electronic EAPs. This is predominantly because most of the research has been targeted at studying the effect of CNTs on piezoelectric response of polymers driven by the piezoelectric crystalline phase and molecular dipoles. This fact restricts the use of CNTs to how they affect the polymer microstructure while any potential enhancement in the dielectric properties are not exploited. Furthermore only a few studies have investigated the interaction between the CNTs and the polymers and its effect on the electromechanical response. In this current study, as mentioned in Section 1.1, focus will be on impact of CNTs on actuation field, strain and work density without restricting ourselves to a piezoelectric phase in the polymer.

1.3 Organization of sections

This dissertation consists of 6 sections. Section 1 presents the problem statement and a literature review of the state of art of the multifunctional properties of CNT-polymer nanocomposites. Section 2 contains the experimental details of this work reviews the processing techniques used in the synthesis of the SWNT –polyimide nanocomposites, and the processing details of SWNT – polyvinylidene fluoride (PVDF) nanocomposites. This section also presents details on the characterization of physical properties including: actuation strain measurements, impedance and dielectric relaxation spectroscopy, thermal and thermo-mechanical characterization, dynamic mechanical analysis, Fourier transform infrared and Raman spectroscopy and optical/electron microscopy. Section 3 presents a comprehensive study of the SWNT- non-polar CP2 system targeting electromechanical strain measurements and a thorough investigation of the dependence of the strain and strain rate response on the SWNT content. It also documents the contributions to the driving mechanism from the polymer matrix, the SWNTs and SWNT–polymer interaction. Section 4 presents the investigation of the electromechanical properties of SWNT-polar (β-CN) APB ODPA nanocomposites and their comparison to the SWNT-non-polar CP2 nanocomposites. Based on this comparison, the dependence of the electromechanical strain response on the polyimide

dipole, and the interaction between the SWNTs and the polyimide matrix, is established. Section 5 documents the study of the electromechanical response of SWNT-PVDF nanocomposites where focus is on optimizing the electromechanical properties based on the findings of Sections 3 and 4. The differences in the contributions to the driving mechanism for the polyimide systems and the PVDF system are also evaluated. Further attempts to improve the electromechanical response of the SWNT – PVDF system are also documented. Section 6 offers conclusions and recommendations for future work.

2. EXPERIMENTAL

This section provides experimental details of the different processing methods and experimental characterization techniques used in this work. The purpose, function and theory of the experimental characterization techniques used are discussed in detail.

2.1 Processing of SWNT – polymer nanocomposites

2.1.1 SWNT-polyimide nanocomposites

The SWNTs used in this study are processed through two different routes: laser-ablated SWNTs acquired from Rice University, and high pressure carbon monoxide (HIPCo)-processed SWNTs acquired from Carbon Nanotechnologies Incorporated (CNI), Houston. In the laser-ablated process, a mixture of carbon and transition metals are evaporated by a laser impinging on a graphite-metal composite target [70, 71]. The target is kept in a controlled environment at temperatures around 1200°C and in the presence of an inert gas. The nanotube vapor condenses on the cooler part of the reactor. The yield from the laser ablated process is typically around 70%[19]. HIPCo uses carbon monoxide as the carbon source. This is a gas-phase catalytic process which involves passing carbon monoxide along with an organometallic catalyst ($Fe(CO)_5$) in a heated furnace [72]. $Fe(CO)_5$ decomposes to give iron clusters which act as nuclei around which SWNTs are deposited.

An aromatic colorless polyimide, CP2 (APB-6FDA) (Figure 2.1), and a polar polyimide, (β-CN)APB-ODPA [52] (Figure 2.2) are the polyimides used in this study. The SWNT-polyimide nanocomposites are prepared by in situ polymerization under sonication. The diamine and dianhydride used to prepare CP2 are; 1,3-bis(3-aminophenoxy) benzene (APB) and 2,2-bis (3,4-anhydrodicarboxyphenyl) hexafluoropropane (6FDA) respectively, and those used for the (β-CN)APB-ODPA are; 2,6-bis(3-aminophenoxy) benzonitrile (β-CN)APB (diamine), and 4,4-oxydiphthalic anhydride (ODPA-dianhydride). The diamine used in the two polyimides is similar except for the high dipole C-CN nitrile group. The dianhydride on CP2 contains two CF_3

groups that can show a small dipole but the rigid dianhydride structure renders the molecule non-polar.

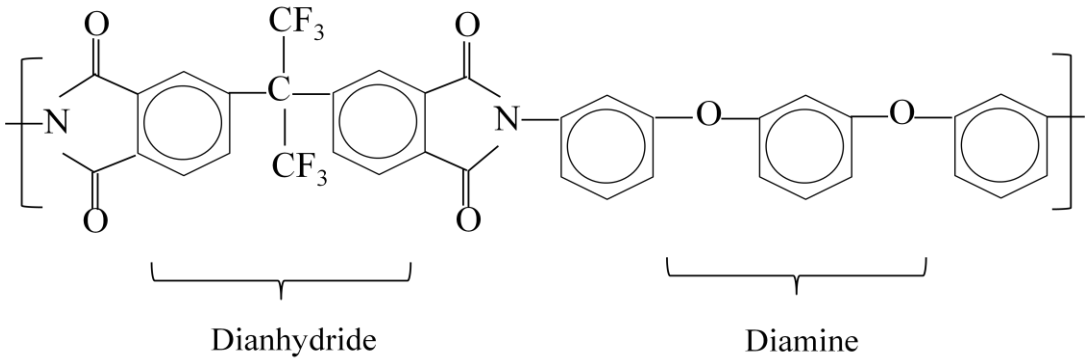

Figure 2.1 Chemical structure of CP2.

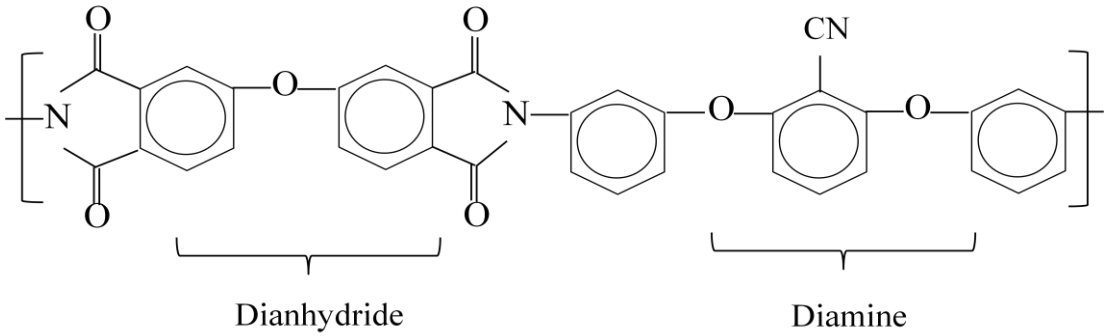

Figure 2.2 Chemical structure of (β-CN) APB-ODPA.

Both polyimides were developed by researchers at NASA Langley Research Center. CP2 was developed by St.Clair et al[73] and (β-CN) APB-ODPA by Simpson et al[74].

The SWNT-CP2 composites were prepared at NASA Langley by Park et al [30] using the following process; SWNTs are dispersed in anhydrous dimethyl formamide (DMF). After stirring, APB is added to the solution then the 6FDA. The whole process is carried out with stirring, in a nitrogen purged flask immersed in a 40kHz ultrasonic bath. This step is maintained until the solution viscosity increases and stabilizes, indicating

polymerization has taken place. Sonication is terminated after 3 hours and the stirring is continued for several hours to form a SWNT-poly(amic acid) solution. Acetic anhydride and pyridine are added to chemically imidize the SWNT-poly(amic acid) solution. The SWNT-CP2 solution is then cast onto a glass plate and dried in a dry air flowing chamber. The dried tack free film is then thermally cured in an air circulating oven at 110, 170, 210, and 250°C for 1 hour each to obtain solvent-free SWNT-CP2 film. A series of nanocomposite films are prepared with the SWNT concentrations varying from 0 to 2 vol% [30]. The SWNT-(β-CN)AP-ODPA composites were prepared by a similar method with SWNT concentration varying from 0 to 5 vol% [52].

2.1.2 SWNT-PVDF nanocomposites

PVDF used in the study is KYNAR 301 in powder form from Arkema Inc. (Figure 2.3). The unpurified HiPCO single walled carbon nanotubes were obtained from Rice University. They were further purified by a process based on [75]. The SWNT-PVDF nanocomposites are prepared by a solution casting process. SWNTs are dispersed in N,N-dimethyl acetamide (DMAc) using a probe sonicator for 3 hrs. The KYNAR 301 powder is then added to the solution and mixed by a mechanical stirrer in a 40 kHz ultrasonic bath for 24hrs. The SWNT-PVDF solution is then heated in an oven to 130°C before casting it on glass slide using a doctor blade. The cast film is kept in the oven at 130°C until all the DMAc evaporates to give a solvent-free film. The high temperature during film casting is used to ensure low viscosity. SWNT density of 1.33 g/cc is used to convert the SWNT wt% to SWNT vol%[76].

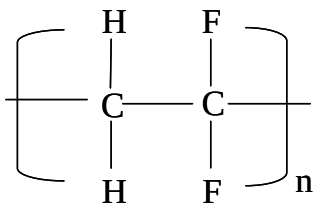

Figure 2.3 Chemical structure of PVDF.

2.2 Actuation strain measurements

Nanocomposite transverse and longitudinal actuation strains in response to DC and AC electric fields are measured using two setups: transverse and bending actuation.

2.2.1 Thickness Actuation

The nanocomposite films are coated with a thin silver layer by a vapor deposition process using a metal evaporator. The thickness of the silver layer is kept at 100 nm. For thickness actuation, a small area on the bottom face of the electroded sample is constrained and the electric field is applied through the thickness t. An MTI 2100 photonic fiber optic sensor is used to measure the change in thickness (Δt) (Figures 2.4 (a) and (b)). The transverse strains are then calculated as;

$$S_{33} = \frac{\Delta t}{t} \tag{2.1}$$

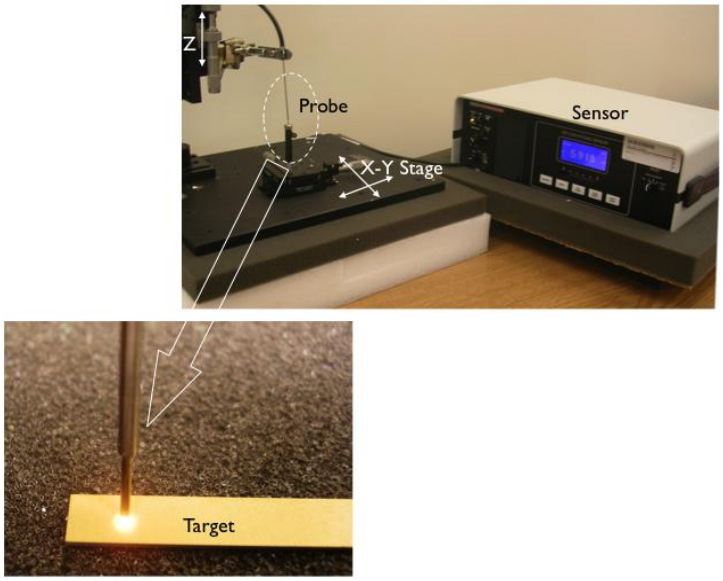

(a)

Figure 2. 4 (a) Fiber optic sensor, (b) Thickness actuation schematic.

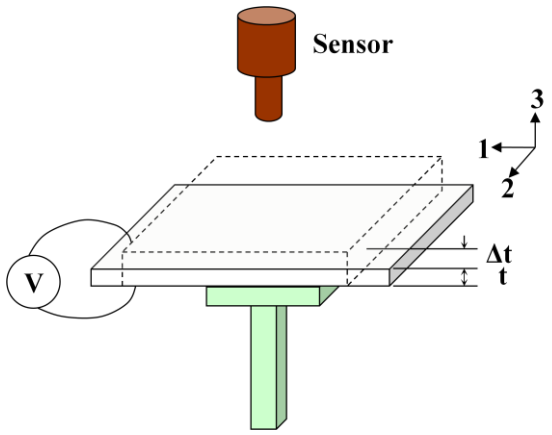

(b)

Figure 2. 4 Continued.

2.2.2 Bending actuation

The electroded film samples are cut into strips of around 3cm x 0.5cm area, which are then used for the bending actuation tests. Figure 2.5(a) shows the experimental set-up used while Figure 2.5(b) represents the bending experiment schematically. The nanocomposite strips are sandwiched between glass plates with provisions for leads. This setup is then suspended vertically in a fiber glass box chamber. The leads allow the application of electric field (DC or AC) to the strip. The bending of the sample is captured by a Fastcam high speed camera setup. An auxiliary light source is also used for better visibility. The captured videos are analyzed using Photron image analysis software**.** This software allows measurement of the sample displacement by analyzing the sample position in successive video frames.

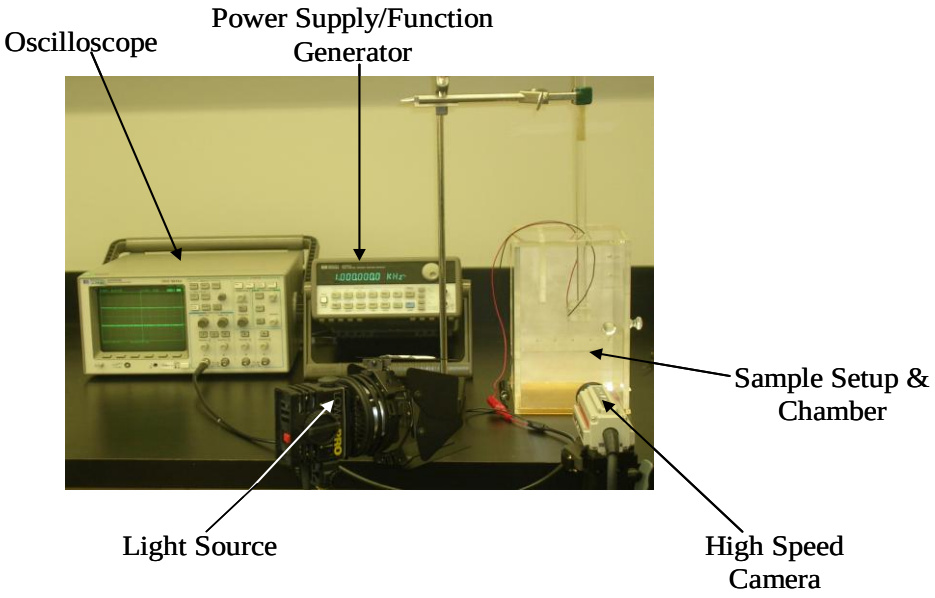

(a)

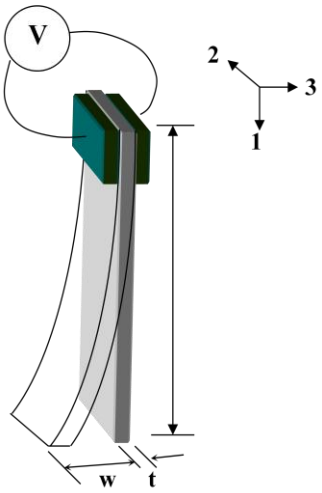

(b)

Figure 2.5 (a) Bending actuation setup, (b) Bending actuation schematic.

The elongation strain is computed by modeling the bent strip as a cantilever beam under constant bending moment, thus assuming a constant radius of curvature, using the Euler-Bernoulli beam theory. This model gives a good starting point for the calculation of strains. Assuming a bent beam with uniform bending moment (M) , tip

displacement (w), thickness (t) and length (L), the stress (T_s) acting on the outermost layer under the bending moment M is given by[77],

$$T_s = \frac{M}{I}\frac{t}{2} \tag{2.2}$$

I is the moment of inertia of the beam. Furthermore the tip displacement can also be expressed as

$$w = \frac{ML^2}{2E_m I} \tag{2.3}$$

Where E_m is the elastic modulus of the beam. Assuming Hooke's law to be valid we then find the longitudinal strain in the outermost layer is,

$$S_{11} = \frac{w \cdot t}{L^2} \tag{2.4}$$

It is noted that the strain S_{11} is measured along the length (1-direction) due to an electric field applied through the thickness (3-direction).

2.3 Impedance spectroscopy

The dielectric and electrical properties of the nanocomposite samples are measured using two different equipments. The first is a Novocontrol broadband impedance analyzer shown in Figure 2.6(a). The principle of dielectric measurement is shown in Figure 2.6(b). The sample is mounted in a sample cell between two electrodes. A sinusoidal voltage (U_0) applied to a material causes a current (I_0) with a phase shift described by phase angle (ϕ). In complex notation the relationships are given by;

$$U(t) = U_0 \cos(\omega t) = \mathrm{Re}(U^* \exp(i\omega t)) \tag{2.5}$$

$$I(t) = I_0 \cos(\omega t + \phi) = \mathrm{Re}(I^* \exp(i\omega t)) \tag{2.6}$$

$$I^* = I' + iI'' \tag{2.7}$$

$$U^* = U_0 \tag{2.8}$$

$$I_0 = \sqrt{I'^2 + I''^2} \tag{2.9}$$

$$\tan(\phi) = \frac{I''}{I'} \tag{2.10}$$

For a sample capacitor with a linear electromagnetic response, the impedance is given by:

$$Z^* = Z' + iZ'' = \frac{U^*}{I^*} \tag{2.11}$$

The complex permittivity can then be expressed as:

$$\varepsilon^*(\omega) = \varepsilon' - i\varepsilon'' = \frac{-i}{\omega Z^*(\omega) C_0} \tag{2.12}$$

where C_0 is the empty sample capacitor. ε' and ε'' are the dielectric constant and loss. The complex conductivity of the sample can then be expressed as:

$$\sigma^* = \sigma' - i\sigma'' = -2\pi f \varepsilon_0 (\varepsilon^* - 1) \tag{2.13}$$

where σ' and σ'' are the conductivity and loss respectively. f is the frequency and $\varepsilon_0 = 8.85 \times 10^{-12}$ F/m is the permittivity of free space. The frequency range used is between 0.01 Hz – 10^7 Hz.

(a)

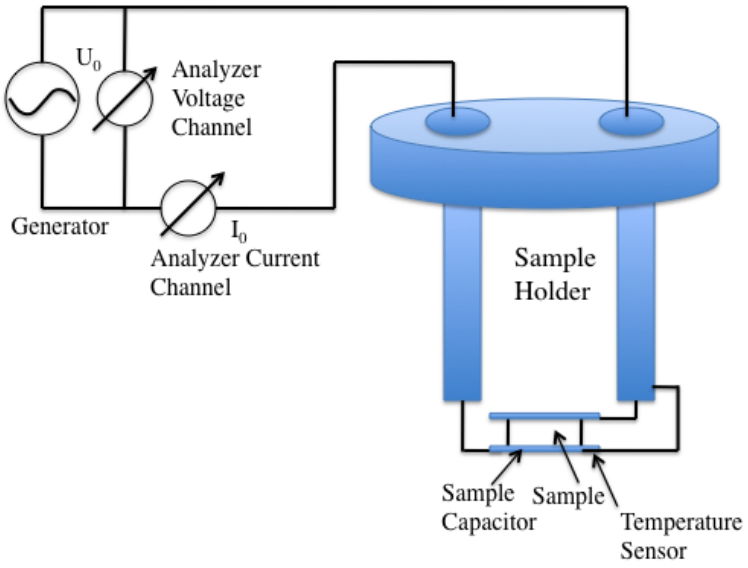

(b)

Figure 2.6 (a) Novocontrol broadband impedance analyzer, (b) Novocontrol sample cell.

The second equipment used in the study is an LCR meter (Figure 2.7). AC dielectric measurements are carried out for the nanocomposites over a range of frequencies (20Hz – 1MHz) using the QuadTech precision LCR meter. In the LCR meter the dielectric constant (ε') of the material is derived from the measured capacitance (C) in a parallel plate configuration using the thickness (t) of the sample and the electroded area (A):

$$\varepsilon' = \frac{C \cdot t}{\varepsilon_0 \cdot A} \tag{2.14}$$

The dielectric loss is then derived as:

$$\varepsilon'' = D_f \cdot \varepsilon' \tag{2.15}$$

D_f is the dissipation factor. This value is also known as the loss tangent (tanδ). The real part of conductivity (σ') is described by;

$$\sigma' = \frac{G_p \cdot t}{A} \tag{2.16}$$

where Gp is the conductance measured by the LCR meter.

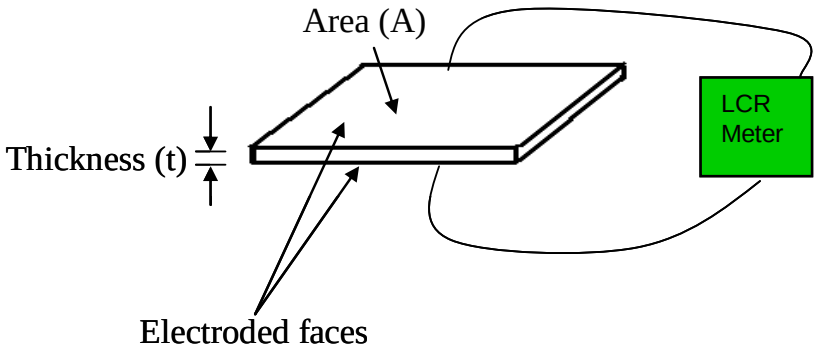

Figure 2.7 LCR meter operation principle.

2.4 Dielectric relaxation spectroscopy and polarization studies

2.4.1 Dielectric relaxation spectroscopy

Dielectric relaxation measurements are carried out to investigate the polarization inherent to the structure of the polymer and/or the enhanced polarization due to presence of nanotubes. Dielectric relaxation occurs due to different types of polarizations present in the material system. Each dielectric relaxation has a characteristic relaxation time and frequency. Figure 2.8 shows the different polarizations and their corresponding relaxation frequencies. These different polarizations are briefly summarized below[78];

a) Electronic polarization ($P_{electronic}$): This occurs due to the displacement of the electron density around the nucleus due to applied electric field. Figure 2.8 (a) shows the change in shape of the atom in response to the electric field.
b) Ionic polarization (P_{ionic}): is caused due to a separation of positive and negative ions by an applied field. Figure 2.8 (b) shows the separation between the ions under an applied field.
c) Dipolar polarization ($P_{dipolar}$): This is due to contributions of permanent and induced dipoles created due to the applied field. The orientation of dipoles under an applied field is demonstrated in Figure 2.8 (c)
d) Interfacial and space charge polarization ($P_{interfacial}$): Interfacial polarization is caused in a heterogeneous material due to ease in motion of charges through one phase compared to others. This leads to accumulation of charges at the component interface in a multi-component system. This process is demonstrated in Figure 2.8 (d).

Figure 2.8 (e) shows the dielectric relaxation dispersion in frequency of the different polarizations in polymers.

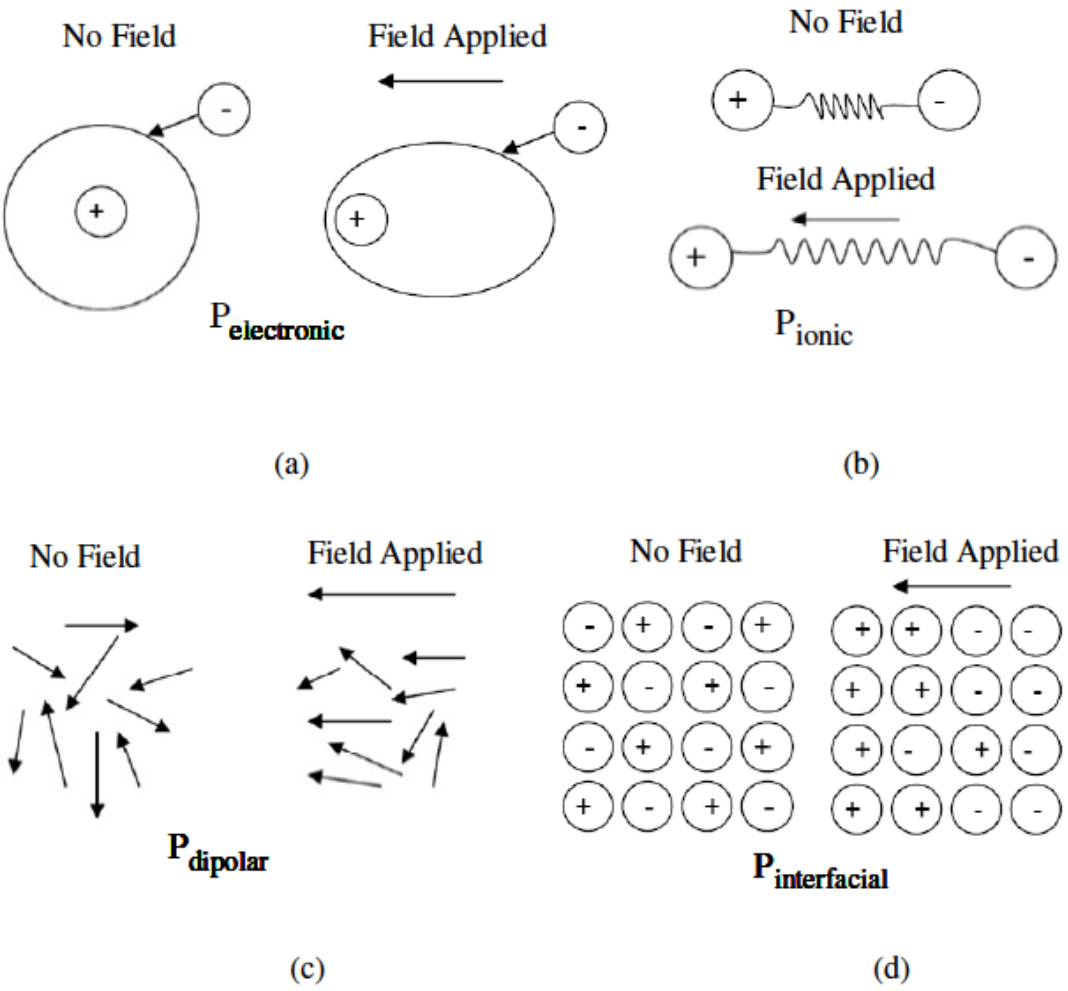

Figure 2.8 (a) Electronic polarization, (b) Ionic polarization, (c) Dipolar polarization, (d) Interfacial polarization and (e) Relaxation frequencies of different polarizations (adapted from [79, 80]).

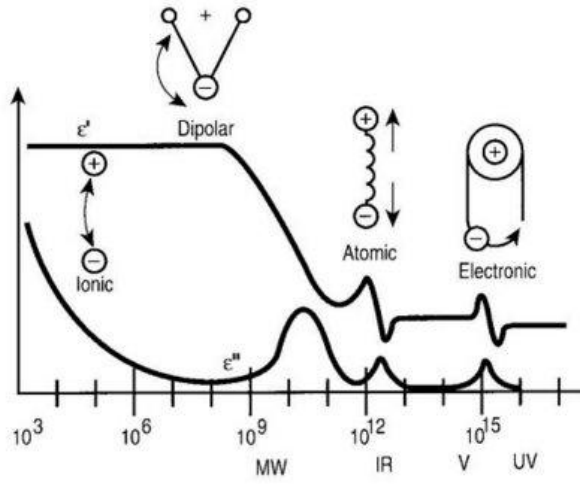

(e)

Figure 2.8 Continued.

Dielectric constant mapped as a function of temperature and thermally stimulated current (TSC) measurements are two methods used to detect and study the dielectric relaxation of the SWNT -polyimide composites. The dielectric relaxation resulting from movement of permanent and induced dipoles is called dipolar relaxation while that from the electric charges is called ionic relaxation. The first dielectric relaxation spectroscopy technique involves measuring the dielectric constant as a function of temperature at different frequencies using the Novocontrol broadband dielectric spectrometer or the combination of the Sun Systems environmental chamber and the QuadTech precision LCR meter. Characteristic relaxation time (τ) is defined as the time required for the dipoles or ions to return to their original configuration. The frequency at which this occurs is called the relaxation frequency. Relaxation in polymers is also temperature dependent. As temperature increases the polymer chains and the dipoles, if they are present, tend to relax.

The nanocomposite sample is held in a teflon holder with leads connected to the LCR meter. This setup is kept inside the environmental chamber. The temperature is varied within the chamber and the capacitance and loss factor are measured and then used to compute the real and imaginary parts of the dielectric permittivity. Alternatively

the samples are also tested over a range of temperatures using the Novocontrol broadband dielectric spectrometer with the Quatro temperature controller. The relaxation of the dipoles in a system is measured by the dielectric relaxation strength ,Δε,, which is the difference between the static (ε_s) and high frequency (ε_∞) limits on dielectric constant,

$$\Delta\varepsilon = \varepsilon_s - \varepsilon_\infty \tag{2.17}$$

Using the Clausius Mossotti equation,

$$\frac{N_0\alpha}{3\varepsilon_0} = \frac{\varepsilon' - 1}{\varepsilon' + 2} \tag{2.18}$$

where N_0 is the number molecules per unit volume, α is the polarizability, ε_0 is the permittivity of space and ε' is the dielectric constant of the material, the Onsager formula that defines the dielectric relaxation strength is then derived as[81, 82] ;

$$\Delta\varepsilon = \frac{N\mu}{3kT\varepsilon_0}\left(\frac{n^2+2}{3}\right)^2\left(\frac{3\varepsilon_s}{2\varepsilon_s + n^2}\right) \tag{2.19}$$

N is the number of dipoles per unit volume, k is the Boltzmann constant, T is temperature in K , n is the refractive index and $n^2 \approx \varepsilon_\infty$.This value also quantifies the remnant polarization. Polarization (P) is defined as;

$$P = (\varepsilon - 1)\varepsilon_0 E \tag{2.20}$$

Remnant polarization P_R is due to contributions by dipoles present in the system and is defined by,

$$P_R = P_s - P_\infty \tag{2.21}$$

P_s is the polarization at low frequency and P_∞ is that at high frequency and are given by;

$$P_s = (\varepsilon_s - 1)\varepsilon_0 E \tag{2.22}$$

$$P_\infty = (\varepsilon_\infty - 1)\varepsilon_0 E \tag{2.23}$$

where E is the applied electric field. The remnant polarization takes the linear form,

$$\begin{aligned} P_R &= (\varepsilon_s - \varepsilon_\infty)\varepsilon_0 E \\ &= \Delta\varepsilon\, \varepsilon_0 E \end{aligned} \tag{2.24}$$

The Δε value can also be measured by using temperature instead of frequency. The behavior of dipoles under high temperature is analogous to that at low frequency, while the value of dielectric constant at low temperature is analogous to that at high frequency (Figure 2.9). At low frequency the dipoles present in the system have a relatively high relaxation time and can be oriented as the fluctuations in the electric field are low but at high frequency these dipoles lag behind the high frequency field. Similarly, at high temperature the thermal energy provided to the system increases the mobility of the polymer chains and allows the dipoles to be oriented easily, similar to the low frequency case. At low temperatures the dipoles are difficult to move due to of the immobility of the polymer chains, possibly resulting in steric hindrances, and this condition is analogous to the high frequency case described earlier.

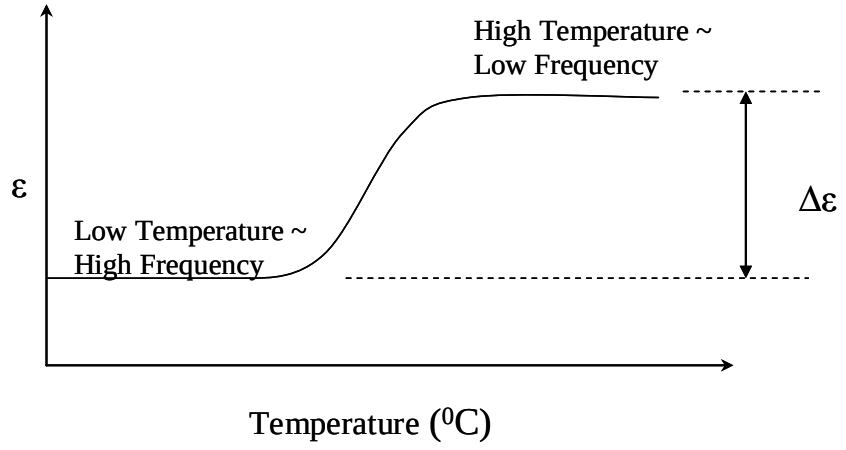

Figure 2.9 Dielectric constant as a function of temperature.

2.4.2 Thermally stimulated current measurements (TSC)

The thermally stimulated current (TSC) method was proposed by Bucci et al [83] in 1966. It has become a powerful tool for characterizing the dielectric relaxation phenomenon in polymers. The low frequency (equivalent to 10^{-3} to 10^{-4}Hz) results in a good resolution of the depolarization current spectrum, and a good sensitivity to different dielectric relaxations in the system under study. This makes TSC an attractive technique for detection of dipoles present, especially in polymers. The TSC techniques has been employed for different polymers like Poly(ethylene terephthlate) (PET)[84], Poly (vinyl chloride) (PVC) and Poly (methyl methacrylate) (PMMA)[85].

Figure 2.10 shows the Setaram TherMold TSC/RMA sample cell[86]. An electroded sample is sandwiched between metal disks, to which electrical contacts are made to allow poling of the sample and current measurement. The whole setup is placed in a controlled temperature chamber. The samples are usually vacuum dried and helium is pumped into the chamber to avoid arcing. The chamber is maintained at atmospheric pressure.

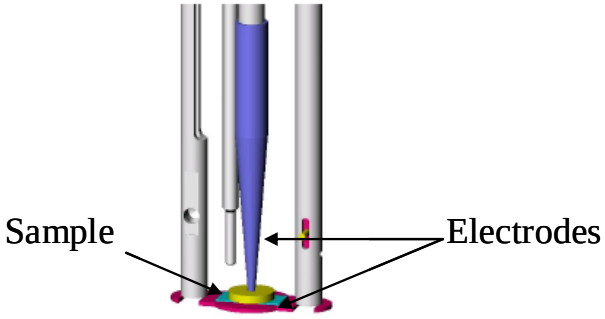

Figure 2.10 The TSC sample cell (adapted from[86]).

The general method used involves polarizing the sample at a static field, E_p, at the polarization temperature, T_p, in order to make sure the polarization reaches equilibrium (Figure 2.11). In the polymer or polymer nanocomposite case, the sample is poled by DC electric field around the glass transition temperature, T_g. The poling time is 20 minutes and is kept the same for all samples. The sample is then cooled rapidly to

room temperature using liquid nitrogen (with the electric field still on) and then re-heated slowly at a constant heating rate (1°C/min) to 300°C. Upon heating the chains slowly start to relax which in turn leads to the dipolar relaxation. A current (also known as the depolarization current) is recorded due to the return of the dipoles to equilibrium state. This current shows peaks as seen by an idealized case in Figure 2.12. These peaks in the measured current physically denote the dipolar reorientation due to the relaxation and are used to calculate the dielectric relaxation strength Δε and remnant polarization P_R[87, 88];

$$\Delta\varepsilon = \frac{1}{\beta}\int_{T_1}^{T_2} I(T)dT \tag{2.25}$$

$$P_R = \Delta\varepsilon\,\varepsilon_0 E = \int_{t_1}^{t_2} I(t)dt \tag{2.26}$$

β is the heating rate and T_1, T_2, t_1, t_2, are the initial temperature, final temperature, initial time and final time for the peak (as illustrated in Figure 2.12).

Thus dielectric constant as a function of temperature and TSC measurements are used to evaluate the dielectric relaxation phenomenon and the behavior of dipoles in the nanocomposite films.

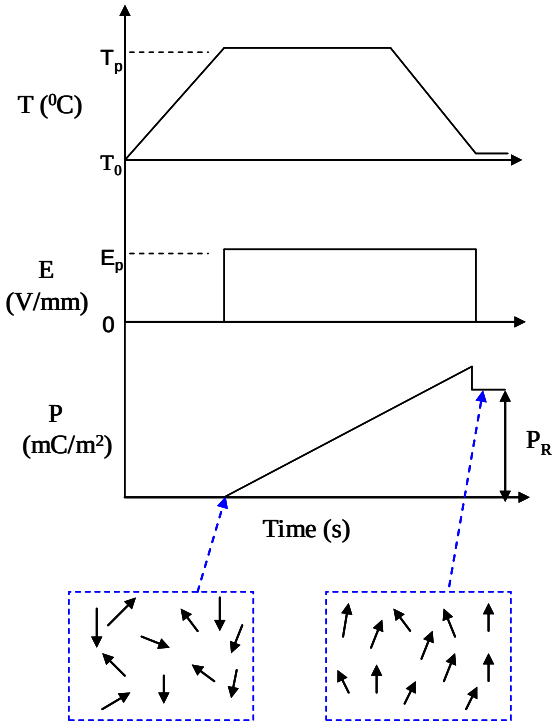

Figure 2.11 TSC poling cycle.

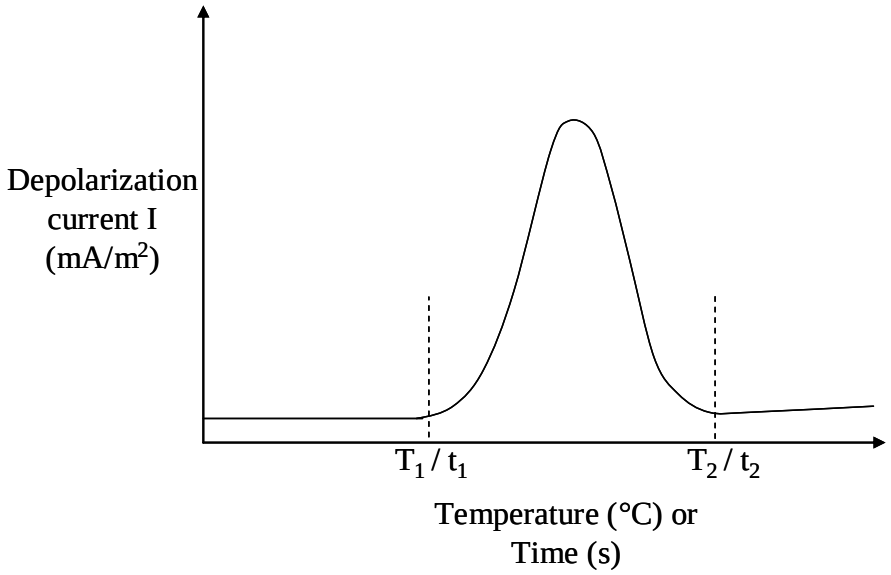

Figure 2.12 TSC heating cycle.

2.5 Thermal analysis

2.5.1 Differential scanning calorimetry (DSC)

The DSC is a thermal analytical tool that can detect thermal transitions like glass transition, fusion and crystallization in polymers. The DSC uses a reference pan and a sample pan on two heaters such that the pans are maintained at the same temperature. Any thermal transitions in the sample are detected due to more or less heat needed to maintain the sample at the same temperature as the reference pan. Figure 2.13 is a schematic of the DSC. Typical thermal transitions that occur in a semi-crystalline polymer are represented in Figure 2.14.

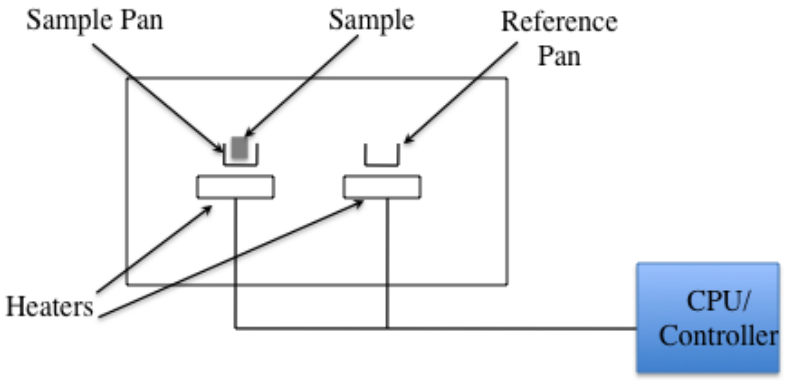

Figure 2.13 Schematic of a differential scanning calorimeter (DSC).

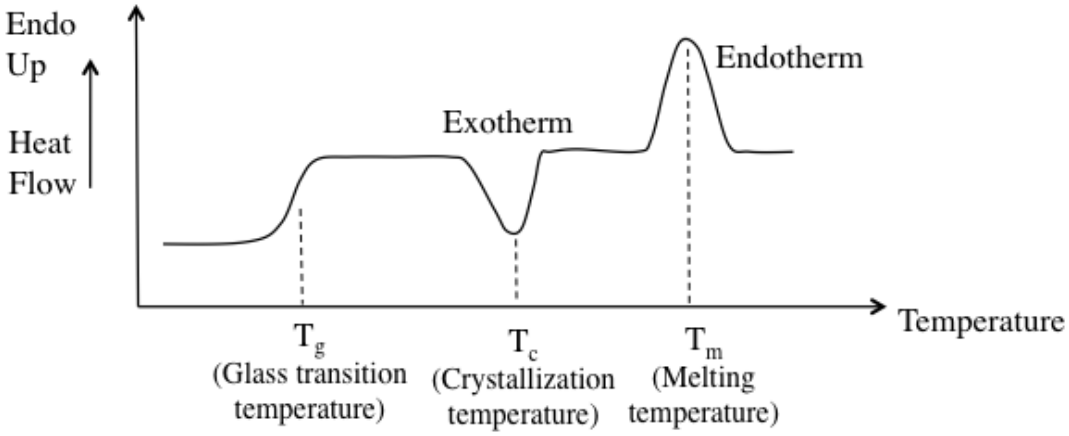

Figure 2.14 Schematic of thermal transitions in a semi-crystalline polymer.

As the semi-crystalline polymer is heated past its glass transition temperature (T_g) an increase in the heat flow is observed as the polymer demonstrates higher heat capacity above its glass transition temperature. During crystallization the sample gives out heat resulting in a decrease in the heat flow required to maintain the sample at the same temperature as the reference pan. On the other hand melting of crystallites requires more heat to maintain the sample at the reference temperature leading to increase in the heat flow. These transitions are represented by crystallization temperature (T_c) and the meting temperature (T_m) respectively (Figure 2.14). The percentage crystallinity is computed from the areas under the crystallization and melting temperature peaks. For example in the case of Figure 2.14 the percentage crystallinity is computed by:

$$\%\text{Crystallinity} = \frac{H_m - H_c}{H_m^* \cdot m} \tag{2.27}$$

Where H_m and H_c are the heat given out during melting and absorbed during crystallization respectively (Area under melting peak x mass of sample/Heating rate). H_m^* is the specific heat of melting and m is the total mass of the sample. The DSC used in this study is the TA instruments DSC Q20 and all tests are carried out at a heating rate of 10°C/min.

2.5.2 Thermo mechanical analysis (TMA)

The thermo-mechanical analyzer in this study is used primarily to measure the coefficient of thermal expansion of polymer and polymer nanocomposite films. A TA instruments Q400 thermo mechanical analyzer (TMA) is used with a tension fixture to measure the coefficient. The TMA measures the dimensions of the sample as a function of temperature as shown in Figure 2.15. The coefficient of thermal expansion (CTE) can then be measured from the slope of the plot.

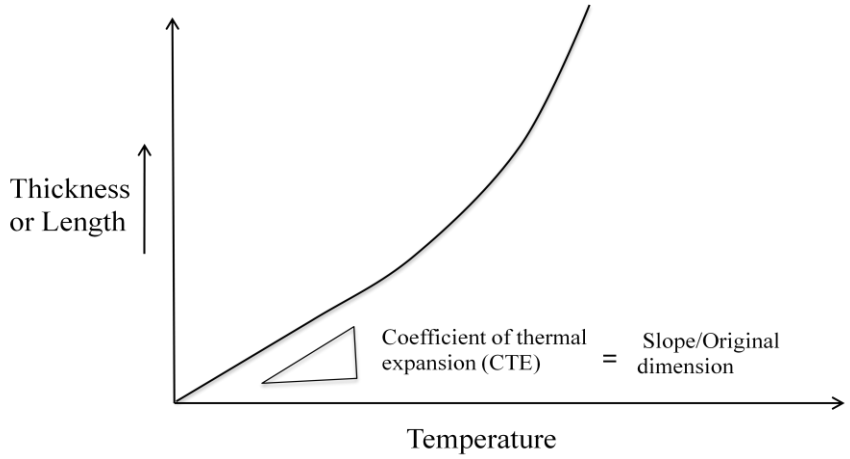

Figure 2.15 CTE measurement using TMA.

2.6 Fourier transform infrared spectroscopy (FT-IR) and Raman spectroscopy

Fourier transform infrared spectroscopy (FT-IR) is a popular non-destructive infrared spectroscopy technique for identifying different types of compounds and phases in materials. Infrared radiation is passed through the samples resulting in a unique pattern of absorption and transmission bands. Unique molecular structures have their own unique infrared spectrum that can be used for identifying the materials along with their amount. Thermo Electron Corporation Nicolet 380 is employed in two different modes for this study: Transmission and Attenuated Total Reflection (ATR). Transmission FT-IR is ideal but requires thin and transparent samples for a clean spectrum (Figure 2.16). The ATR mode requires only a few microns of depth of

penetration for the incident radiation and hence is preferred for thick and semi-transparent samples (Figure 2.17). In this study FT-IR is used to probe the microstructure and content of different crystalline phases of the PVDF nanocomposite samples.

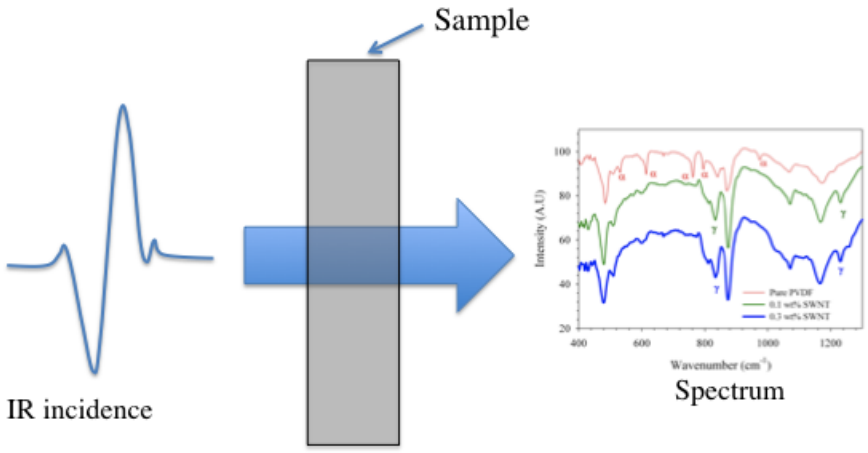

Figure 2.16 Transmission FT-IR.

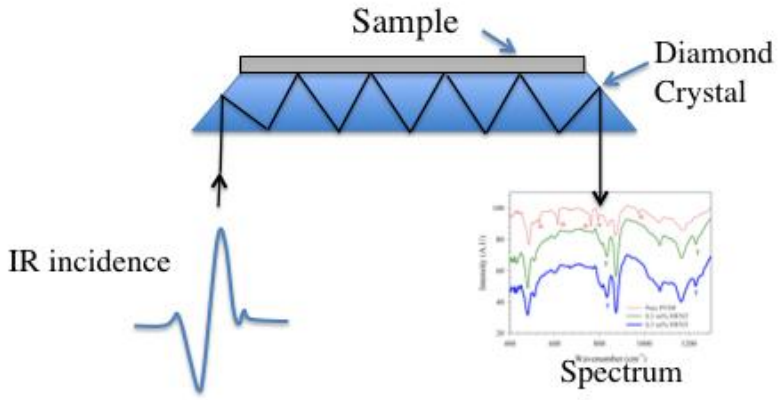

Figure 2.17 FT-IR – ATR.

A Nanonics Multiview 400 Raman spectrometer employing a JY Horiba 532 nm laser is used to probe the interaction between the polymer and SWNTs and also to determine structural changes in the SWNTs during actuation. To probe the interaction between SWNTs and the polymer matrix, different vibrational breathing modes of

SWNTs are studied in the pristine state and in nanocomposite samples. For studying the effect of electric field on SWNTs in polymer nanocomposites, silver electrodes are patterned on the surface of high content SWNT samples and the effect of DC field is observed on the breathing modes of SWNTs. Any changes in the breathing modes of SWNTs signify structural changes and in turn can indicate the presence of interaction between SWNTs and polymer matrix as well as strains due to electromechanical actuation.

2.7 Wide angle X-ray scattering (WAXS)

Wide angle powder X-ray diffraction is employed in this study to confirm the type of crystalline microstructure in the PVDF and SWNT-PVDF nanocomposite samples. WAXS data is collected using a Bruker-AXS D8 Advanced Bragg-Brentano X-ray Powder diffractometer over the 2θ range of 10° - 70°.

2.8 Dynamic mechanical analysis (DMA)

A TA instruments RSA III dynamic mechanical analyzer is used in this study to measure the storage modulus of the nanocomposite samples. Storage modulus, loss modulus and tan δ are measured using a thin film fixture. All tests are carried out at 1 Hz frequency. The storage modulus, measured as a function of SWNT loading, is used to calculate the work and energy densities of the nanocomposite actuators.

2.9 Scanning electron microscopy (SEM)

A FEI Quanta 600 field emission scanning electron microscope (FE-SEM) with a Schottky emitter and a Everhart-Thornley secondary electron detector is used in this study. A Pt-Pd coating of 5 nm is used on the nanocomposite samples. A working distance of approxmately 10 mm is used along with accelerating voltages between 5 – 20 kV. The SEM is used to probe the dispersion of SWNTs in the polymer nanocomposites along with any possible interaction between the SWNTs and the polymers. Additionally

the SEM is also used to probe the crystalline microstructure and its evolution in PVDF in the presence of SWNTs. A Zeiss 1530 high resolution FE-SEM is also used in this study.

3. ELECTROMECHANICAL RESPONSE OF SWNT-CP2 NANOCOMPOSITES*

3.1 Dispersion of SWNT – CP2 nanocomposites

The SWNT-CP2 composites are prepared by *in-situ* polymerization under sonication in a process developed by researchers at NASA Langley Research Center[30, 52]. This procedure includes ultrasonication to efficiently pre-disperse the SWNTs in dimethylformamide (DMF) solvent, then mechanical stirring in subsequent steps. Polymerization takes place between the diamine and dianhydride constituents that are mixed in the presence of the pre-dispersed SWNT solution while bath sonicating at 40 kHz sonication. The viscosity of the solution increased with the nanotube content. Mechanical stirring along with sonication was employed to get well dispersed films. It is important to note that the SWNTs used are as-produced without any surfactants or chemical functionalizations.

The two key factors in judging the quality of the nanocomposites are the dispersion of the nanoinclusions in the polyimide matrix and their adhesion to it. Previous studies on these SWNT- CP2 nanocomposites [30, 52, 89] have shown a good dispersion using transmission electron microscopy (TEM) and optical microscopy.

Figure 3.1 shows SEM images of 0.5% and 2% SWNT - CP2 nanocomposite fracture surfaces. Figure 3.1(a) shows nanotubes evenly dispersed in the sample showing good dispersion but they do not appear anchored in the polymer. Figure 3.1 (b) shows evidence of polymer wetting of the nanotubes. Thus though there is some evidence of adhesion between the nanotube and polymer it does not appear strong in nature and can be attributed to lack of any strong affinity between the SWNTs and the CP2.

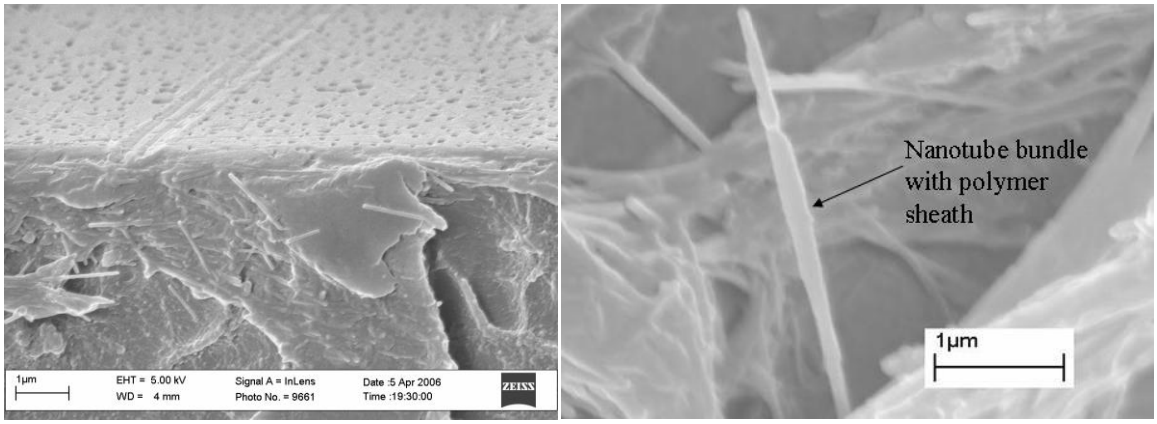

(a) (b)

Figure 3.1 (a) SEM of 0.5%SWNT+CP2 showing the SWNTs not anchored in the polymer (b) SEM images of 2%SWNT+CP2 showing polymer wetting of the nanotube.

Electrical conductivity data is used to calculate the percolation threshold and quantify the dispersion state of SWNTs. The plot of average electrical conductivity as a function of SWNT concentration is shown in Figure 3.2 (it is noted that each point is extrapolated to DC). The conductivity is linear with $(v\text{-}v_c)$ on a logarithmic scale described by the equation:

$$\mathrm{Log}\,\sigma = \mathrm{LogA} + \mathrm{Log}[(v - v_c)]^t \qquad (3.1)$$

where σ is the conductivity of the nanocomposite, v is the volume fraction of the SWNT in the nanocomposite, v_c is the volume fraction at percolation , A and t are fitted constants. A best fit to the data results when $A = 5 \times 10^{-2}$ S/cm and t = 1.71, resulting in a v_c = 0.04vol%. This fit is shown in the inset of Figure 3.2.

The SWNT – CP2 nanocomposites show excellent dispersion that can be attributed to the in-situ polymerization under sonication technique used in the study. However it is also evident that there is an absence of any strong affinity between the SWNTs and the CP2 polyimide.

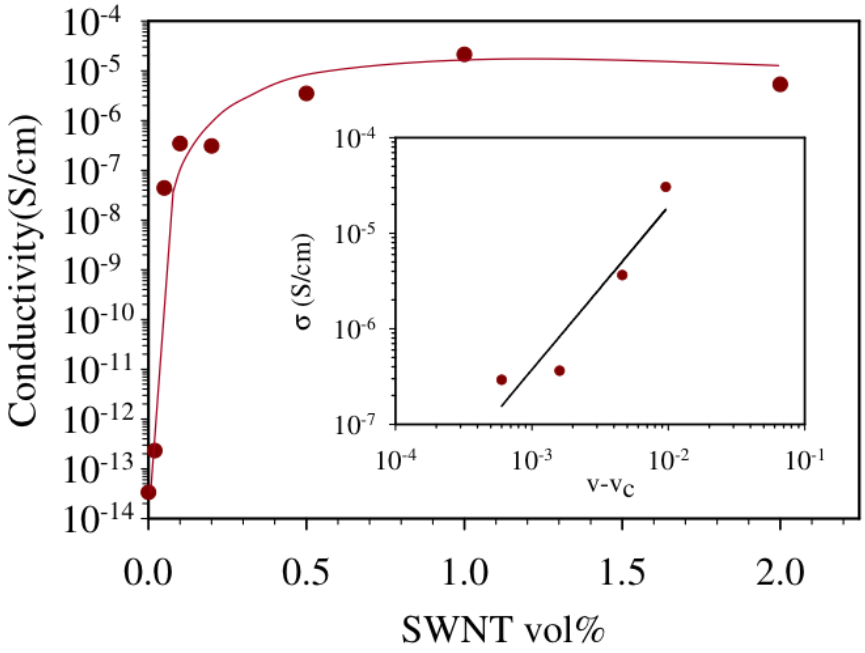

Figure 3.2 Variation of conductivity with SWNT loading (the solid line in the main figure is added to ease the reading of the data; the solid line in the inset is the linear trend exhibited by the data).

3.2 Thickness actuation

A fiber optic sensor is employed to measure the out-of-pane or transverse strains in the nanocomposite samples on application of DC and AC electric fields. It is noted that nanocomposites below the percolation threshold do not show any significant actuation response, whereas samples above percolation exhibit strains in response to applied voltage. For the thickness experiment (see Figure 2.4)), the transverse strains are calculated by the measured change in the thickness (Δt),

$$S_{33} = \frac{\Delta t}{t} \tag{3.2}$$

Transverse strains S_{33} for composites with 0.1vol%, 0.5vol%, 1vol% and 2vol% SWNT loadings are plotted in Figure 3.3. The data is collected at 1 Hz frequency. The strains increase non-linearly with the magnitude of electric field as seen in Figure 3.3(a). A striking observation is the low magnitude of electric fields required for actuation; the magnitude of the field is one to three orders lower than that required for other

electrostrictive polymers like polyurethane[90] and poly(vinylidene fluoride-trifluoroethylene) [64]. We also see an enhancement in the actuation response as the SWNT loading increases from 0.1 to 1vol%. At 2vol% SWNT loading however, the nanocomposite shows a decrease in strain compared to 1vol% SWNT loading sample. This can be attributed to SWNT agglomeration in the 2vol% SWNT samples. This is reflected in lower conductivity for 2 vol% samples compared with that for 1 vol% SWNT samples shown in Figure 3.2. Figure 3.3(b) depicts the dependence of the electromechanical strains on the square of the electric field, where the solid lines are linear fits with R^2 values in the range of 0.94 - 0.97.

3.3 Bending actuation

For the bending experiment, a sample strip with silver electrodes on both faces is suspended vertically as a cantilever with an electric field applied through the thickness. The length extensional strain resulting from bending is computed by modeling the bent strip as a cantilever beam under a uniform bending moment thus assuming a constant radius of curvature (see Figure 2.5).

Using Hookes law the strain at each point along the length would be constant and equal to;

$$S_{11} = \frac{w \cdot t}{L^2} \tag{3.3}$$

The strain S_{11} is measured along the length (1-direction) due to an electric field applied through the thickness (3-direction). In a separate study, Sellinger et al[91] have demonstrated the presence of a thin polyimide skin in the nanocomposite actuators that acts as a constraining layer and consequently results in a bending actuation response. The thickness of the thin skin can be as low as of the order of 50 nm. This layer results from the casting process used for the polymer films, where the solution is poured on the glass slide, as a wall depletion effect takes place[92, 93]. The other surface (air surface) is SWNT-rich and has a rough texture.

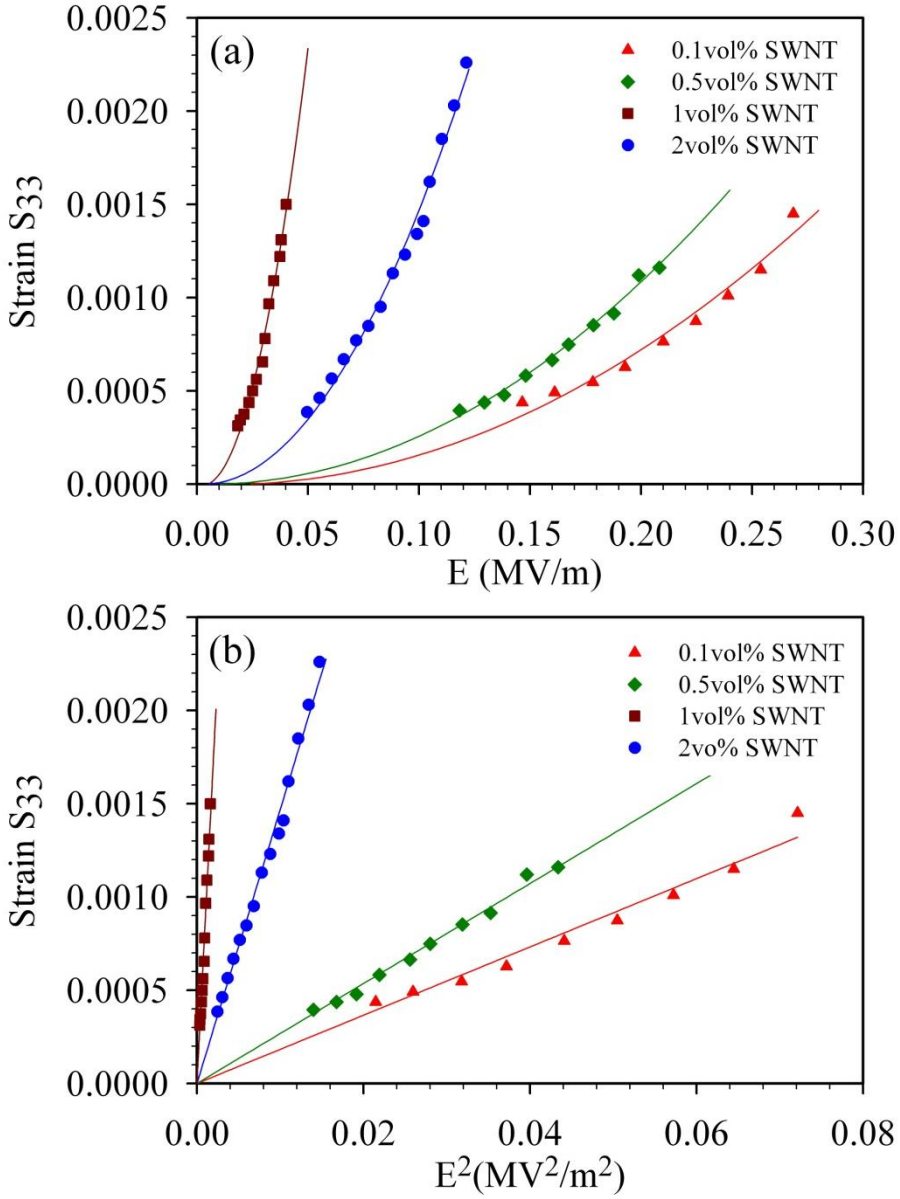

Figure 3.3 (a) Transverse strains as a function of AC electric field (1 Hz) and SWNT content. (b) Transverse strains proportional to squared electric field. Solid lines are quadratic fit for (a), and linear for (b).

Length extensional strains S_{11} for the composites under DC and AC fields are shown in Figures 3.4 and 3.5 respectively. Similar to thickness actuation case, the electric field magnitudes required in the bending experiment are very low. Also, the strains are proportional to the square of the electric field as can be seen in Figures 3.4(b)

and 3.5(b). Finally, the bending actuation response increases with the SWNT loading up to 1vol% SWNT content, above which a decrease is seen which could be attributed to possible agglomerations in the 2vol% SWNT samples.

3.4 Strain rate

We also investigated the strain rate associated with S_{11}, i.e., how quickly the strain reaches its maximum value under an applied electric field. Figure 3.6 shows strain as a function of time at different DC voltages for 0.5vol% SWNT loading. The strain increases linearly after an initial lag of a few seconds, and then plateaus off. A higher strain rate is seen with an increase in the applied voltage. Similar observations are made at different vol% SWNT loading. Table 3.1 summarizes some of these results. From the table it can be inferred that higher SWNT loading samples demonstrate higher strain rates at lower electric fields. Thus, the strain rate increases with increase in voltage and SWNT loading.

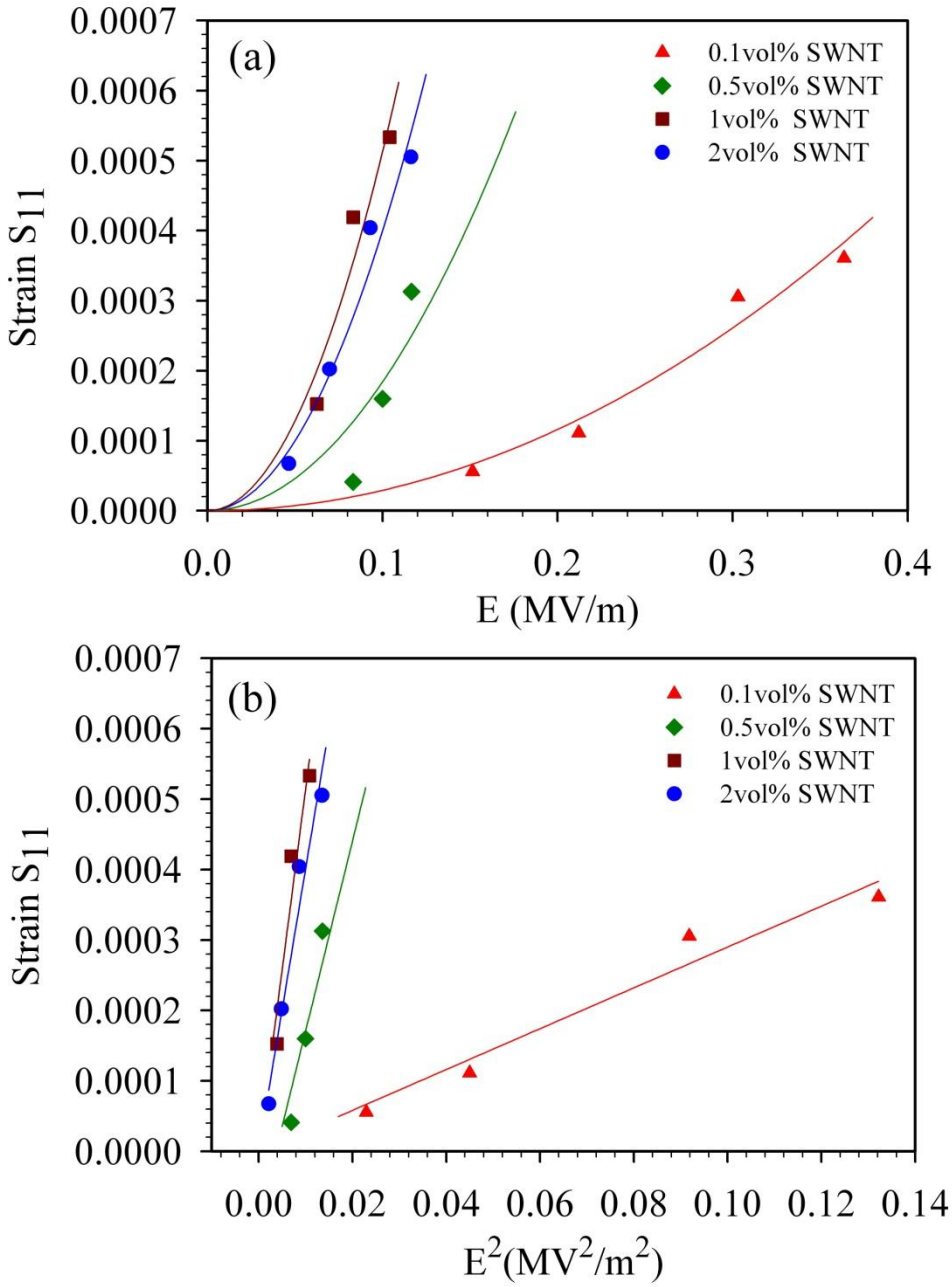

Figure 3.4 (a) Longitudinal strains as a function of DC electric field and SWNT content. (b) Longitudinal strains proportional to squared electric field. Solid lines are quadratic fit for (a), and linear for (b).

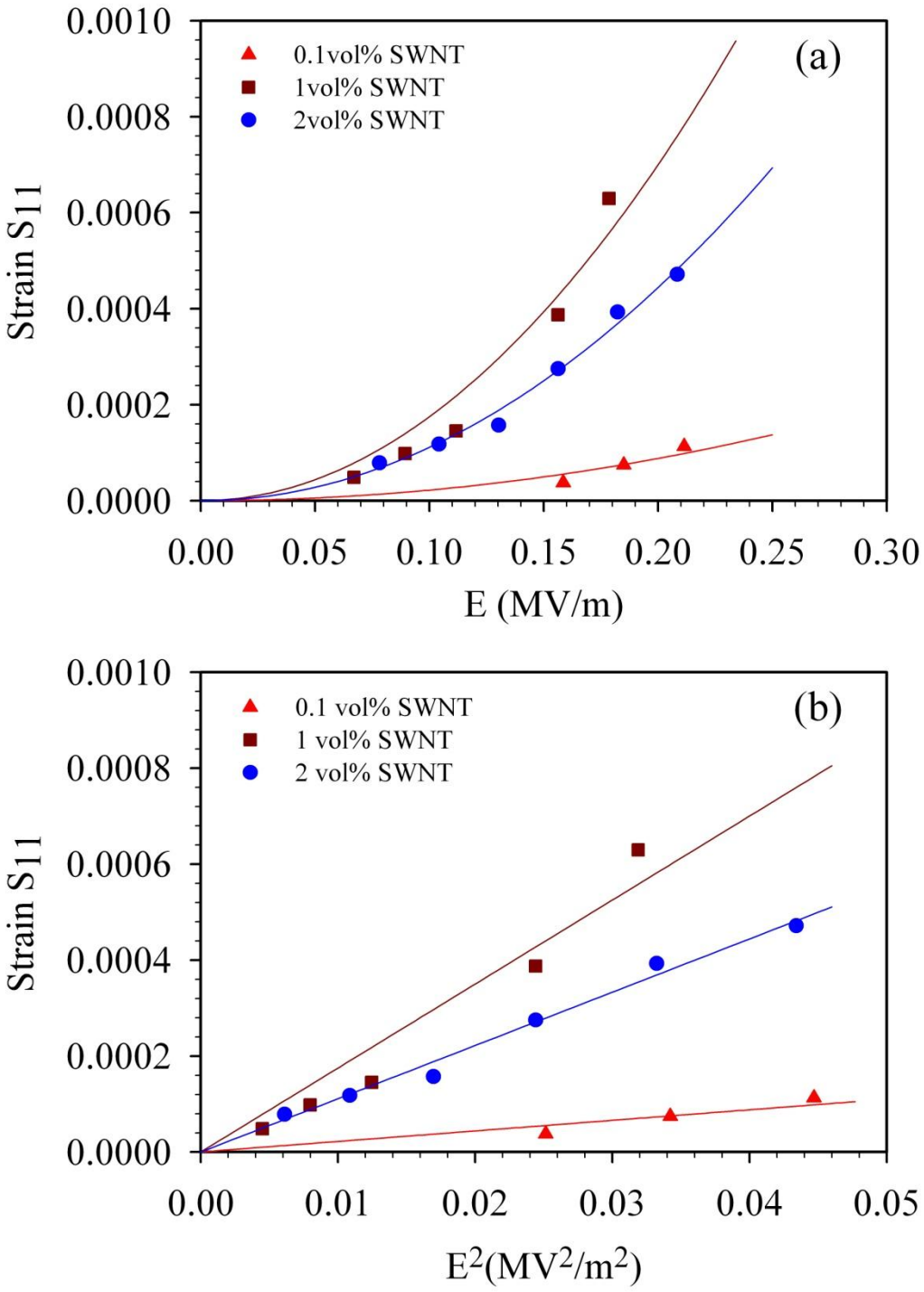

Figure 3.5 (a) Longitudinal strains as a function of AC electric field (0.5 Hz) and SWNT content. (b) Longitudinal strains proportional to squared electric field. Solid lines are quadratic fit for (a), and linear for (b).

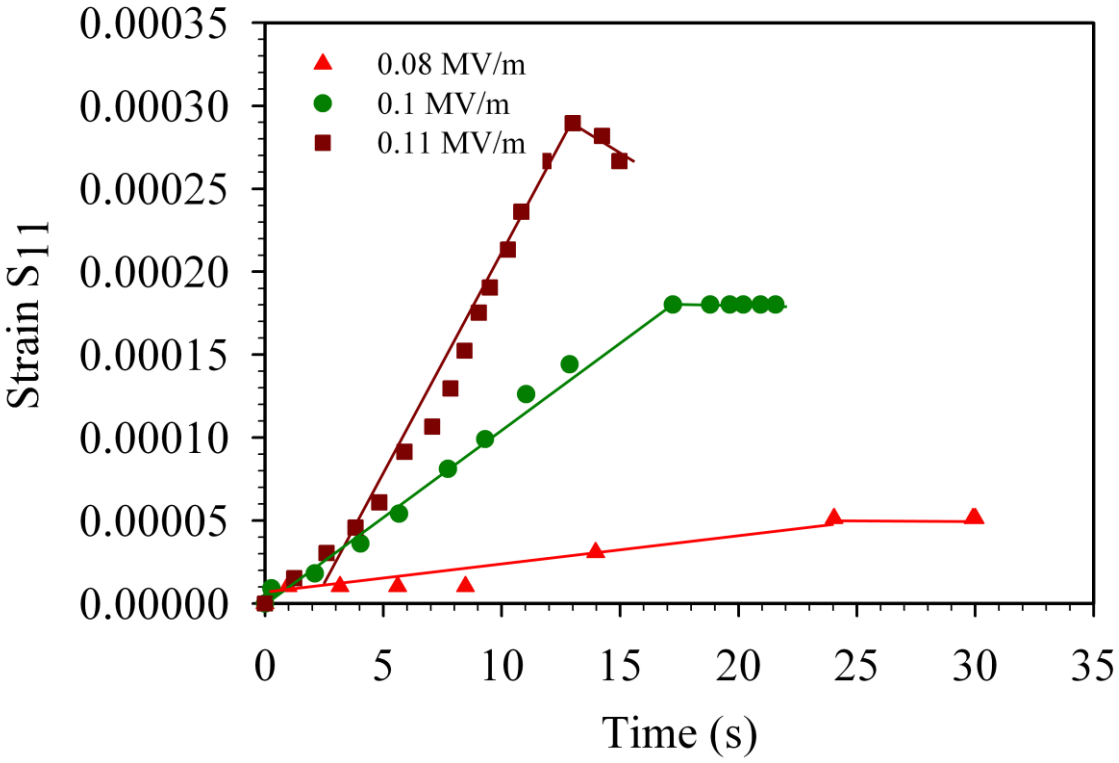

Figure 3.6 S_{11} strain rates compared at different voltages for 0.5 vol% SWNT- CP2.

Table 3.1 Strain rates at different SWNT content and applied voltages.

Electric Field (MV/m)	Strain Rate (s^{-1})	
	0.1vol% SWNT	0.5vol% SWNT
0.08	-	4×10^{-6}
0.1	-	2×10^{-5}
0.11	2.2×10^{-5}	8.9×10^{-5}

3.5 Quadratic electromechanical response

Both S_{33} and S_{11} strains show a quadratic dependence on electric field. This can be seen in Figures 3.3 (b), 3.4 (b) and 3.5 (b). This quadratic response can also be observed visually:

a) In thickness actuation experiments, the samples always expand in thickness in the consecutive half cycles of the applied sinusoidal AC field.
b) In bending actuation experiments, the samples always bend in the same direction irrespective of the sign of the applied electric field in DC case and the consecutive half cycles in the AC case.

In general, the strain response of a sample S_{ij} under an applied stress T_{ij}, electric field E_i and temperature change ΔT can be expressed as;

$$S_{ij} = s_{ijkl}T_{kl} + d_{ijk}E_k + M_{ijkl}E_kE_l + \alpha_{ij}\Delta T + \text{higher order terms} \quad (3.4)$$

s_{ijkl}, M'_{ijkl}, d_{ijk} and α_{ij} are the compliance, coefficient of electrostriction, piezoelectric strain coefficient and coefficient of thermal expansion respectively. The SWNT-CP2 nanocomposite samples are unpoled centro-symmetric non-piezoelectric materials. No external stress is applied to the samples before or during the actuation tests. Also, any change in temperature of the samples would result from resistive heating (Joule heating) phenomenon and show a quadratic dependence on electric field. Hence the quadratic strain response can be expressed in the most general form as:

$$S_{ij} = M_{ijkl}E_kE_l \quad (3.5)$$

M_{ijkl} in equation 3.5 is the quadratic electromechanical coefficient that can encompass three mechanisms:

i) Electrostriction
ii) Electrostatic strains or Maxwell's stress driven strains
iii) Joule heating

3.5.1 Quadratic electromechanical coefficients

The quadratic electromechanical coefficients M_{3333} and M_{1133} are calculated from the strain vs. squared electric field plots for a minimum of three samples. Figure 3.7

compares the coefficients for our composites with known electrostrictors like polyurethane and PVDF copolymer P(VDF-TrFE). M_{3333} at 1 Hz shows an increase with SWNT content up to 1vol% SWNT above which we observe a decrease in the value. Similarly an increase in the M_{1133} coefficient for the DC case up to 1vol% SWNT is observed, above which, the value plateaus off. Under AC field, the M_{1133} values are lower than in the DC case. In general, the coefficients of electrostriction for the SWNT-PI composites are six to eight orders higher than those shown in electrostrictive Polyurethane [94] and PVDF-TrFE [64].

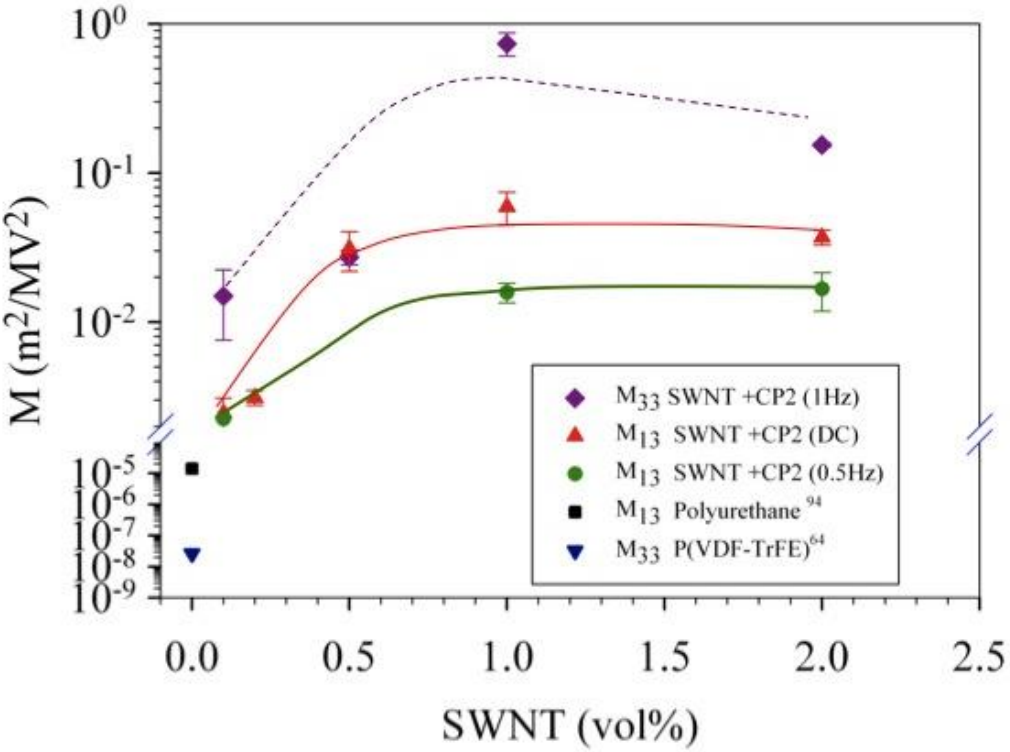

Figure 3.7 Comparison of quadratic electromechanical coefficients. Lines are drawn to ease the reading of the data.

3.5.2 Contributions to quadratic electromechanical response

This section investigates the contributions to M_{ijkl} from SWNT actuation, electrostatic strains, electrostriction and Joule heating.

3.5.2.1 SWNTs

As discussed in the introduction SWNTs can demonstrate electromechanical properties including electrostriction. Both El-Hami et al[24] and Guo et al[25] have concluded that SWNTs exhibit an electrostrictive behavior. However, the coefficient of electrostriction measured in [24] is a low $2x10^{-6}$ m^2/MV^2, which does not account for the high electrostrictive coefficient seen in Figure 3.7. However the contributions to the electromechanical strains from SWNTs need to be probed especially at high SWNT content. Previous studies have demonstrated shifts in the G band frequency of SWNTs under strains, individually[95, 96], or in a composite[97]. Strains as low as 0.06% in the SWNTs can be detected using Raman spectroscopy[95, 96]. To study this possibility we conducted in-situ Raman spectroscopy while applying a DC electric field during a thickness actuation experiment. The DC electric fields used were the same magnitudes as used in the actuation data discussed earlier. The DC voltage is increased until the breakdown of the sample is reached while consistently gathering the Raman spectrum at multiple points. Figure 3.8 (a) shows a schematic of the setup used and 3.8 (b) shows the tangential breathing mode peak of SWNTs before and after applying a DC voltage for a 2vol% SWNT sample. No change in the vibrational frequencies of SWNTs is observed. This result confirms minimal structural changes in the SWNTs and in turn minimal strain contributions under applied electric field, most likely due to the low electric field used and possible constraining effect of the rigid polymer matrix.

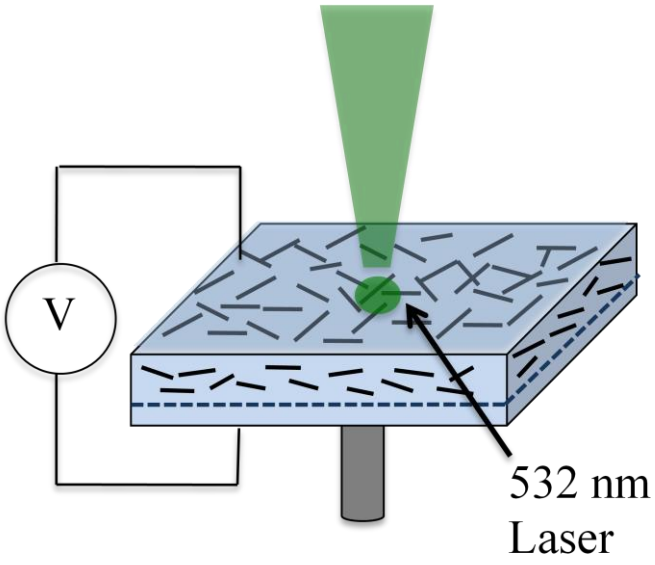

(a)

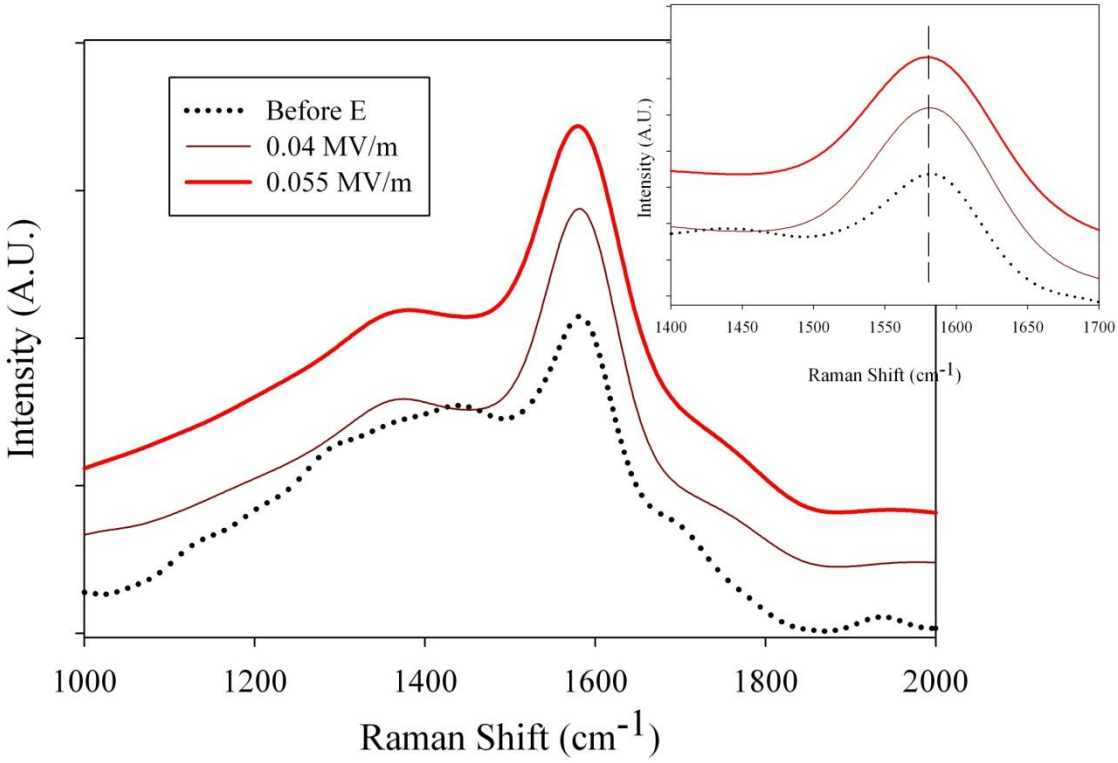

(b)

Figure 3.8 (a) In-situ Raman setup during thickness actuation, (b) In-situ Raman spectrum before and after applied DC electric fields.

3.5.2.2 Electrostriction

As mentioned earlier, electrostriction is a quadratic electromechanical response. Electrostriction is also a polarization driven phenomenon. In the absence of piezoelectric contributions, and higher order terms, electrostrictive strains can be expressed as a function of polarization as[78]:

$$S_{ij} = Q_{ijkl} P_k P_l \tag{3.6}$$

P_k and P_l are the polarization vectors and Q_{ijkl} is the coefficient of electrostriction associated with polarization. Most dielectric materials are linear dielectrics where the applied field and the resulting polarization are linearly related. Polarization can then be expressed in terms of the electric field as[98],

$$P_i = \varepsilon_0(\varepsilon_{ij} - 1)E_j \tag{3.7}$$

Where ε_0 and ε_{ij} are the permittivities of space and the dielectric material respectively. Hence the electrostrictive strain can then be written in terms of the electric field vectors E_r and E_s as[98],

$$S_{ij} = M_{ijrs} E_r E_s \tag{3.8}$$

Where M_{ijrs} is the electrostriction coefficient related to the electric field. The two coefficients are related to each other through,

$$M_{ijrs} = \varepsilon_0(\varepsilon_{kr} - 1)(\varepsilon_{ls} - 1)Q_{ijkl} \tag{3.9}$$

Figure 3.9 shows the effective dielectric constant at different SWNT vol%. A high value is seen above the percolation threshold. The value increases until 0.5vol% SWNT content above which the value plateaus off. It is believed that the increase in the dielectric constant is indicative of an enhanced polarization in the nanocomposite samples.

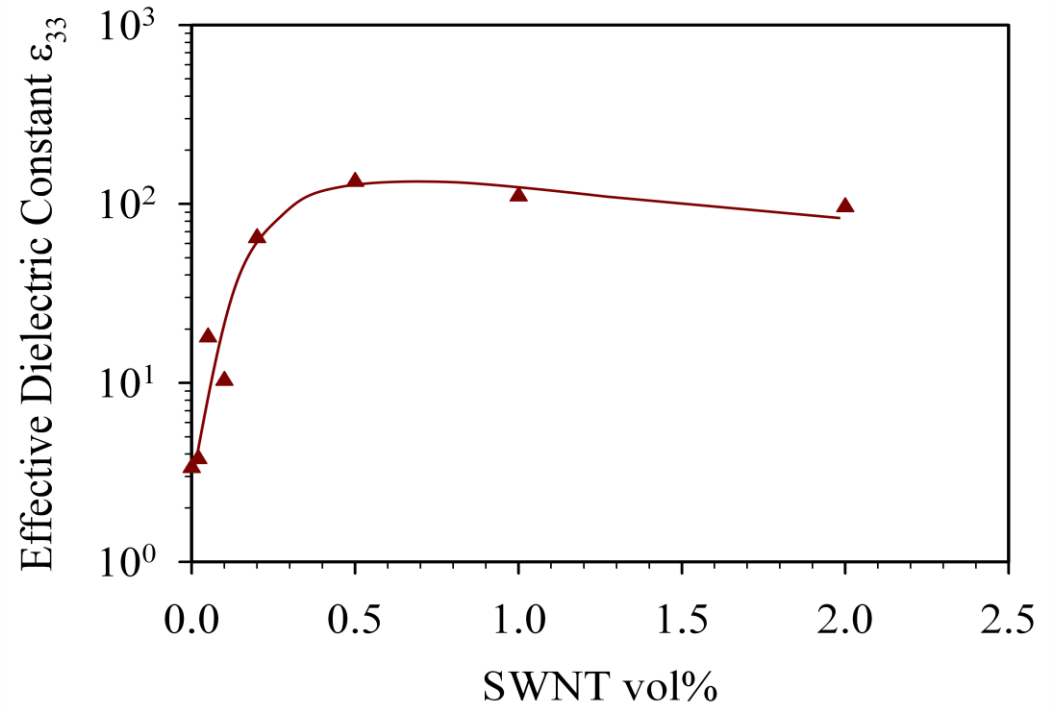

Figure 3.9 Dielectric constant vs SWNT content.

Since electrostriction is a polarization dependent phenomenon (Equation 3.4), results of thermally stimulated current (TSC) and dielectric relaxation experiments offer an explanation to this emergence and enhancement of the actuation response. Figure 3.10 shows the depolarization current per unit area for 0.05 vol% SWNT-PI and 0.1 vol% SWNT composites obtained from TSC. The area under the peaks corresponds to the polarization induced in the composites. Inspection of Figure 3.10(a) shows that the 0.1 vol% composite has a higher polarization as compared to the 0.05 vol% composite. Figure 3.10(b) summarizes the polarization for three different samples: pure CP2, 0.05vol% SWNT+PI and 0.1vol% SWNT samples at the same poling temperature of 200°C (glass transition of the system, which remains unchanged with addition of SWNTs[30]) but different poling fields. An increase is observed in the induced polarization with the SWNT content and poling field. Effect of poling temperature was also investigated for 0.1%SWNT samples and a higher polarization (2-4 factors) is seen for

poling temperatures at 200°C compared to that at 180°C and 190°C as shown in Figure 3.11.

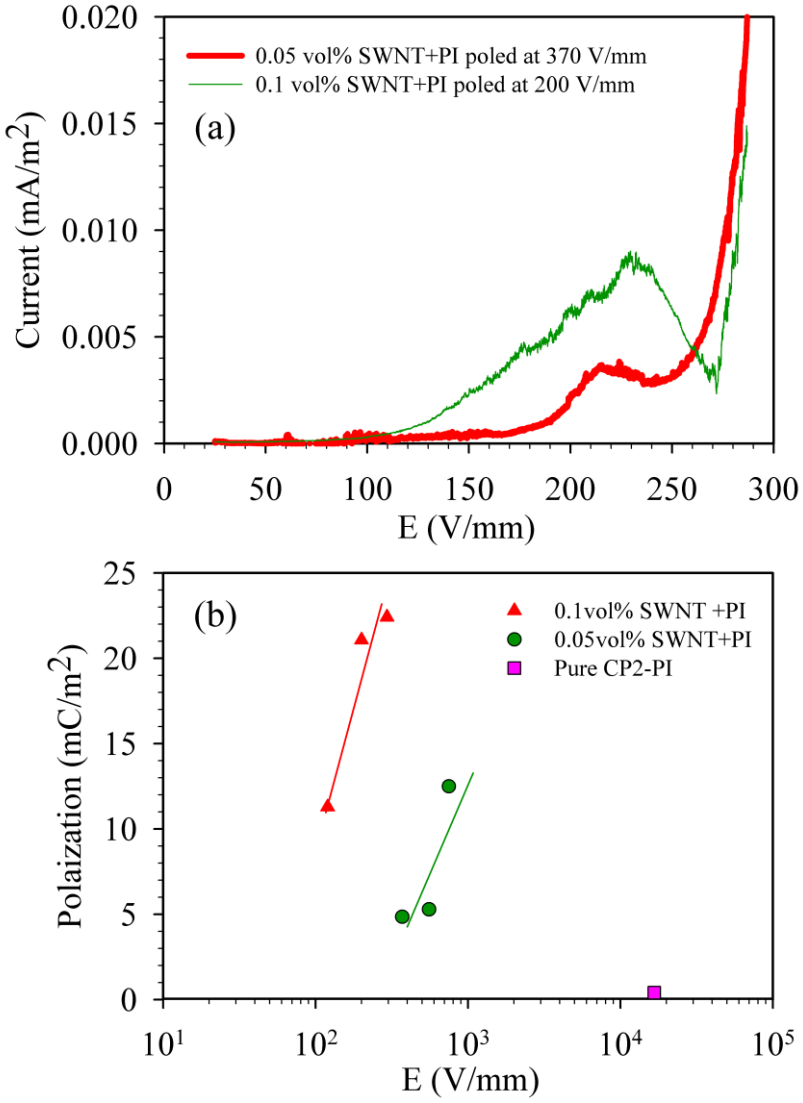

Figure 3.10 (a) Depolarization current as a function of temperature for 0.05 vol% and 0.1 vol% SWNT samples. (b) Polarization induced in the nanocomposites by TSC with varying SWNT loading compared to pure polyimide. Solid lines are used to ease the reading of the data.

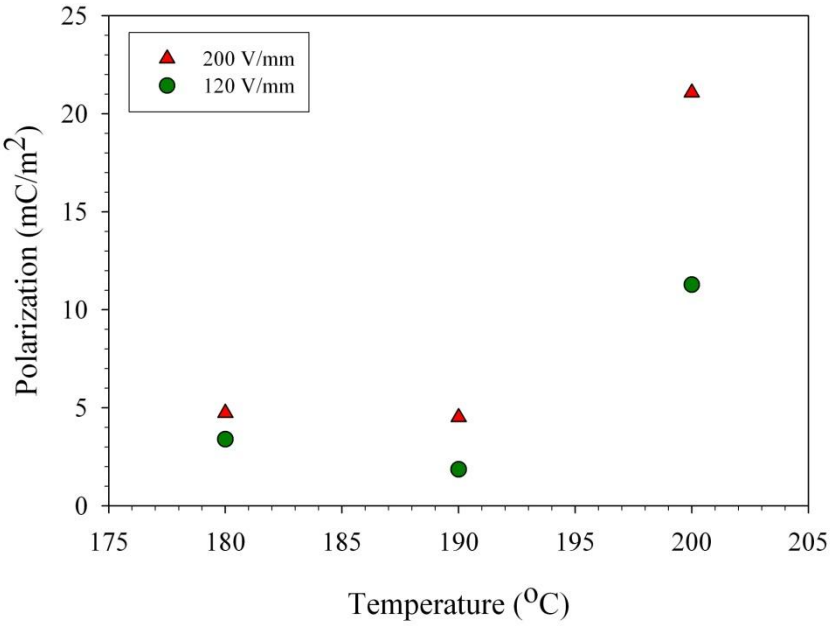

Figure 3.11 Polarization as a function of poling temperature for 0.1%SWNT-CP2.

The remnant polarization, polarization due to permanent dipole contributions, is given by the Clausius Mossotti equation[99]:

$$P_R = \Delta\varepsilon\, \varepsilon_0\, E \qquad (3.10)$$

where, ε_0 is the permittivity of free space, E is the applied electric field, and $\Delta\varepsilon$ is the dielectric relaxation strength which is the difference between the static (low frequency) and high frequency limits on dielectric constant. The $\Delta\varepsilon$ value can also be measured by using temperature instead of frequency. The behavior of dipoles under high temperature is analogous to that at low frequency, while that at low temperature is analogous to the behavior at high frequency. Figure 3.12 shows the increasing difference between the high and low temperature values of dielectric constant ($\Delta\varepsilon$) for different SWNT loading at 21.5Hz. This value increases with SWNT loading as seen in Table 3.2, indicating an increase in the dipolar relaxation and remnant polarization with SWNT loading. Both Figure 3.10 and Table 3.2 confirm the presence of dipolar polarization in CP2 in the presence of SWNTs. The enhancement in polarization due to the presence of SWNTs

strongly indicates that the quadratic electromechanical response is electrostriction. Figure 3.13 shows the predicted remnant polarization based on the dielectric relaxation strength according to equation (3.10). The remnant polarization increases with SWNT content.

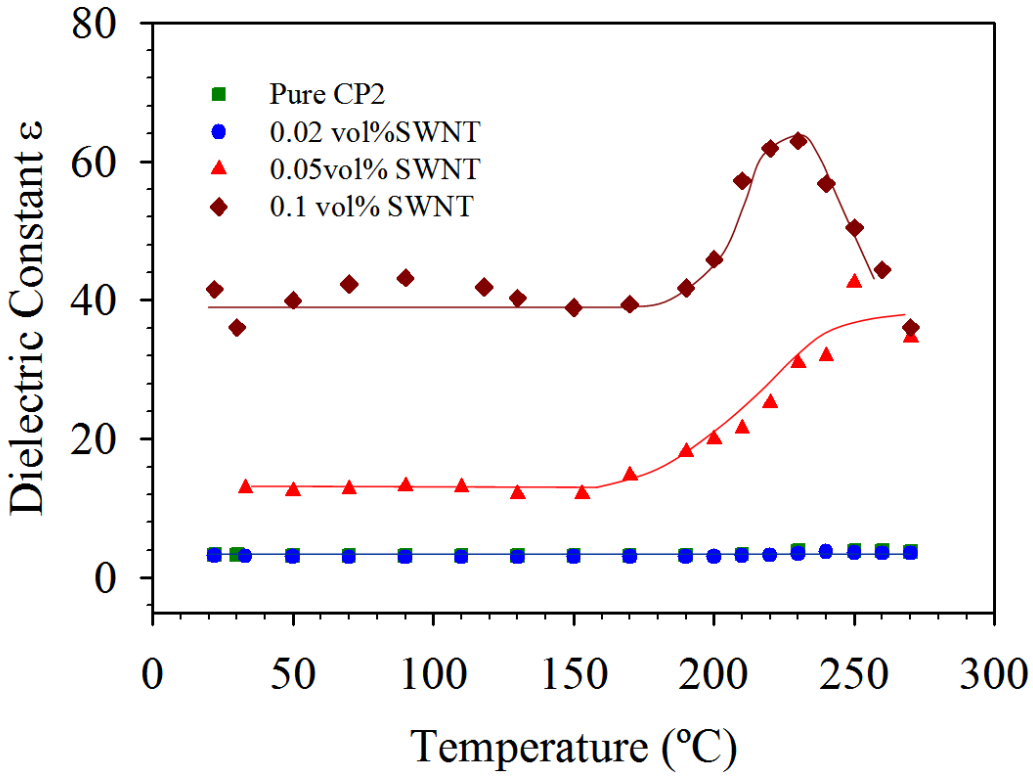

Figure 3.12 Dielectric constant as a function of temperature at 21.5Hz showing dipolar relaxation at different SWNT content. *Note*: data for pure CP2 and for the 0.02 wt.% nanocomposites overlap.

Table 3.2 $\Delta\varepsilon$ as a function of SWNT loading.

SWNT loading (Vol%)	$\Delta\varepsilon_{21.5\ Hz}$
0	0.69
0.02	0.72
0.05	21
0.1	24

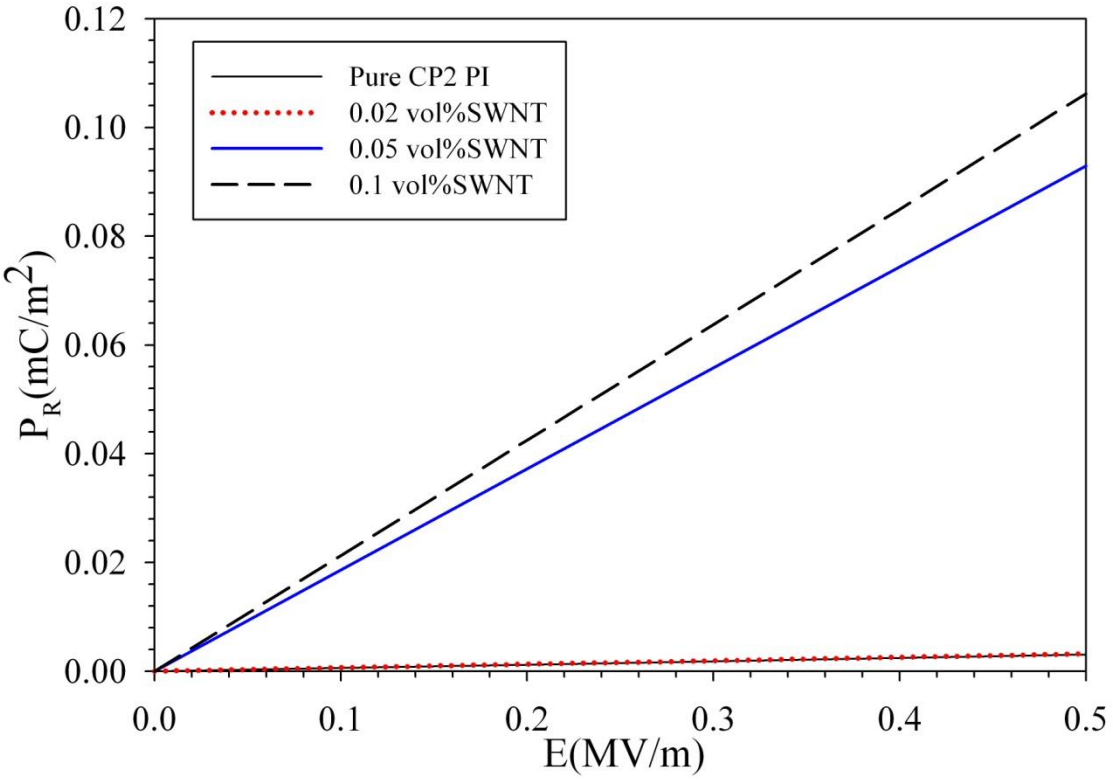

Figure 3.13 Remnant polarization predicted for SWNT - (β-CN) APB-ODPA nanocomposites for the actuation electric fields used.

3.5.2.3 Electrostatic actuation

Electrostatic actuation results from Maxwell's stress due to pressure created by attraction between opposite charges on the surface of a dielectric material. The pressure on the dielectric material with a dielectric constant ε due to an applied electric field E can be expressed as:

$$P = \varepsilon_0 \varepsilon E^2 \tag{3.11}$$

The strains resulting from the Maxwell's stress can be calculated from the storage modulus (E_s) of the nanocomposite samples ($S_{33}=P/E_s$). Table 3.3 lists the storage modulus as a function of the SWNT content. Our calculations indicate a maximum contribution from Maxwell strain of the order of -10^{-9} to -10^{-10} at the electric field magnitudes used in this study. Hence, electrostatic actuation can be ruled out as the mechanism driving the actuation response in the SWNT-CP2 nanocomposites due to the rigid nature of CP2 polyimide at room temperature

Table 3.3 Storage modulus of SWNT-CP2 nanocomposites.

SWNT loading (Vol%)	Storage Modulus E_s (MPa)
0	2960
0.02	3170
0.05	3700
0.1	3630
0.2	3460
0.5	3660
2	4700

3.5.2.4 Joule heating

Strains resulting from Joule or resistive heating show a quadratic dependence on electric field. To evaluate the Joule heating contributions to strains the temperatures of the SWNT – CP2 PI are mapped as a function of electric field using a thermocouple and an IR temperature gun. Under AC electric field the samples showed almost insignificant temperature increase of around 1 °C for 2 vol% SWNT samples at maximum AC actuation fields used. The samples were also heated in an oven through 120 °C to evaluate any bending response due to differences in the coefficient of thermal expansion between the thin polymer skin and the SWNT rich nanocomposite layer (Figure 3.14). In a different study[100], it has also been shown that the difference in the coefficient of thermal expansion between pure CP2 and SWNT+CP2 nanocomposites is negligible, possibly explaining the lack of bending response due to temperature changes. These observations indicate no contributions of Joule heating to the observed electromechanical strains due to the glassy nature of the CP2 (T_g = 200 °C).

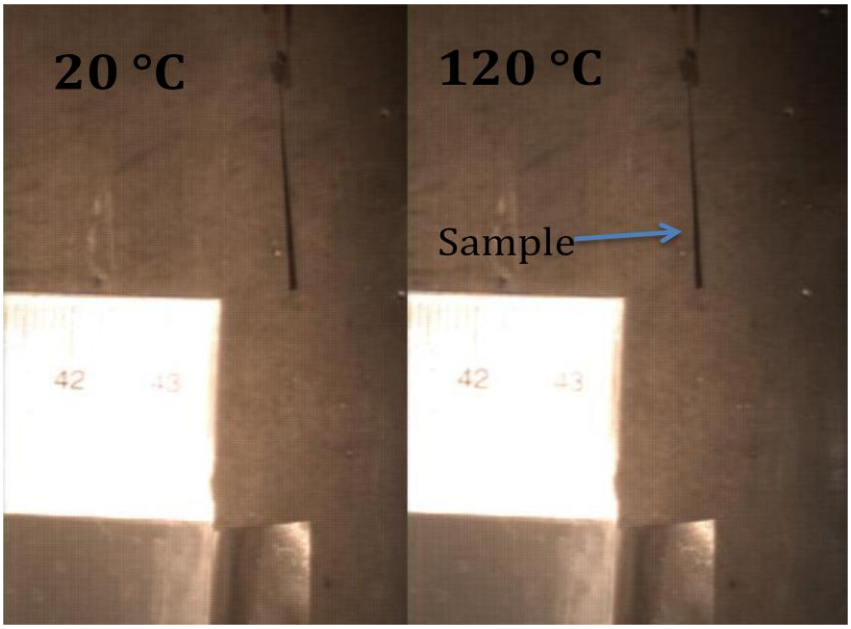

Figure 3.14 Effect of temperature on 2% SWNT – CP2 PI nanocomposite sample.

3.6 Discussion

In this section we have demonstrated the emergence of a quadratic electromechanical response in the SWNT – CP2 nanocomposites. The pristine polyimide did not demonstrate any measurable electromechanical response. The contributions to the electromechanical response from SWNTs, Maxwell's stress and Joule heating were determined to be minimal. The enhanced polarization in the nanocomposite samples detected by the dielectric relaxation spectroscopy and thermally stimulated current measurements strongly indicate an electrostrictive phenomenon.

The SWNTs used in this study are a mixture of metallic and semiconducting nanotubes, with a high effective dielectric constant[101, 102]. This contrast in the dielectric constant between the SWNTs and the polymer can lead to accumulation of charges at the inclusion-polymer interface causing interfacial polarization[103] schematically represented in Figure 3.15. Interfacial polarization increases with increase in the SWNT content and would explain the high dielectric constant values shown in Figure 3.9. However, contributions from dipoles inherent to the polymer matrix cannot be neglected. The electrical conduction at the percolation threshold results from an electron hopping phenomenon called quantum tunneling, rather than from physical contact between the SWNTs[104]. Therefore the presence of nano and micro- capacitors between the SWNTs is possible (Figure 3.16). This conjecture is also supported by the increase in the dielectric constant of the nanocomposite with SWNT content (Figure 3.9). In addition to augmenting the effective dielectric constant through a series of micro and nanocapacitors, the SWNTs could act as extension of electrodes within the polyimide. Our calculations show that in a percolated SWNT structure a field up to 2 factors higher than the applied field could exist locally between SWNTs. In these calculations, SWNTs are assumed to be at random angles in the conducting path through the thickness of the nanocomposite films. The distance between the SWNTs are assumed to exist in series and the distance between the nanotubes is computed for a particular concentration using a concentric cylinder representative volume element. In CP2, the C-CF_3 bonds (Figure 2.1) result in a dipole moment of around 2.95 debye[105, 106] but due to the rigid

dianhydride (6FDA) structure the movement of this dipole under an applied electric field is restricted. The higher local electric field between the SWNTs could cause the weak dipoles to rotate, further contributing to the enhanced induced polarization as represented in Figure 3.17.

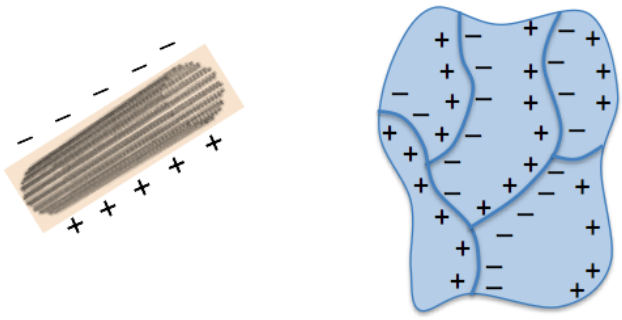

Figure 3.15 Interfacial polarization in SWNT-CP2 PI nanocomposites due to SWNTs.

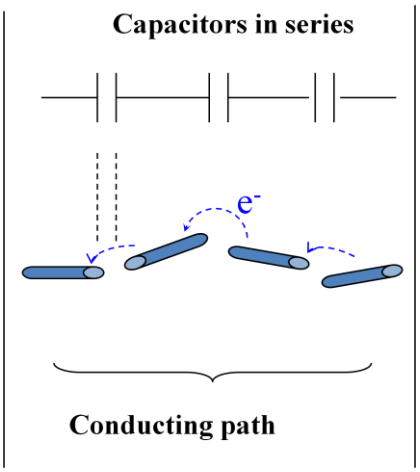

Figure 3.16 Possible scenario depicting polarization due to micro and nanocapacitors.

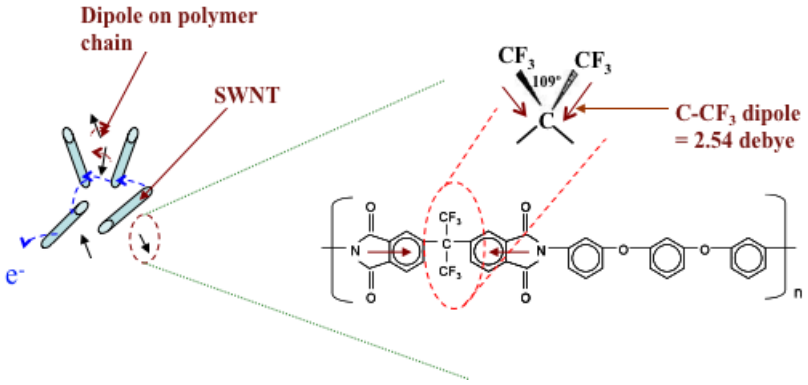

Figure 3.17 Polarization resulting from SWNTs acting as extensions of electrodes.

The focus of this section was on the demonstration of the creation and enhancement of an electromechanical coupling in SWNT-CP2 nanocomposites due to the presence of SWNTs. The neat polyimide does not show any actuation response under an applied electric field, whereas the SWNT-CP2 composites above the percolation threshold demonstrate an electrostrictive behavior. This response gets stronger with SWNT content as seen in Figure 3.7. TSC and dielectric relaxation studies confirmed the presence of dipole contributions, which increased with SWNT loading. Possible reasons for this observed behavior are: interfacial polarization, formation of micro or nanocapacitors, and local field enhancement due to SWNTs acting as electrodes. These effects are thought to result in the increase in polarization, resulting in the high electrostrictive behavior. These observations demonstrate that the presence of SWNTs not only enhances the electrical and dielectric properties but also creates an electromechanical response in a non-electroactive polymer.

4. ELECTROMECHANICAL RESPONSE OF SWNT-(β-CN)APB-ODPA NANOCOMPOSITES

In the previous section, the quadratic electromechanical response of SWNT-non polar polyimide CP2 nanocomposites was investigated. In the absence of major contributions from SWNT actuation, Maxwell's stress driven strains and Joule heating, the quadratic electromechanical response was attributed to polarization driven electrostriction. Dielectric relaxation spectroscopy and thermally stimulated current measurements showed enhanced polarization in the presence of SWNTs, confirming the polarization driven electrostrictive phenomenon.

In the absence of any external stress, thermal strains and piezoelectric response, the strains can be expressed as a function of polarization as (suppressing the indicial notation):

$$S=QP^2 \tag{4.1}$$

CP2 is a non-polar polyimide due to the rigid diamine structure that restricts any response from the small dipole on the polymer chain and does not show any non-covalent interaction with SWNTs[107]. From equation 4.1 it is clear that any improvements in the electrostrictive strain response of the SWNT based nanocomposites is dependent on enhanced polarization in the nanocomposites. The enhanced polarization in SWNT – polymer nanocomposites can result from two factors:

a) Polymer dipoles and
b) SWNT – polymer interaction

In this section the quadratic electromechanical response of SWNT nanocomposites based on the polar (β-CN) APB ODPA polyimide is reported. SWNT-(β-CN) APB ODPA nanocomposites are of interest because (β-CN) APB ODPA has a higher dipole than CP2 as shown in Figure 4.1 and also demonstrates an electron donor-acceptor relationship with SWNTs. Figure 4.2 schematically shows the SWNT – CN interaction which can be detected due to change in the SWNT structure using Raman

spectroscopy. The upshift in the Raman G band frequency of SWNTs is attributed to stiffening of carbon-carbon bonds in the SWNTs due to loss of an electron [52].

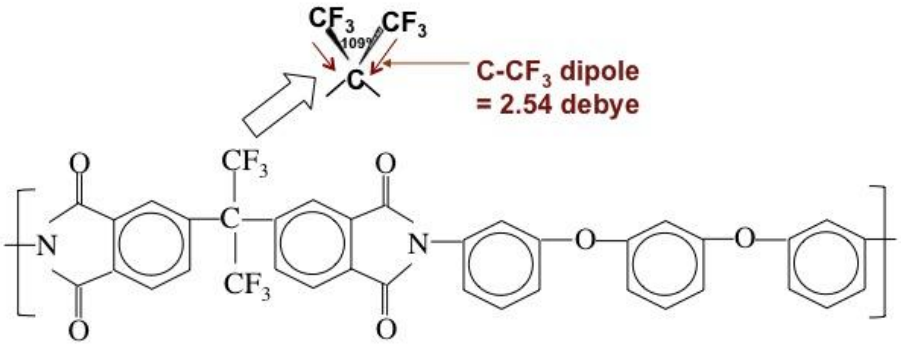

(a)

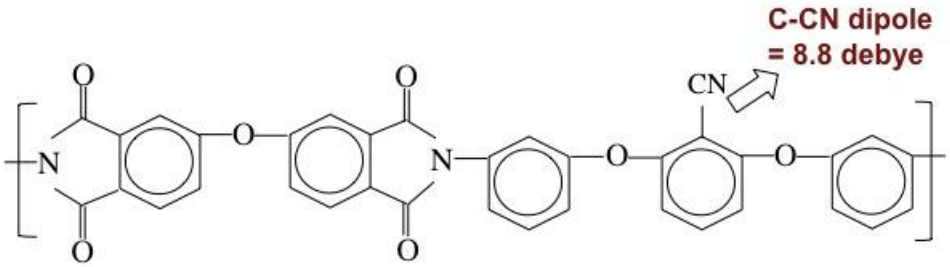

(b)

Figure 4.1 Polymer dipoles of (a) CP2 and (b) (β-CN) APB ODPA.

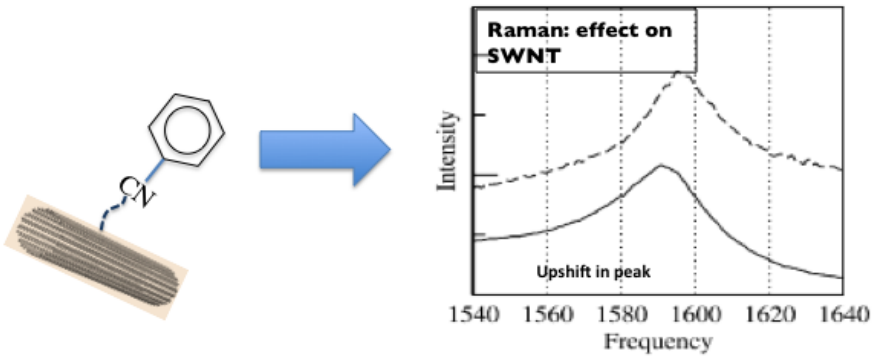

Figure 4.2 Secondary non-covalent interaction between SWNTs and C-CN dipole on (β-CN) APB ODPA (adapted from [52]).

Figure 4.3 (a) and (b) show the fracture surface of 0.5 vol% SWNT - (β-CN) APB ODPA nanocomposite samples. It can be observed from the images that SWNTs are well dispersed and show good adhesion with the polymer. This is in contrast with the observations of the SWNT-CP2 nanocomposites (Figure 3.1). Observations from Figure 4.3 also support the findings from [52] of good interaction between the SWNTs and (β-CN) APB ODPA, as indicated by Raman and FTIR studies.

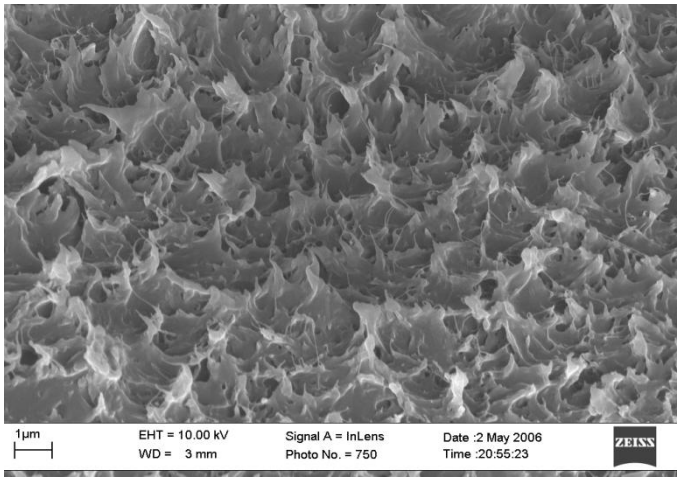

(a)

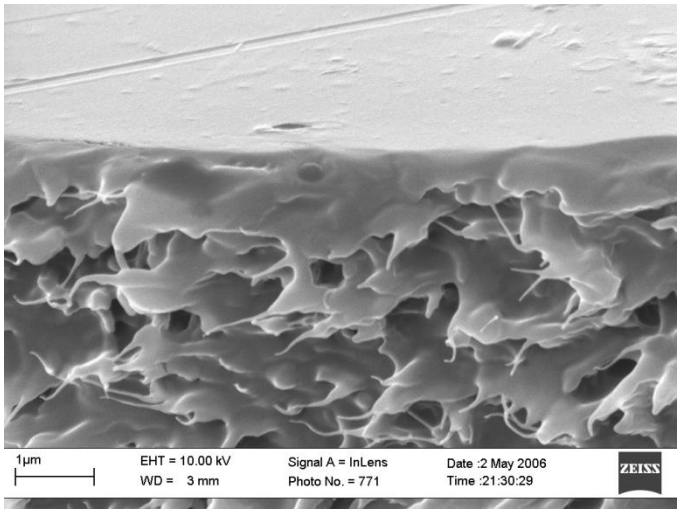

(b)

Figure 4.3 SEM images of 0.5%SWNT-(β-CN) APB-ODPA, (a) Image shows a good dispersion of nanotubes, (b) SWNTs anchored in the polymer matrix.

4.1 Thickness actuation

Figure 4.4 (a) shows the transverse S_{33} strains measured using the MTI 2100 fiber optic sensor as a function of electric field and SWNT content for the SWNT-(β-CN) APB-ODPA nanocomposites at 1Hz AC signal (Sine wave). The strains increase non-linearly with increase in electric field similar to the SWNT-CP2 case. The nanocomposites also demonstrate an increased strain response with increasing SWNT content. Figure 4.4 (b) shows a linear trend in the strains plotted as a function of squared electric field. The quadratic dependence of the strains is also confirmed physically by increase in the sample thickness in successive half cycles of the applied AC field.

Figure 4.5 shows a comparison between SWNT-CP2 and SWNT-(β-CN) APB-ODPA for 0.1 vol% SWNT and 1 vol% SWNT samples. It is evident from the figure the SWNT-(β-CN) APB-ODPA samples show a higher strain response as compared to the SWNT-CP2 samples.

4.2 Bending Actuation

Figure 4.6 shows the longitudinal S_{11} strains calculated from the bending experiment as a function of DC electric field, polarity of electric field and SWNT content for SWNT-(β-CN) APB-ODPA. The strain increases with electric field and SWNT content. The quadratic dependence of strains on electric field, observed in the thickness actuation experiments, is confirmed by the behavior of the longitudinal strains shown in Figure 4.6. The samples bend in the same direction on reversing the polarity of the applied DC field as reflected by Figure 4.6 (a). Figure 4.6 (b) shows the linear dependence of strains on the quadratic electric field.

In Figure 4.7, the longitudinal strains in both SWNT-CP2 and SWNT-(β-CN) APB-ODPA systems are compared for 0.1 vol% SWNT and 2 vol% SWNT samples. As in the thickness actuation case, the SWNT-(β-CN) APB-ODPA nanocomposites show a higher electromechanical strain response than the SWNT-CP2 nanocomposite samples.

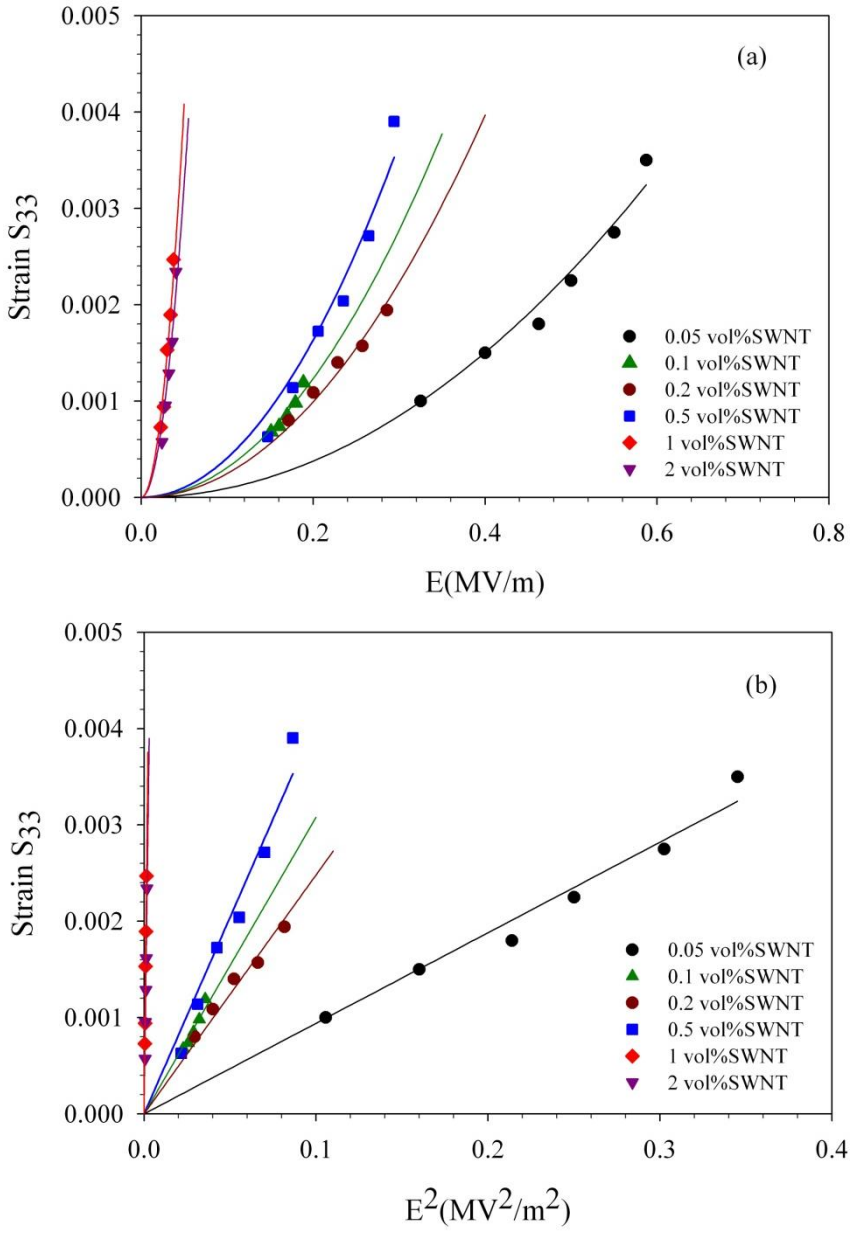

Figure 4.4 (a) Transverse strains as a function of AC electric field (1 Hz) and SWNT content. (b) Transverse strains proportional to squared electric field. Solid lines are quadratic fit for (a), and linear for (b).

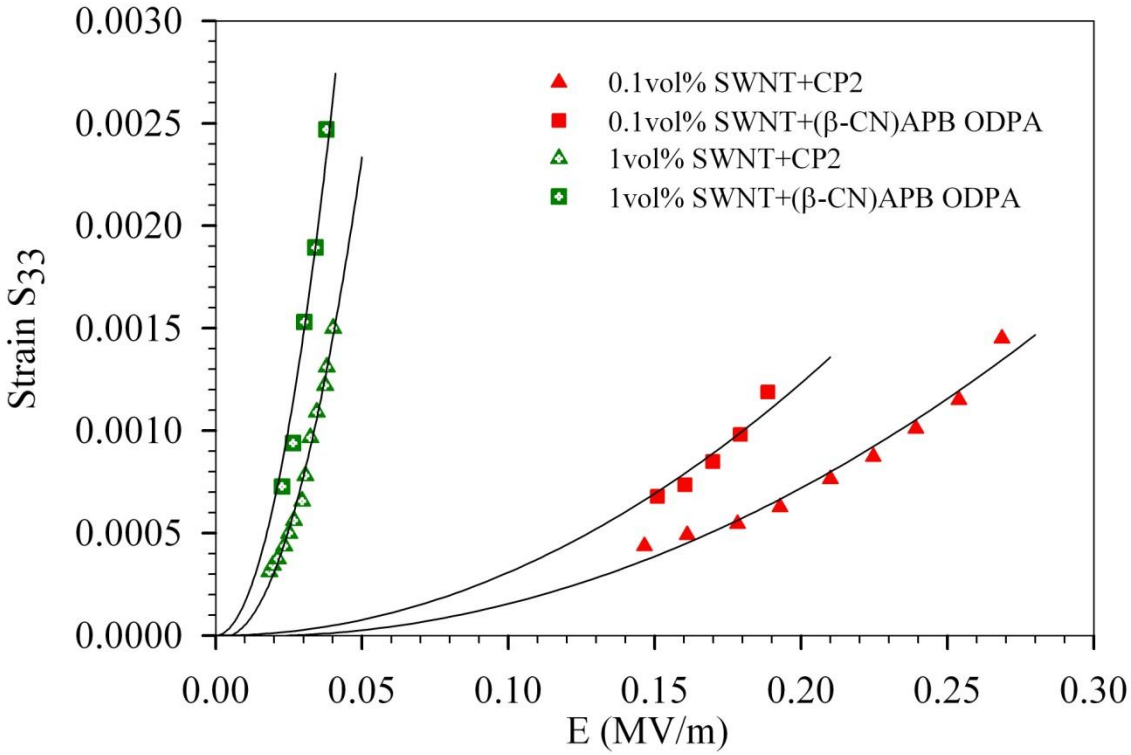

Figure 4.5 Comparison of transverse strains between SWNT-CP2 and SWNT-(β-CN) APB-ODPA nanocomposites.

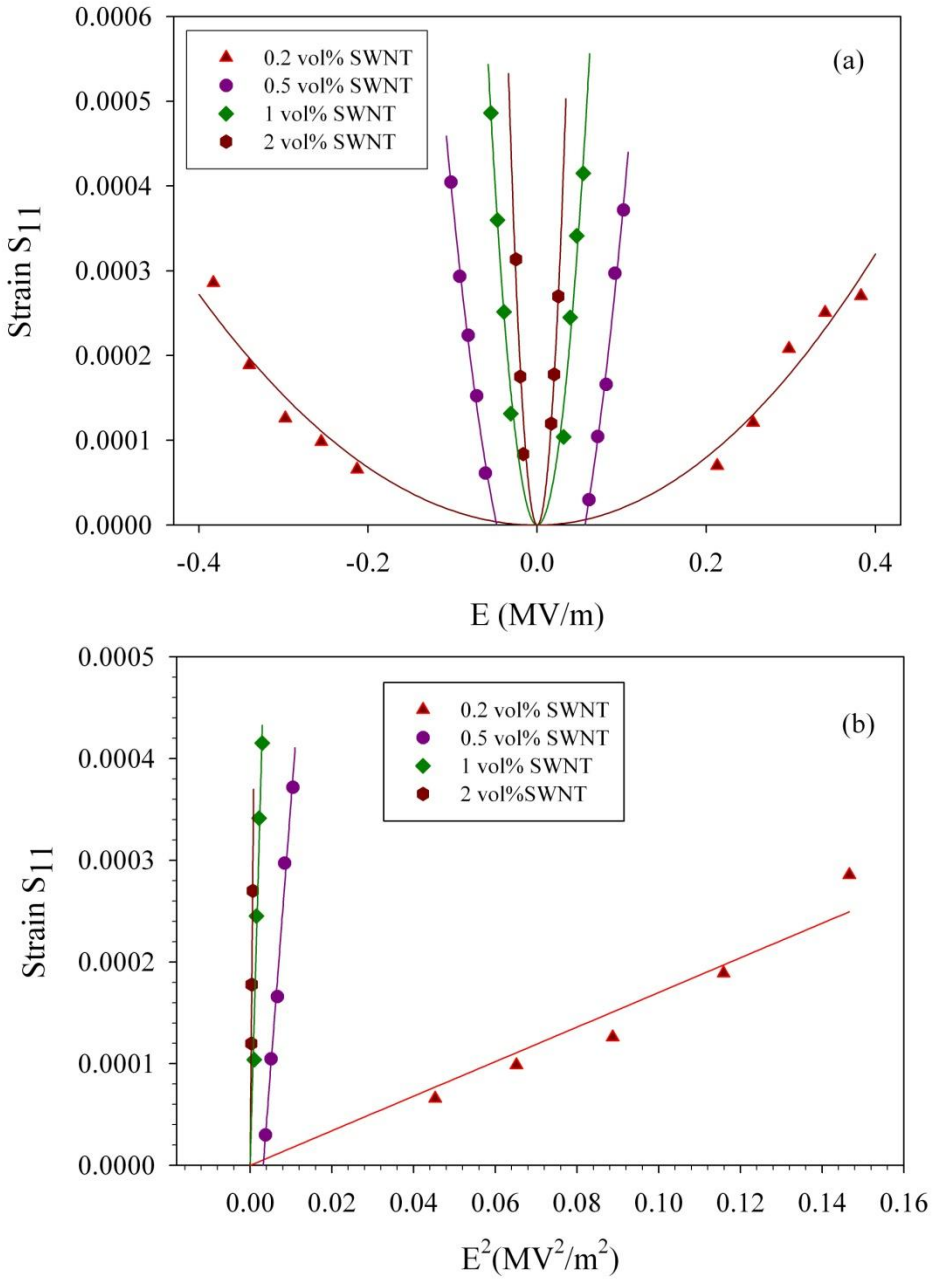

Figure 4.6 (a) Longitudinal strains as a function of DC electric field and SWNT content. (b) Longitudinal strains proportional to squared electric field. Solid lines are quadratic fit for (a), and linear for (b).

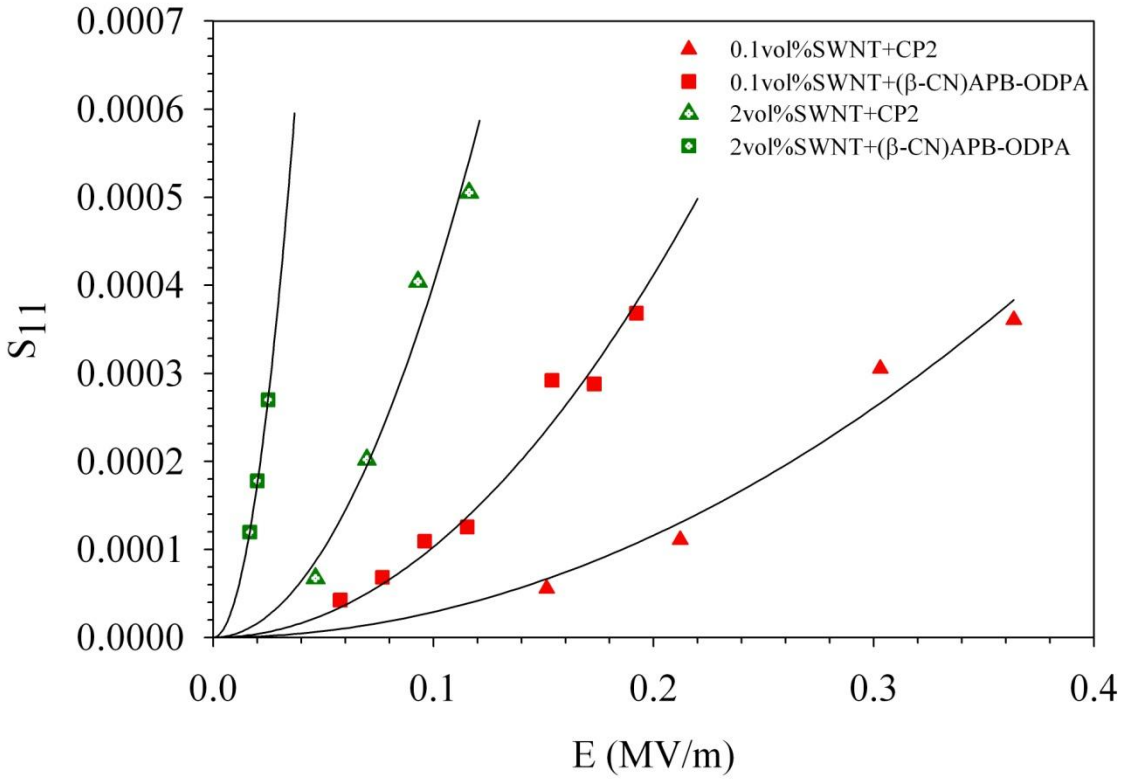

Figure 4.7 Comparison of longitudinal strains between SWNT-CP2 and SWNT-(β-CN) APB-ODPA nanocomposites.

4.3 Strain rate

The rate at which the longitudinal strain for 0.5 vol% SWNT sample approaches its maximum is plotted in Figure 4.8. The strain rate increases with the applied electric field. The comparison of strain rates for different electric fields for 0.5 vol% SWNT samples for CP2 and (β-CN) APB-ODPA based nanocomposites are shown in Figure 4.9. The 0.5 vol% SWNT - (β-CN) APB-ODPA samples show higher strain rates than the 0.5 vol% SWNT – CP2 samples. In the last section we had established that the strain rate increased with the SWNT content. These results show that the strain rates are also dependent on the polymer matrix dipole and the SWNT – polymer interaction.

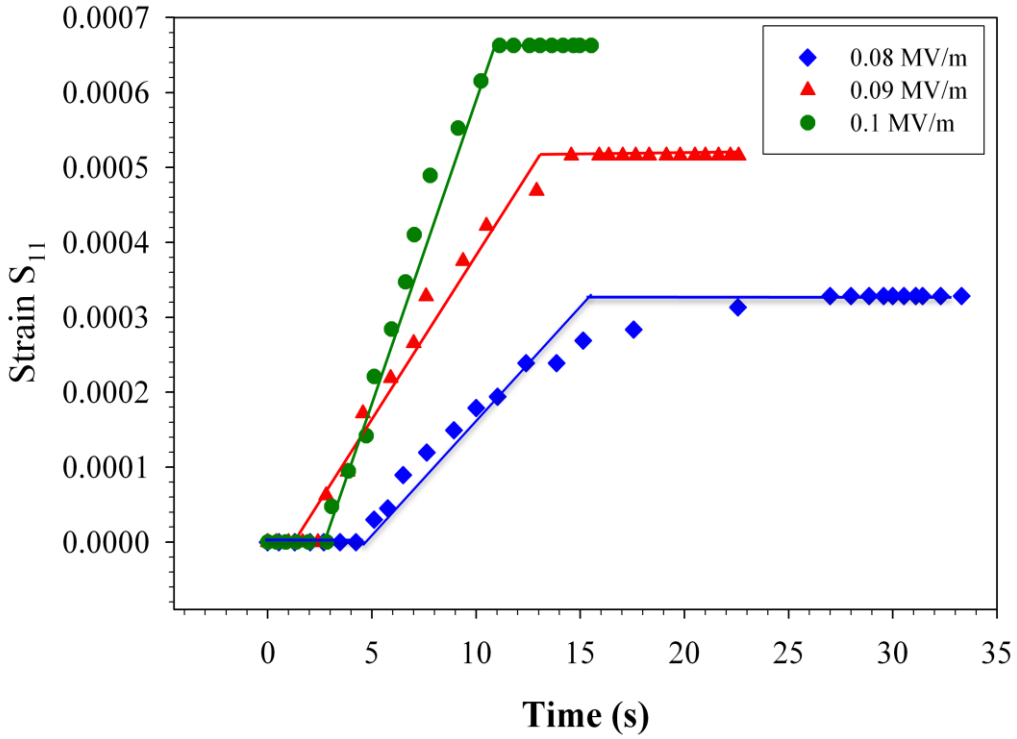

Figure 4.8 S_{11} strain rates compared at different voltages for 0.5 vol% SWNT- (β-CN) APB-ODPA.

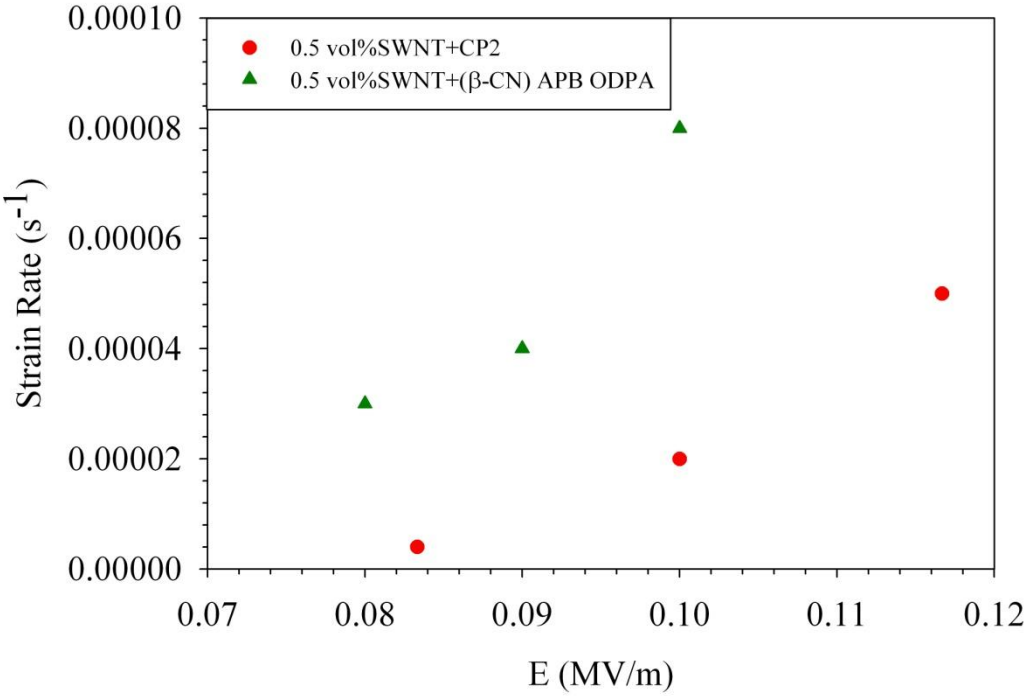

Figure 4.9 S_{11} strain rates comparison between 0.5 vol% SWNT- CP2 and 0.5 vol% SWNT - (β-CN) APB-ODPA.

4.4 Electrostriction

Same observations are made about minimal contributions from SWNT actuation, Joule heating and Maxwell's stress as causes for actuation for SWNT-(β-CN) APB-ODPA nanocomposites as was discussed in detail for the SWNT – CP2 samples in the previous section. In this section we compare the coefficients of electrostriction for SWNT-(β-CN) APB-ODPA nanocomposites with those of SWNT – CP2 system. Furthermore we compare the effect of the higher polymer dipole and SWNT – (β-CN) APB-ODPA interaction on the polarization observed in the nanocomposite samples using dielectric relaxation spectroscopy and thermally stimulated current measurements.

4.4.1 Coefficients of electrostriction

Figures 4.10 and 4.11 show the effect of SWNT content on the M_{3333} (1 Hz AC) and M_{13} (DC) electrostrictive coefficients for SWNT - (β-CN) APB-ODPA

nanocomposites. Both electrostrictive coefficients show an increase with SWNT content. The figures also show the comparison between the SWNT - CP2 and SWNT - (β-CN) APB-ODPA coefficients. As reflected in the thickness and longitudinal strain response discussed earlier, the SWNT - (β-CN) APB-ODPA electrostrictive coefficients are consistently higher than those of SWNT - CP2 nanocomposites. The coefficients are also compared with those from known electrostrictive polymers like electrostrictive graft elastomer[78] and polyurethane[94]. The nanocomposites show electrostrictive coefficients almost 5-6 orders higher than those of the electrostrictive polymers.

Figure 4.12 shows the effect of frequency on the M_{1133} coefficient for SWNT - (β-CN) APB-ODPA nanocomposites. An initial sharp decrease is seen in the coefficient as the frequency increases followed by a gradual decrease in the value. This result indicates dipolar contributions to the actuation response shows a steep decrease initially with increasing frequency. This can possibly be attributed to decreased contributions of interfacial polarization, which is dominant at low frequencies.

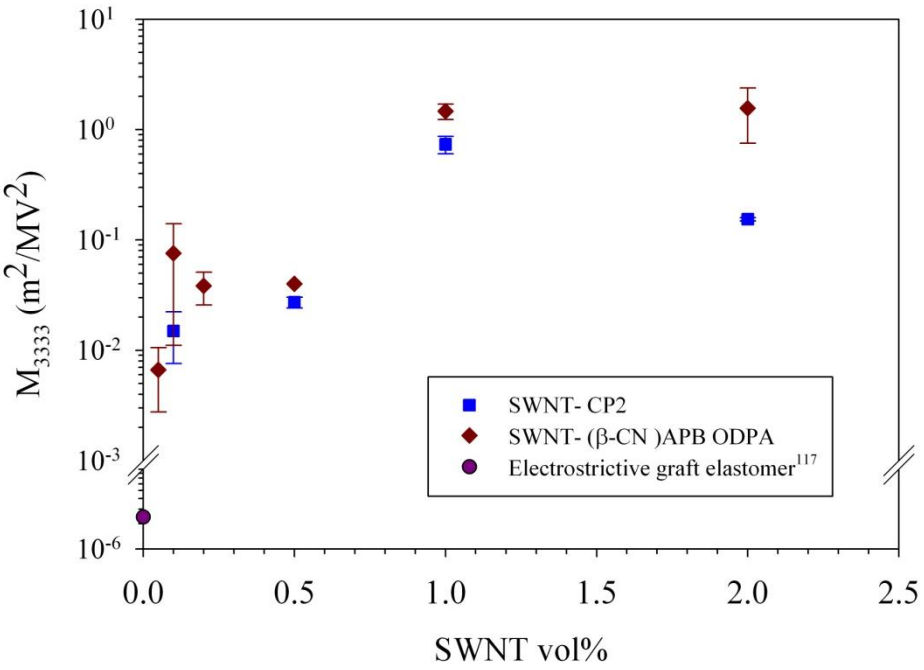

Figure 4.10 Comparison of M_{3333} quadratic electromechanical coefficients between SWNT - CP2 and SWNT - (β-CN) APB-ODPA nanocomposites (1 Hz AC).

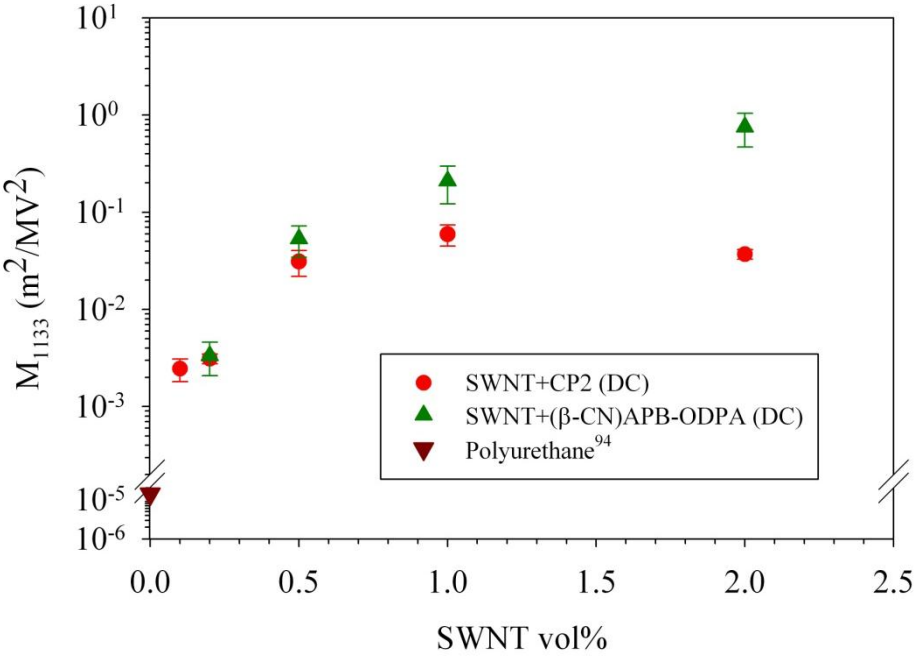

Figure 4.11 Comparison of M_{1133} quadratic electromechanical coefficients between SWNT - CP2 and SWNT - (β-CN) APB-ODPA nanocomposites (DC).

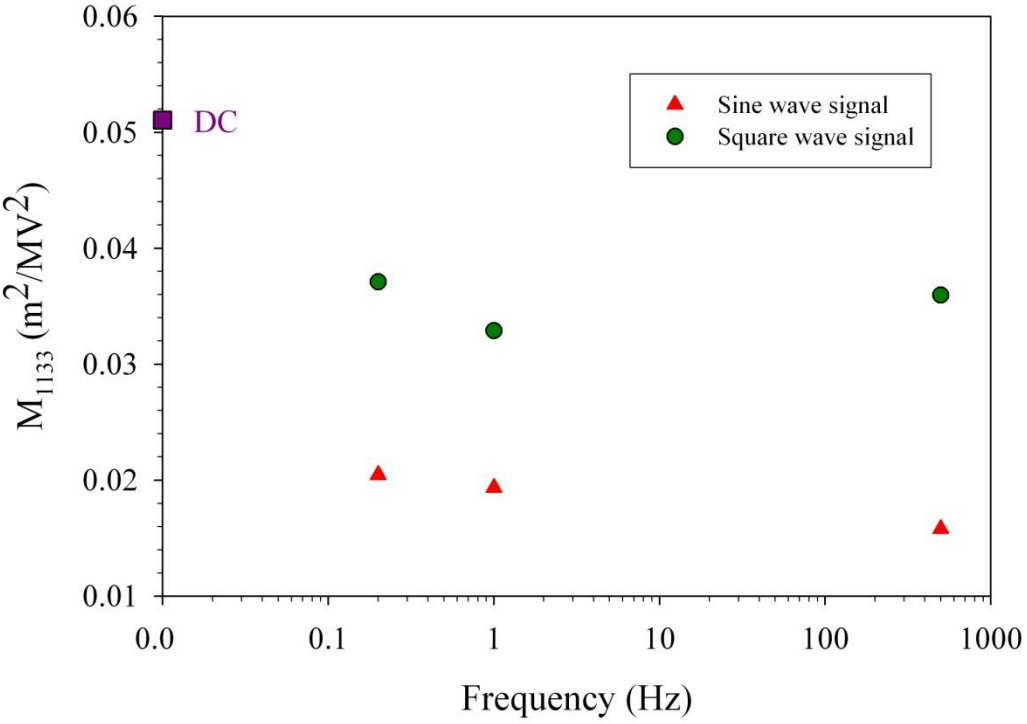

Figure 4.12 M_{1133} as a function of frequency.

The actuation results discussed so far for the SWNT - (β-CN) APB-ODPA nanocomposites and their comparison with the SWNT – CP2 samples indicate a strong effect of polymer dipole and SWNT – polymer interaction on the actuation response. The strain response for the polar (β-CN) APB-ODPA based nanocomposites are consistently higher than that of the CP2 based nanocomposites.

4.4.2 Comparison of SWNT-polyimide actuators with known electrostrictive polymers

Table 4.1 compares the critical parameters like maximum strain, electric field, coefficient of electrostriction and gravimetric work capacity of the SWNT-CP2 and SWNT-(β-CN) APB-ODPA nanocomposites actuators with known electrostrictors like P(VDF-TrFE) and polyurethane. The maximum strains achieved by the SWNT-polyimide nanocomposite actuators is lower than P(VDF-TrFE) but the threshold electric fields required to achieve these strains is a fraction of that required for these polymers. Also, as shown earlier, the coefficient of electrostriction can be 7 to 8 orders of magnitude greater for the 2 vol% SWNT-polyimide nanocomposites than P(VDF-TrFE) and polyurethane[64, 94]. The gravimetric work capacity for the SWNT-polyimide nanocomposite actuators can be calculated from storage modulus E_s (Table 3.3 and [108]) and density ρ (estimated by rule of mixtures) by:

$$W_{gravimetric} = \frac{E_s \cdot (\max\ strain)^2}{2 \cdot \rho} \tag{4.2}$$

The gravimetric work capacity of the SWNT-polyimide nanocomposite actuators is higher than that of P(VDF-TrFE) but lower than that of polyurethane. In general, the gravimetric work capacity is comparable for the nanocomposite actuators and known electrostrictive polymers. The big advantages of these actuators are the high coefficient of electrostriction and very low actuation electric fields coupled with comparable gravimetric work capacity with state of the art electrostrictive polymers.

Table 4.1 Comparison of SWNT-CP2 and SWNT-(β-CN) APB-ODPA with known electroactive polymers.

Sample	Maximum thickness strain (%)	Applied electric field (MV/m)	M_{33} coefficient (m^2/MV^2)	$W_{gravimetric}$ (J/kg)
CP2+2 vol% SWNT	0.22	0.12	0.15	9.5
(β-CN) APB-ODPA+2 vol% SWNT	0.23	0.04	1.5	8
P(VDF-TrFE) [64]	4	150	2.6×10^{-8}	4
Polyurethane [94]	1.6×10^{-4}	4	9.4×10^{-6}	13[64]

4.4.3 Polarization

The SWNT-(β-CN)APB-ODPA nanocomposite samples show a higher electrostrictive response than the SWNT-CP2 samples. Since electrostriction is a polarization dependent electromechanical response, it is important to study the effect of the polymer dipole and SWNT-polymer interaction on the polarization of the nanocomposites. In this section, we evaluate this effect on polarization of the nanocomposites using dielectric relaxation spectroscopy and thermally stimulated current measurements. The SWNT-(β-CN)APB-ODPA results are compared with those of the SWNT – CP2 nanocomposites.

The dielectric constant of SWNT - (β-CN)APB-ODPA nanocomposite samples is compared with that of SWNT – CP2 samples in Figure 4.13. . The percolation threshold of SWNT - (β-CN)APB-ODPA samples is a low 0.06 vol% that is comparable to the 0.04 vol% observed in the CP2 samples[79]. The dielectric constant increases with SWNT content for both nanocomposites above the percolation threshold and are comparable in magnitude.

Figure 4.14 (a) shows the depolarization current for pure (β-CN) APB-ODPA

and 0.5 vol% SWNT obtained from TSC experiments. Pure (β-CN) APB-ODPA samples shows a current peak of 0.002 mA/m^2, which is about 50 times smaller than that demonstrated by the 0.05 vol% SWNT samples. Figure 4.14 (b) shows the comparison between the polarization measured from the TSC experiments between 0.05 vol% SWNT – CP2 and 0.05 vol% SWNT - (β-CN) APB-ODPA samples at different electric fields. The SWNT-CP2 samples show higher polarization values as compared to the SWNT - (β-CN) APB-ODPA samples.

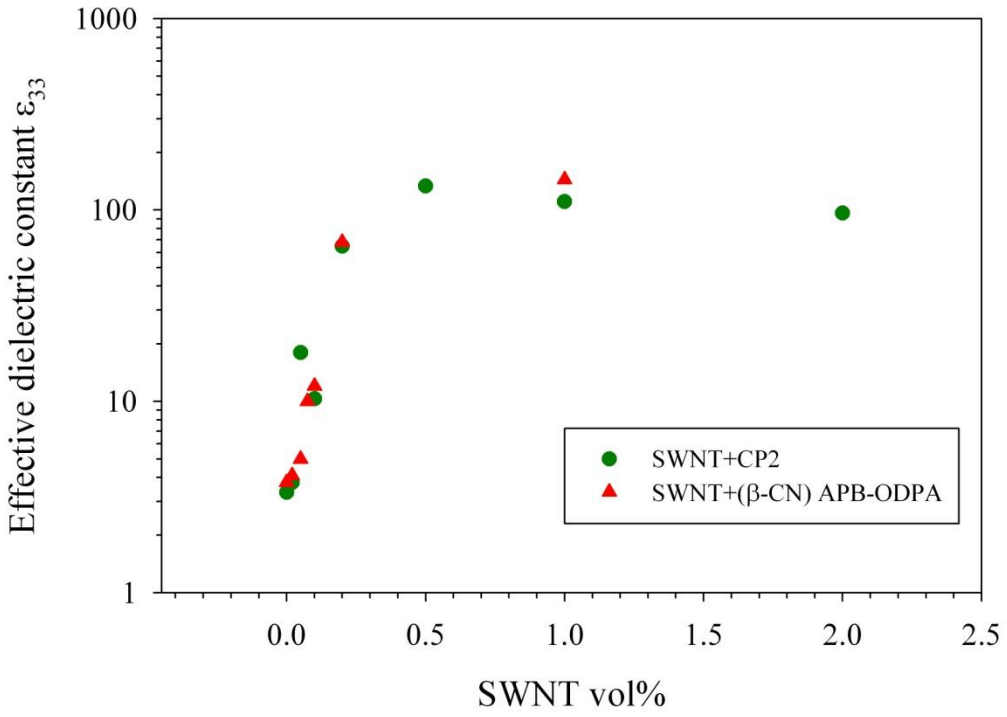

Figure 4.13 Dielectric constant vs SWNT content comparison between SWNT – CP2 and SWNT-(β-CN) APB-ODPA nanocomposites.

Dielectric relaxation spectroscopy is employed to further investigate the induced polarization in SWNT - (β-CN) APB-ODPA samples. Figure 4.15 shows the dielectric constant as a function of temperature for these nanocomposite samples. The dielectric relaxation strength values (Δε) measured from the plot are listed in Table 4.2 and compared with those measured from the SWNT-CP2 samples (Table 3.2). The Δε value

increases with SWNT content and is higher for the SWNT - (β-CN) APB-ODPA samples as compared to the SWNT-CP2 system. Figure 4.16 shows the projected remnant polarization for SWNT-(β-CN) APB-ODPA nanocomposites using the dielectric relaxation strength equation 3.10 for the actuation electric fields used in the study. An increase in the remnant polarization is seen with increase in electric field and SWNT content.

The dielectric constant values shown in Figure 4.13 are measured at low frequencies (<500 Hz) and extrapolated to DC case. Interfacial polarization, which is typically dominant at low frequencies, can result in the high dielectric constant values due to increased time available for movement of charge carriers. The comparable dielectric constant values between the (β-CN) APB-ODPA and CP2 nanocomposites but higher induced polarization detected by TSC and dielectric relaxation spectroscopy indicates that interfacial polarization may not be a critical factor in the difference between the polarization seen by the two nanocomposite systems. The higher induced polarization and electrostrictive response in SWNT-(β-CN) APB-ODP nanocomposites can then be attributed more to the higher (β-CN) APB-ODPA dipole and SWNT - (β-CN) APB-ODPA interaction than due to trapped charge carriers.

In this section we demonstrated the effect of polymer matrix dipole and SWNT-polymer interaction on the electrostrictive response of SWNT based nanocomposites. A higher induced polarization and SWNT-polymer interaction was shown in SWNT-(β-CN) APB-ODPA nanocomposites as compared to SWNT-CP2 nanocomposites. In the next section, the electrostrictive response of SWNT-polyvinylidene fluoride (PVDF) nanocomposites will be discussed. PVDF can demonstrate both a high polarization and an affinity with SWNTs as well; as such, it holds potential on further improving the electrostrictive response of SWNT based nanocomposites.

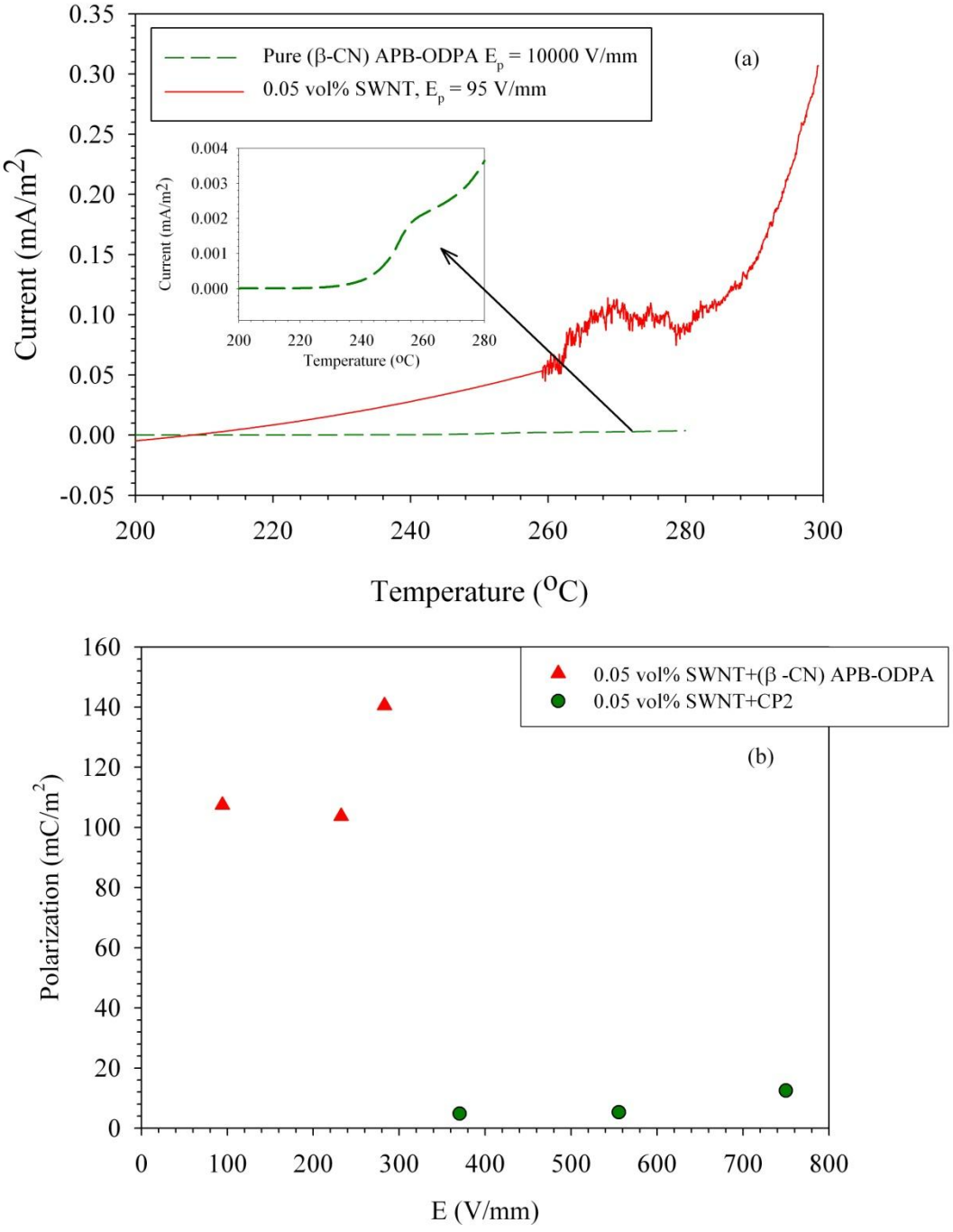

Figure 4.14 (a) Depolarization current as a function of temperature for Pure (β-CN) APB-ODPA and 0.05 vol% SWNT samples. (b) Comparison of polarization induced in the 0.05 vol% SWNT – CP2 and 0.05 vol%SWNT-(β-CN) APB-ODPA nanocomposites by TSC.

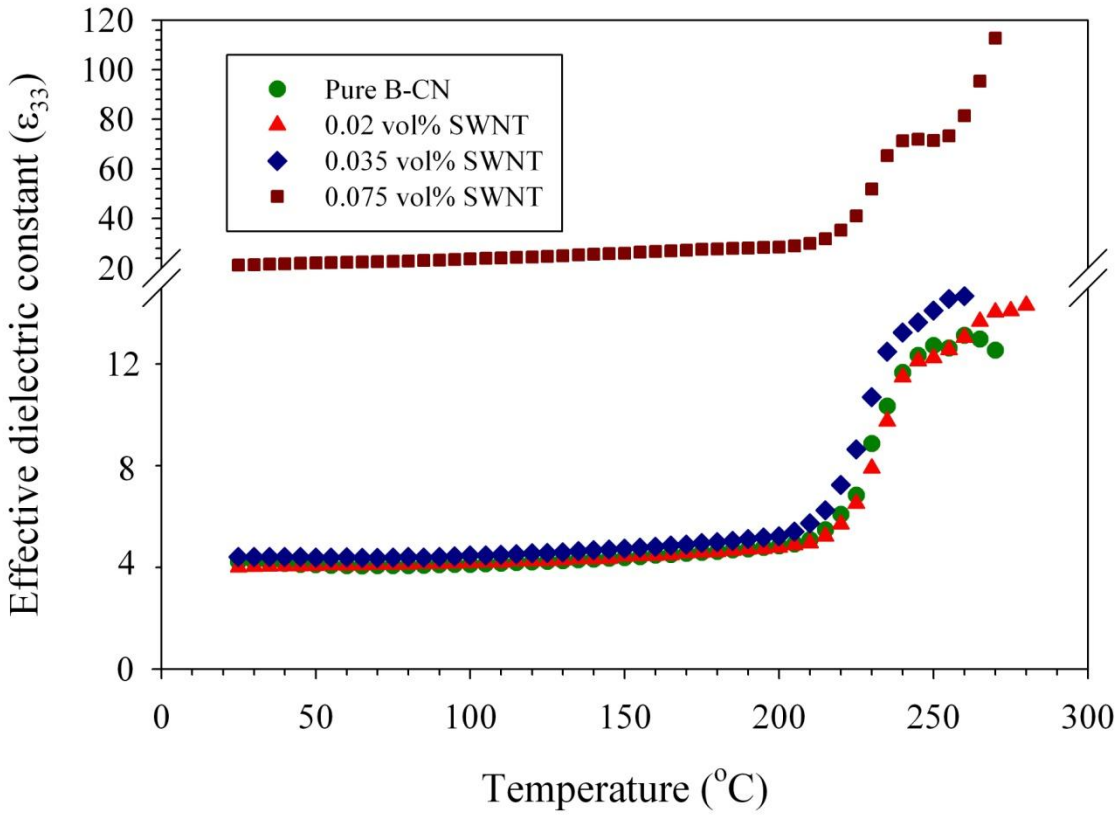

Figure 4.15 Dielectric constant as a function of temperature at 20 Hz showing dipolar relaxation at different SWNT content for SWNT - (β-CN) APB-ODPA nanocomposites.

Table 4.2 $\Delta\varepsilon$ comparison between SWNT – CP2 and SWNT - (β-CN) APB-ODPA as a function of SWNT loading.

SWNT loading (Vol%)	$\Delta\varepsilon_{@21.5Hz}$ (CP2)	$\Delta\varepsilon_{@20Hz}$ ((β-CN) APB-ODPA)
0	0.69	8.6
0.02	0.72	9.69
0.035	-	10.59
0.05	21	-
0.075	-	48
0.1	24	-

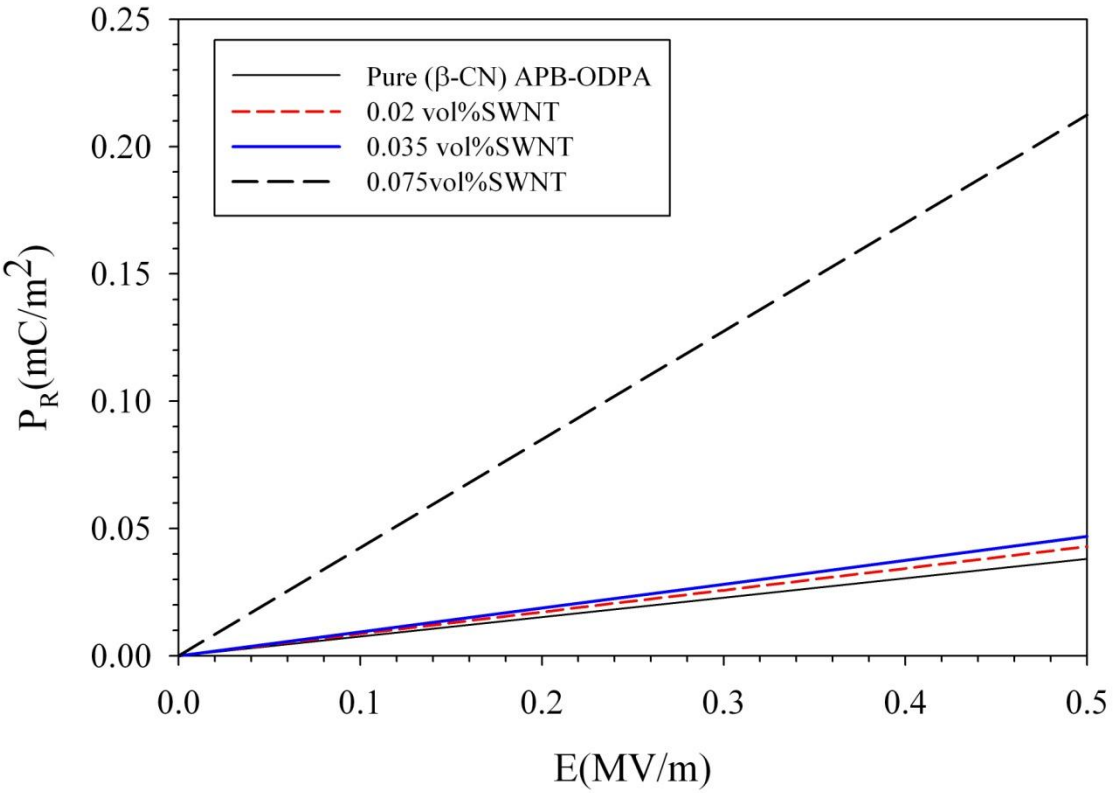

Figure 4.16 Remnant polarization predicted for SWNT - (β-CN) APB-ODPA nanocomposites for the actuation electric fields used.

5. ELECTROMECHANICAL RESPONSE OF SWNT-PVDF NANOCOMPOSITES

Sections 3 and 4 described the electromechanical response of SWNT-based polyimide nanocomposites. In Section 3, the polarization-dependent electrostrictive response of SWNT-non polar CP2 polyimide nanocomposites was discussed. In Section 4 the electrostrictive response of SWNT-polar (β-CN)APB-ODPA polyimide nanocomposites was discussed in detail, and a higher electrostrictive response was found as compared to the SWNT-CP2 nanocomposite samples. The higher electrostrictive response of the SWNT - (β-CN) APB – ODPA nanocomposites was attributed to higher induced polarization resulting from a strong noncovalent interaction between the CN dipole and the SWNTs, and a higher orientation polarization in the (β-CN) APB – ODPA matrix due to the C-CN dipole.

In this section we evaluate the electrostrictive response of SWNT-polyvinylidene difluoride (PVDF) nanocomposites. (β-CN)APB-ODPA has a higher dipole moment (μ) (8.8D)[109, 110] than CP2 which is estimated at 2.93D[111-113]. PVDF on the other hand has a dipole moment of 2.1D but has higher number of dipoles per unit volume (N) leading to an ultimate polarization between 50-100 mC/m^2 (μ*N)[114], much higher than the 40 mC/m^2 possible for (β-CN)APB-ODPA. Furthermore, recent research has targeted crystalline phase transformation in PVDF using CNTs. Yu et al[69] have reported formation of the β phase in the presence of multiwalled carbon nanotubes (MWNTs) caused by the absorption of PVDF trans-trans conformation, formed due to sonication, onto the MWNTs. Manna et al[4] have also demonstrated formation of the β phase due to interaction between functionalized MWNTs and PVDF. Similar observations of MWNT induced β phase formation in PVDF have been reported by other researchers[3, 5]. These results are significant because the β phase of PVDF has the highest polarization and therefore appear the most promising.

Figure 5.1 shows the Raman spectrographs of pure PVDF, SWNTs and PVDF+1.33 vol% SWNT. An upshift of 5 cm^{-1} is observed in the tangential G band frequency of SWNTs in the nanocomposite samples. This upshift is attributed to the

structural changes in SWNTs resulting from an electron donor acceptor relationship between the SWNTs and the electronegative fluorine group[115, 116].

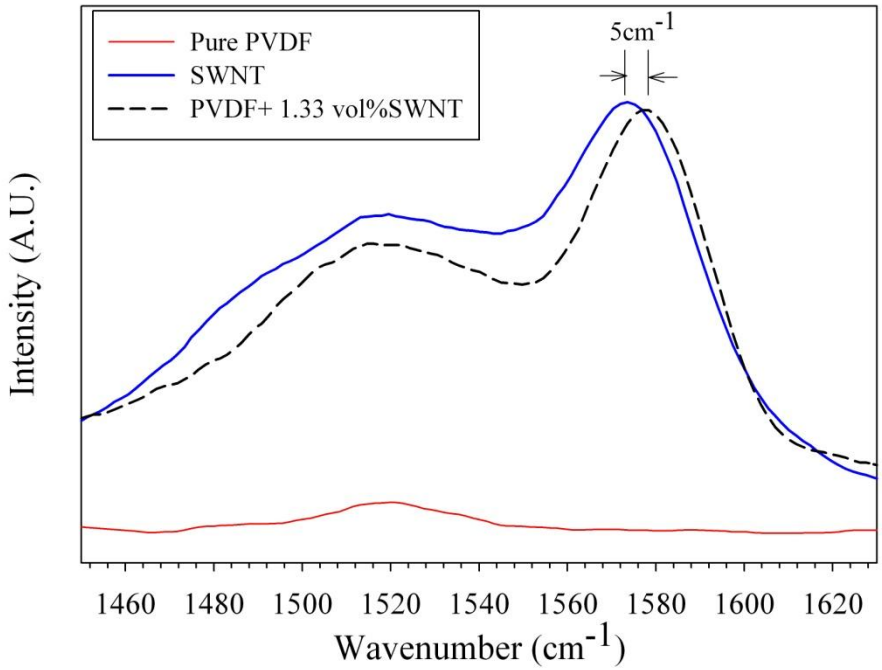

Figure 5.1 Upshift in tangential G band frequency of SWNTs in the PVDF nanocomposites.

Choosing PVDF as the matrix for SWNT based nanocomposites satisfies both the criteria listed earlier to achieve enhanced electrostrictive response, namely high polarization of the matrix and strong dipole-SWNT affinity.

5.1 Electrical conductivity

A series of SWNT-PVDF nanocomposites were processed as described in Section 2.1.2. Characterization of electrical conductivity and percolation were done to qualify and quantify dispersion of SWNTs in the PVDF matrix. Figure 5.2 shows the electric conductivity as a function of frequency at different SWNT content. Generally, the conductivity increases with SWNT content up to 1.33 vol%. The behavior of the composites changes from insulating (increase in conductivity with frequency) to

conducting (constant conductivity with frequency) between 0.26 – 0.4 vol% SWNT which indicates percolation behavior. This is further confirmed from the inset of Figure 5.2 which shows a six order of magnitude increase in conductivity for DC case, as the SWNT content increases from 0.26 vol% to 0.4 vol%.

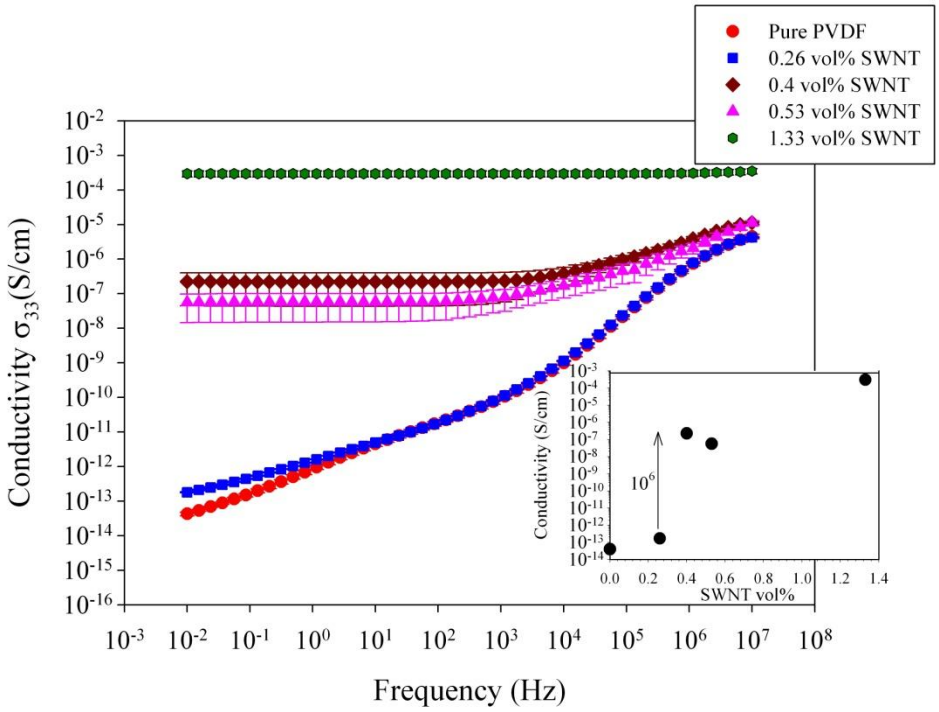

Figure 5.2 Electrical conductivity vs frequency at different SWNT loading. Inset shows an increase of 6 orders in conductivity at percolation.

5.2 Thickness actuation

Figure 5.3 (a) depicts the transverse S_{33} strains for SWNT-PVDF nanocomposites plotted as a function of AC electric field (1 Hz sinusoidal) for different SWNT content samples. A nonlinear dependence of S_{33} is observed as a function of electric field. The S_{33} strains are proportional to the quadratic electric field as seen in Figure 5.3 (b). The quadratic response of the nanocomposites is further confirmed by thickness increase to applied AC field: the thickness always increases in successive half cycles. Pure PVDF that was unpoled and unstretched did not demonstrate any strain response to the applied field. In general increasing the SWNT vol% increases the

electromechanical strain response: the 1.33 vol% SWNT samples show a significantly higher strain response than the 0.4 vol% and 0.53 vol% SWNT samples.

5.3 Bending actuation

Figure 5.4 (a) shows the S_{11} strains for 0.4 vol% SWNT, 0.53 vol% SWNT and 1.33 vol% SWNT samples as a function of DC electric field. It is noted that pure PVDF did not show any bending response. The strains increase with the electric field and are higher for 1.33 vol% SWNT samples as compared to the 0.4 vol% SWNT and 0.53 vol% SWNT samples. Figure 5.4 (b) shows the strains plotted as a function of the squared electric field. The linear dependence confirms the quadratic electrostrictive behavior of the samples. It is also noted that the sample bends in the same direction on reversing the applied electric field. The bending is a result of a resin-rich constraining layer formed in the sample during processing as discussed in Section 3.

Figure 5.5 (a) depicts the S_{11} strains for the nanocomposites as a function of the AC electric field (1 Hz sinusoidal). The strains increase with and have a quadratic dependence on the electric field as can be seen from Figure 5.5 (b). On each half cycle of the AC signal the samples bend in the same direction, confirming the quadratic response. The strains are highest for 1.33 vol% SWNT samples compared to both 0.4 vol% SWNT and 0.53 vol% SWNT. As noted earlier in the thickness actuation case, the 0.4 vol% SWNT samples show a marginally higher response than 0.53 vol% SWNT samples.

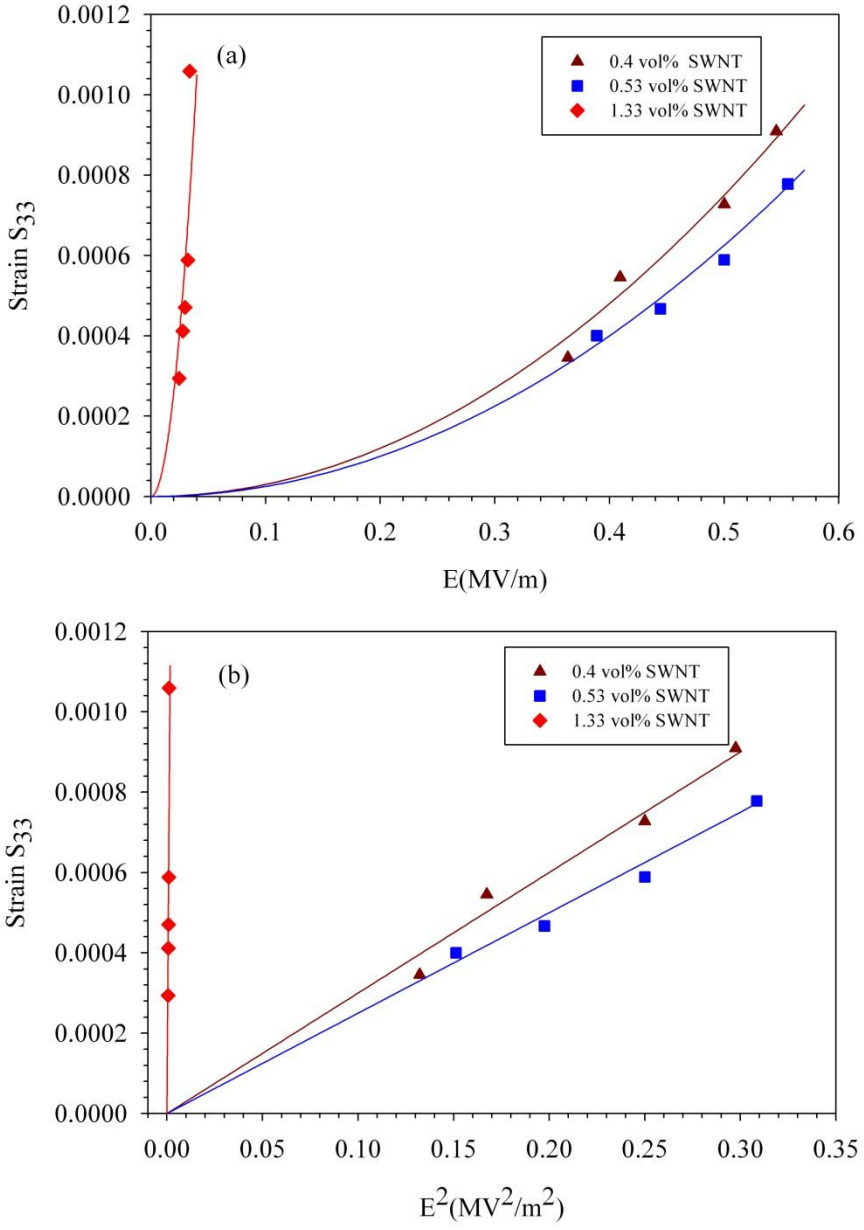

Figure 5.3 (a) S_{33} vs electric field, (b) S_{33} vs squared electric field, for 1 Hz sinusoidal signal.

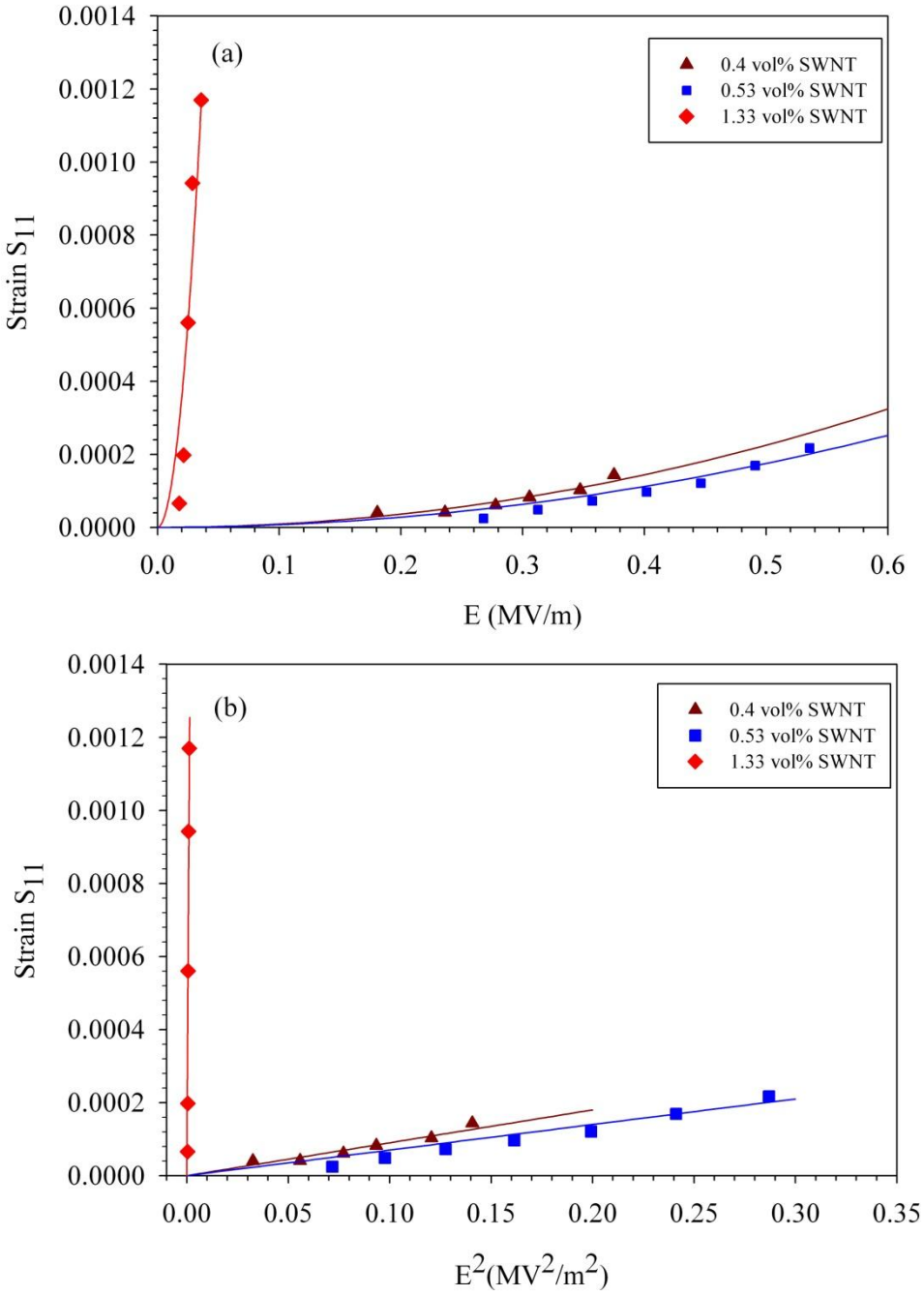

Figure 5.4 (a) S_{11} vs electric field, (b) S_{11} vs squared electric field, for DC signal.

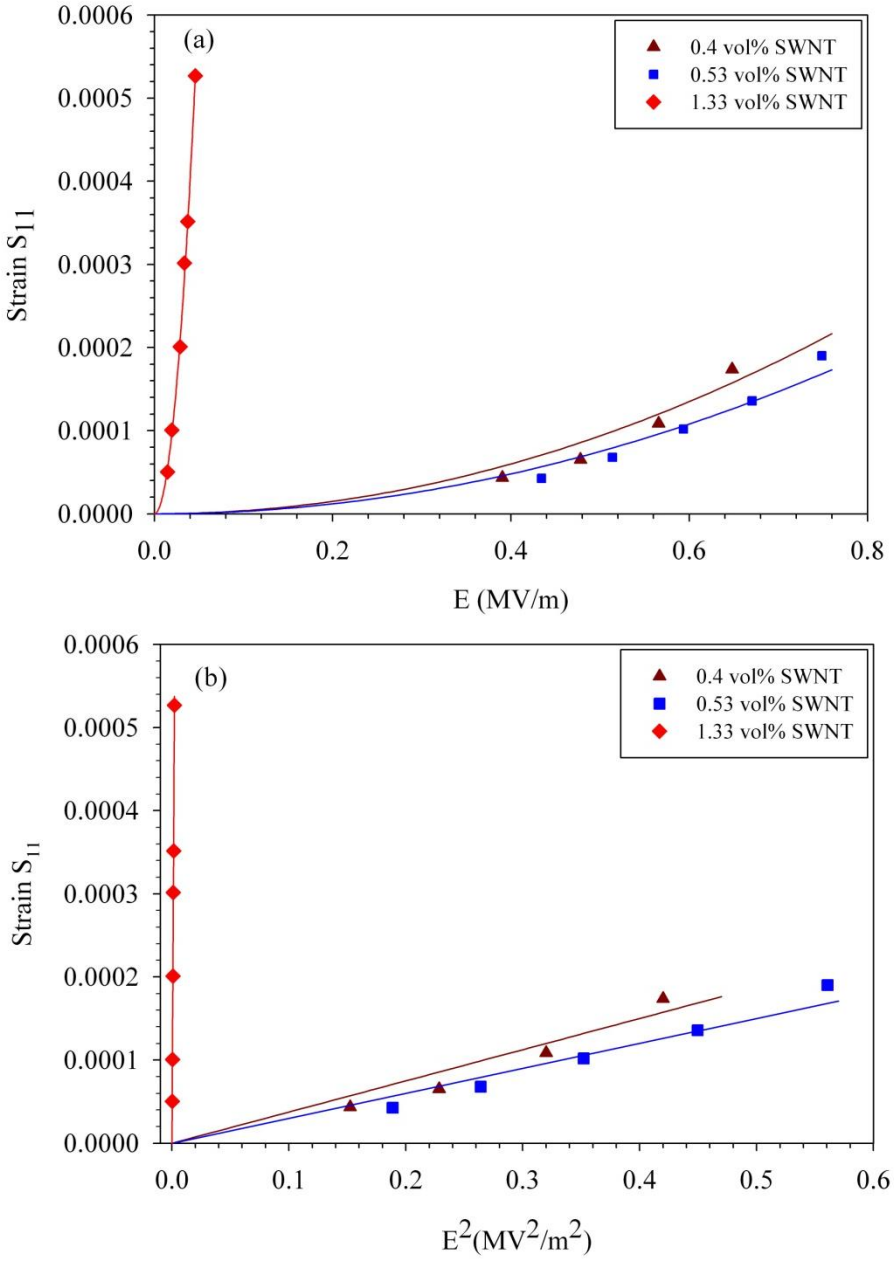

Figure 5.5 (a) S_{11} vs electric field, (b) S_{11} vs squared electric field, for 1 Hz sinusoidal signal.

5.4 Quadratic electromechanical coefficients

The quadratic electromechanical M_{ijkl} coefficients are plotted as a function of SWNT vol% for DC and AC case in Figure 5.6. The M coefficients are zero for pure PVDF and increase with SWNT vol% increases. The M_{1133} and M_{3333} values for 0.4 vol% and 0.53 vol% SWNT samples are comparable and within the standard deviation. A significant enhancement is seen in the values for the 1.33 vol% SWNT sample as was observed in the strain measurements. The M values are compared with known electrostrictive polymers like P(VDF-TrFE)[64], polyurethane[94] and electrostrictive graft elastomer[117]. The M_{33} values for the PVDF composites are 4 to 7 orders of magnitude higher than P(VDF-TrFE) and electrostrictive graft elastomers while M_{13} values are 1to 5 magnitudes higher than electrostrictive polyurethane[94].

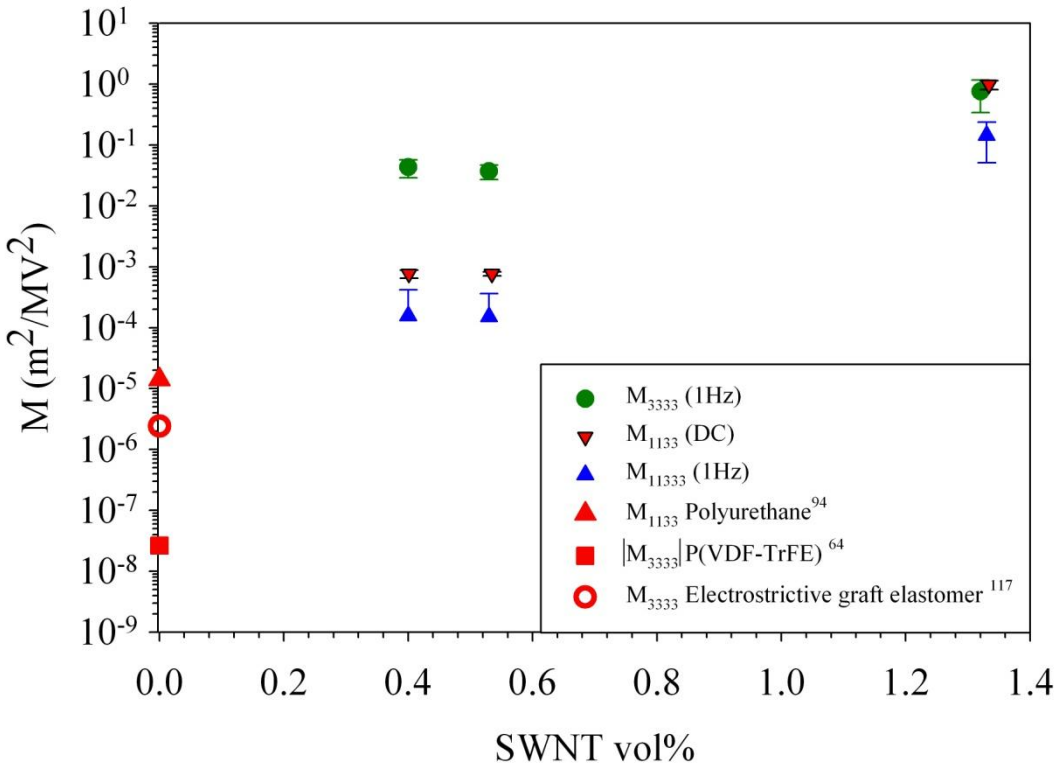

Figure 5.6 M_{1133} (DC and AC) and M_{3333} (AC) as a function of SWNT vol%.

Figure 5.7 shows the dependence of M_{13} on the frequency of the applied field. A steep drop in the M_{13} value is seen when frequency increases from the DC case. Further increase in the frequency shows a gradual decrease in the M_{13} value. The initial drop in the M_{1133} value can be attributed to decrease in contributions from interfacial polarization which is dominant at low frequencies.

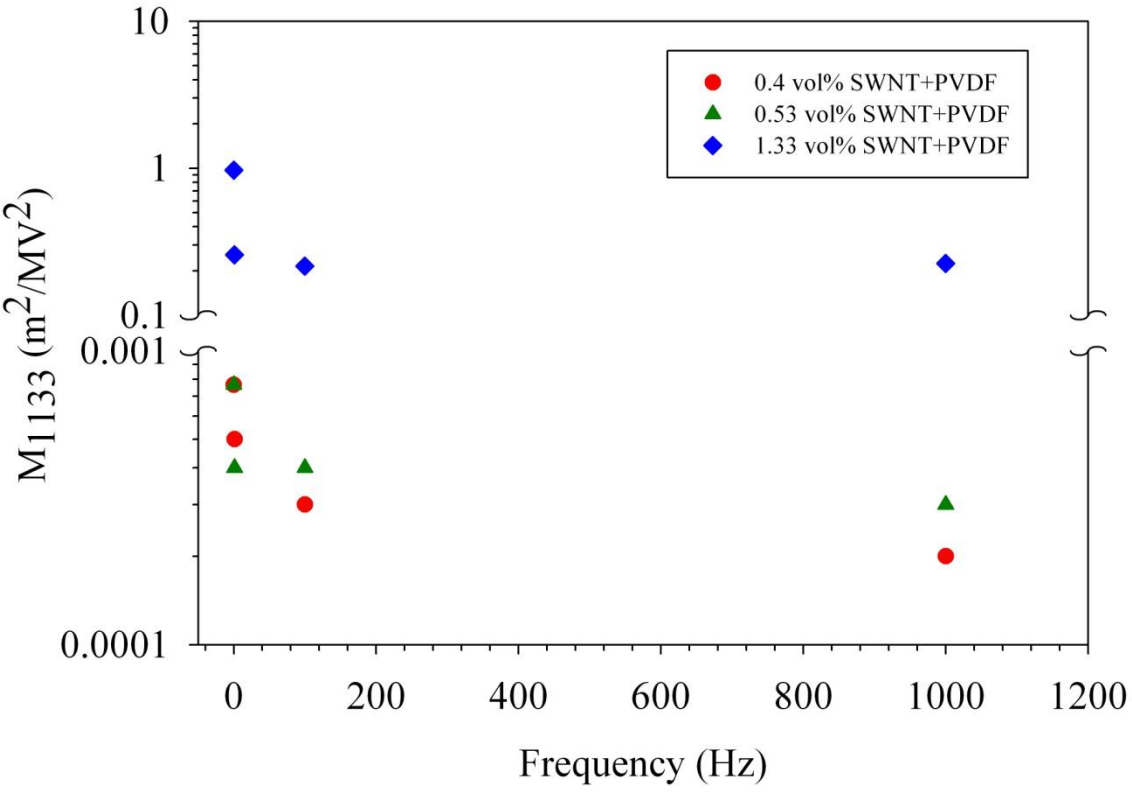

Figure 5.7 M_{1133} as a function of frequency for SWNT-PVDF nanocomposites.

5.5 Contributions to quadratic electromechanical response

As discussed in Sections 3 and 4, quadratic electromechanical strain response can result from SWNT actuation, Maxwell's stress, electrostriction and Joule heating.

5.5.1 SWNT actuation

The effect of electric field on SWNT dimensions and any possible composite strains was studied for the polyimide nanocomposites using Raman spectroscopy earlier. No significant changes to the SWNT structure were observed under applied electric field. This was attributed to the constraining effect of the rigid polyimides on the SWNTs. PVDF however has a very low glass transition temperature (T_g=-35 °C) as compared to the high T_g (200-220°C) polyimides. Hence the effect of electric field on SWNT actuation in SWNT-PVDF nanocomposites is studied using Raman spectroscopy to evaluate the impact of SWNT actuation, if any. Figure 5.8 shows the tangential breathing mode of SWNTs before and after applying DC electric field for a 1.33 vol% SWNT sample during a thickness actuation experiment. Like in the CP2 case, the magnitude of electric field used is comparable to that used during the actuation experiments discussed earlier. No change in the breathing mode of SWNTs is observed. This result confirms minimal structural changes in the SWNTs and minimal strain contributions under applied electric field, potentially resulting from low actuation electric field and the constraining effect of the PVDF matrix.

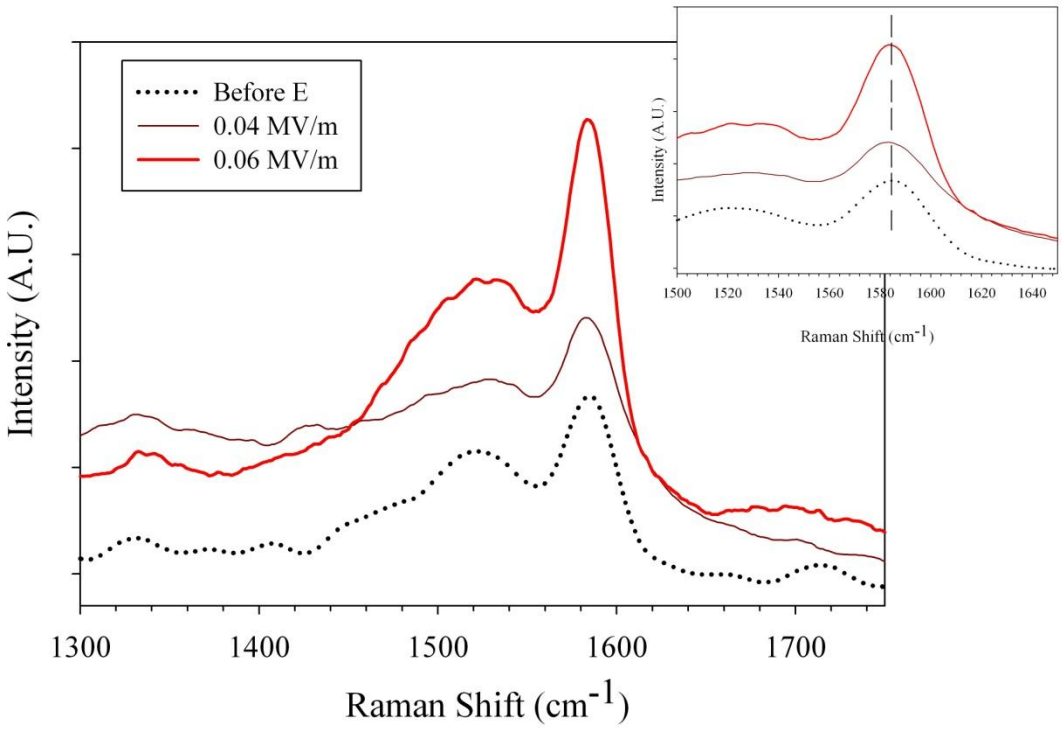

Figure 5.8 In-situ Raman study of Tangential G band frequency of SWNTs in 1.33vol% SWNT-PVDF under applied electric field.

5.5.2 Polarization driven electrostriction

To evaluate polarization driven electrostriction as the mechanism responsible for the enhanced quadratic electromechanical response, it is necessary to evaluate SWNT dependent polarization in PVDF. Figure 5.9 shows the effective dielectric constant ε_{33} as a function of frequency at different SWNT content. An increase in the value is observed with SWNT content up to 0.53 vol% SWNT sample at frequencies below 100 Hz. The dielectric constant of 1.33 vol% SWNT composites could not be measured at low frequencies due to the high conductivity of the samples. Figure 5.10 shows the dielectric constant extrapolated to DC case of the SWNT-PVDF nanocomposites. The dielectric constant increases with SWNT vol% and then plateaus off. The high ε_{33} dielectric constant values observed in Figure 5.10 indicate induced polarization in the PVDF films attributed to interfacial polarization and possible presence of micro/nano capacitors due

to SWNTs. Furthermore, contributions to polarization could result if there is transformation of the non-polar α phase to polar γ phase due to interaction with SWNTs as discussed earlier [3, 4, 69]. In the following sections we investigate the enhancement in polarization in both semi-crystalline and amorphous regions of PVDF due to addition of SWNTs.

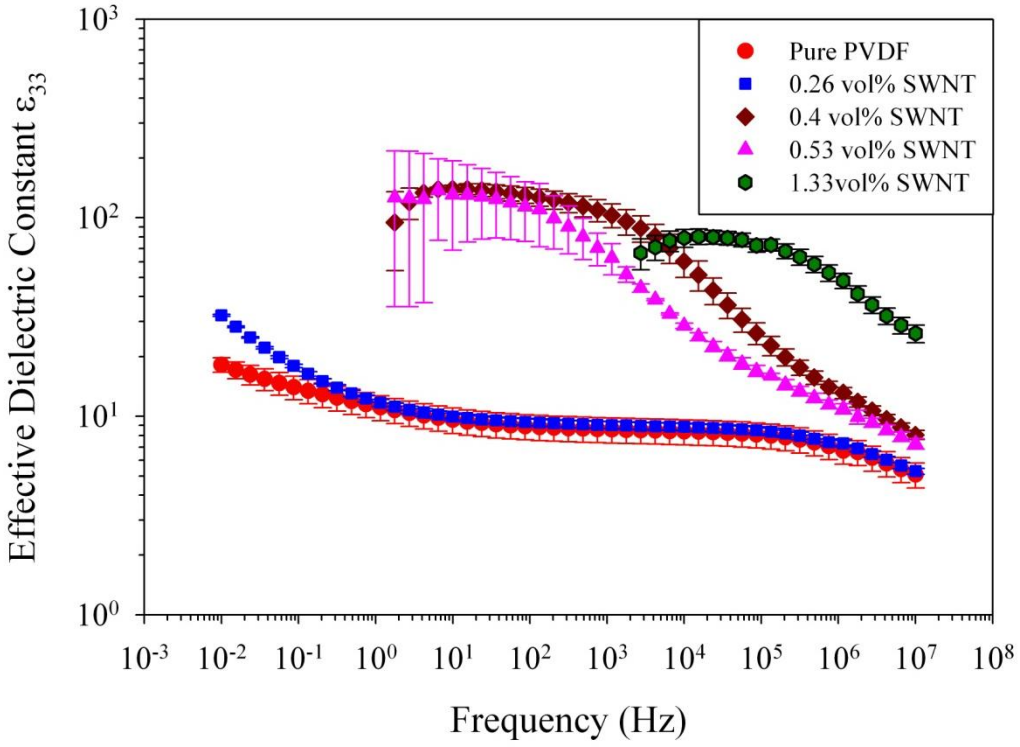

Figure 5.9 Effective dielectric constant vs frequency at different SWNT loading.

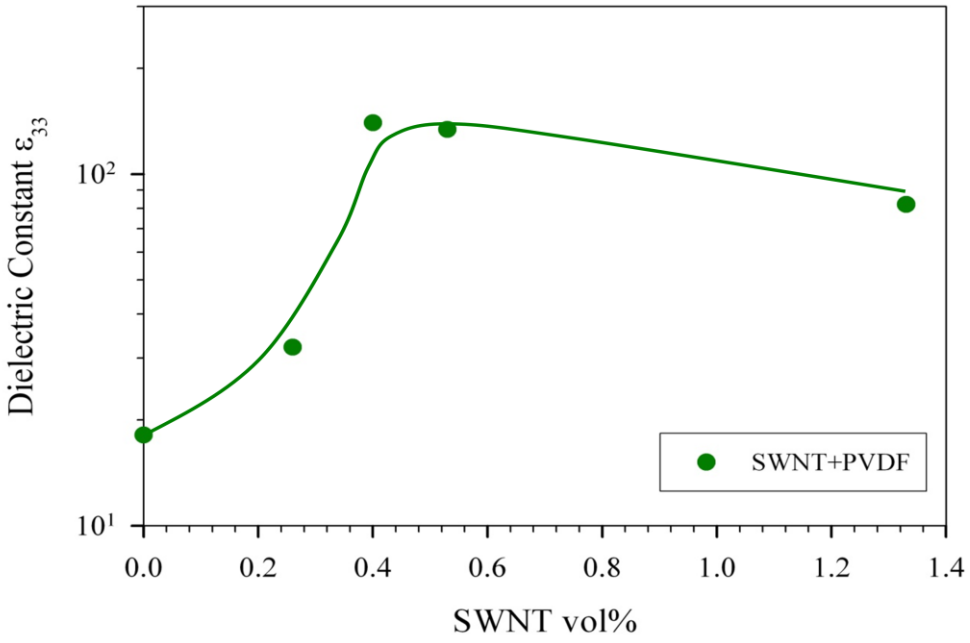

Figure 5.10 Effective dielectric constant (extrapolated to DC) vs SWNT loading. Solid line is drawn to ease reading of data.

5.5.2.1 Polar crystalline contributions

In this section we evaluate the effect of SWNTs on the crystalline microstructure of PVDF in an effort to evaluate the polarization in the crystalline phase of SWNT-PVDF nanocomposites.

FTIR (ATR and transmission mode) and WAXs are employed to evaluate the crystalline phase in pure PVDF and SWNT-PVDF nanocomposites. Figure 5.11(a) shows the FTIR-ATR spectrum of the samples. Pure PVDF film shows characteristic peaks for α phase at 615, 765, 795 and 976 cm^{-1}. Distinct characteristic γ peaks are also seen at 510 cm^{-1} and 834 cm^{-1} indicating the presence of some γ phase[118]. It is important to stress that the peak observed at 834 cm^{-1} that is a characteristic of γ phase and not the β phase (β peak is generally observed at 840 cm^{-1}). The SWNT-PVDF samples on the other hand show a suppression of the α phase peaks along with increase in γ crystalline phase peaks at 812, 834 and 1233 cm^{-1}. The increase in γ phase can be further confirmed

from figure 5.11(b) that shows shallow characteristic γ peaks at 812 and 1233 cm^{-1} in pure PVDF but an increase in the 1233 cm^{-1} peak for the 1.33 vol% SWNT-PVDF.

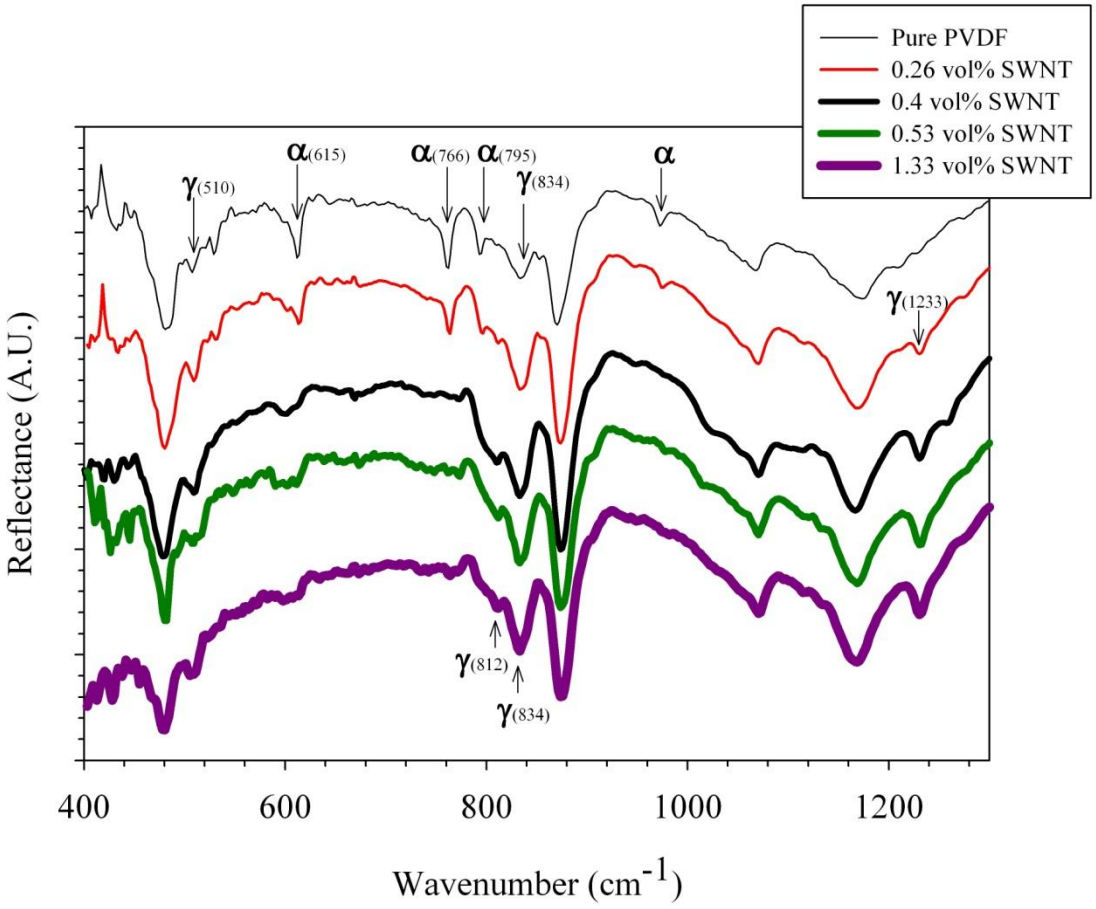

(a)

Figure 5.11 (a) FTIR-ATR spectrum for PVDF and SWNT-PVDF nanocomposites, (b) FTIR-ATR showing presence of some γ phase in pure PVDF and 1wt% SWNT-PVDF.

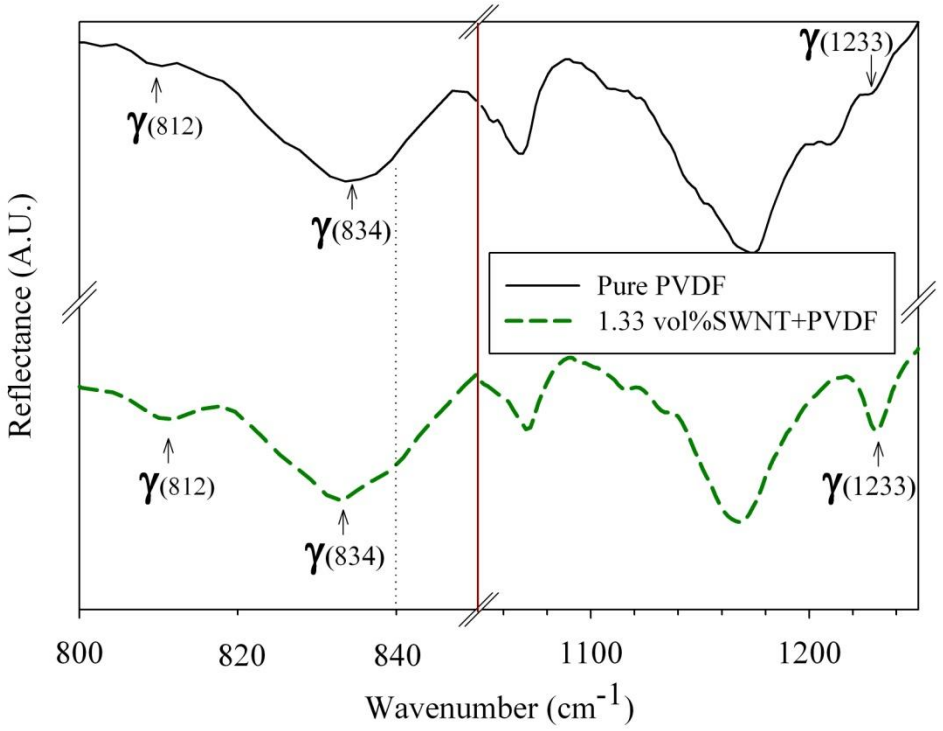

(b)

Figure 5.11 Continued.

Wide angle X-ray (WAXs) spectrum is also used to confirm the results of FTIR. Figure 5.12 shows the WAXs spectrum of PVDF and SWNT-PVDF nanocomposites. Pure PVDF shows distinct peaks at 18.6°, 20.1° and 27° that indicate presence of α phase[119]. SWNT - PVDF nanocomposites show distinct peaks at 18.7°, 20.3° and 39.5°. The 20.3° peak has been attributed to both γ [119, 120] and β [121], although others have placed the β peak at 20.6°[119]. However the shoulder at 18.7° and the peak at 39.5° can definitely be attributed to the γ phase [119, 120] and not to β. Along with the observation of γ peaks, we also observe the absence of the α peak at 27° in the SWNT-PVDF nanocomposites indicating suppression of α phase and increase in the γ phase.

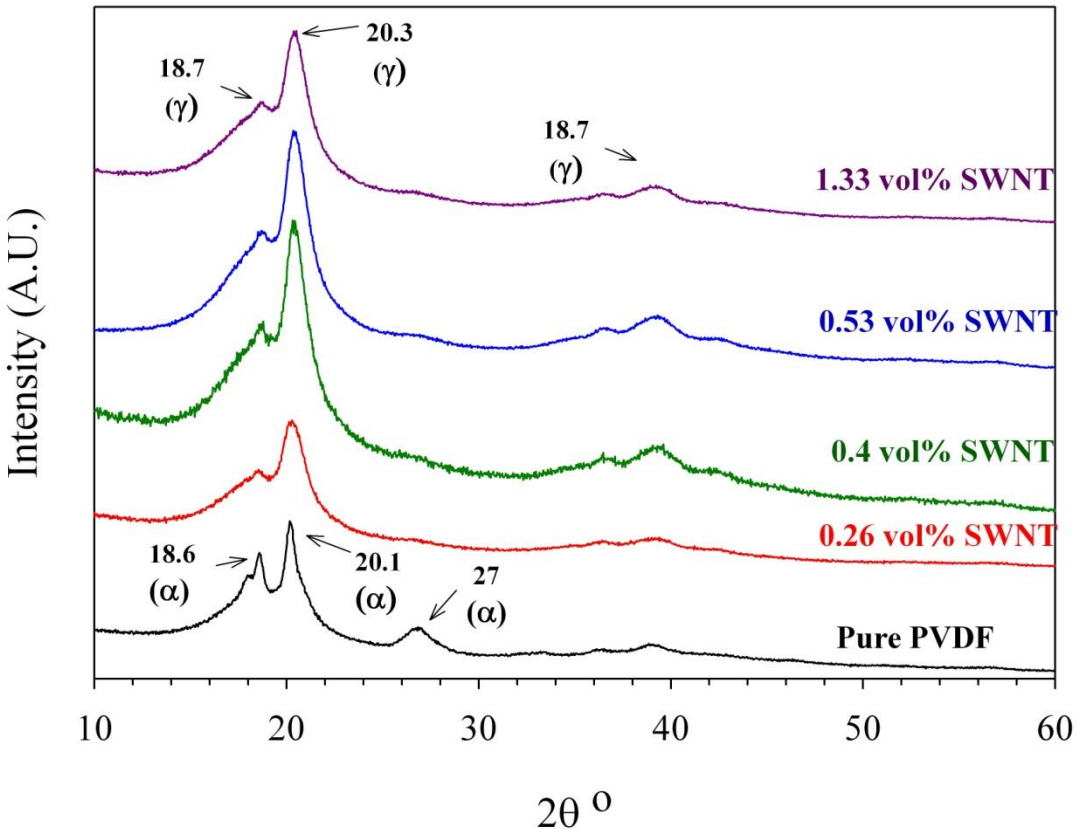

Figure 5.12 WAXs spectrum of unstretched PVDF and SWNT-PVDF nanocomposites.

The differential scanning calorimetry (DSC) studies offer further insight into the effect of SWNTs on phase transformation and crystallization of PVDF. Figure 5.13(a) shows the endotherm peaks of pure PVDF and SWNT-PVDF nanocomposite samples. The melting temperatures, percent crystallinity and crystallization temperatures of the nanocomposites are listed in Table 5.1. In general the melting temperature of the samples increases with increase in the SWNT loading which correlates to the increase in γ phase seen in Figures 5.11 and 5.12. Pure PVDF, which has a combination of α and γ phases, shows a melting temperature of 162°C while PVDF-1.33 vol% SWNT composite, which has a predominantly γ phase, has a melting temperature of 168°C. No significant effect of SWNT content is seen on the crystallinity. Figure 5.13(b) shows the

effect of SWNT content on the crystallization temperature of PVDF. An upshift in the crystallization temperature of PVDF with SWNT content indicates a nucleating effect of SWNTs on the crystallization of pure PVDF. An increase in the crystallization temperature from 131°C to 136°C is observed as the SWNT content increases from 0 to 1.33 vol%. The relatively unchanged crystallinity in the SWNT-PVDF nanocomposites observed in Table 5.1 indicates that SWNTs also hinder the growth of crystals that probably counters any nucleation effect.

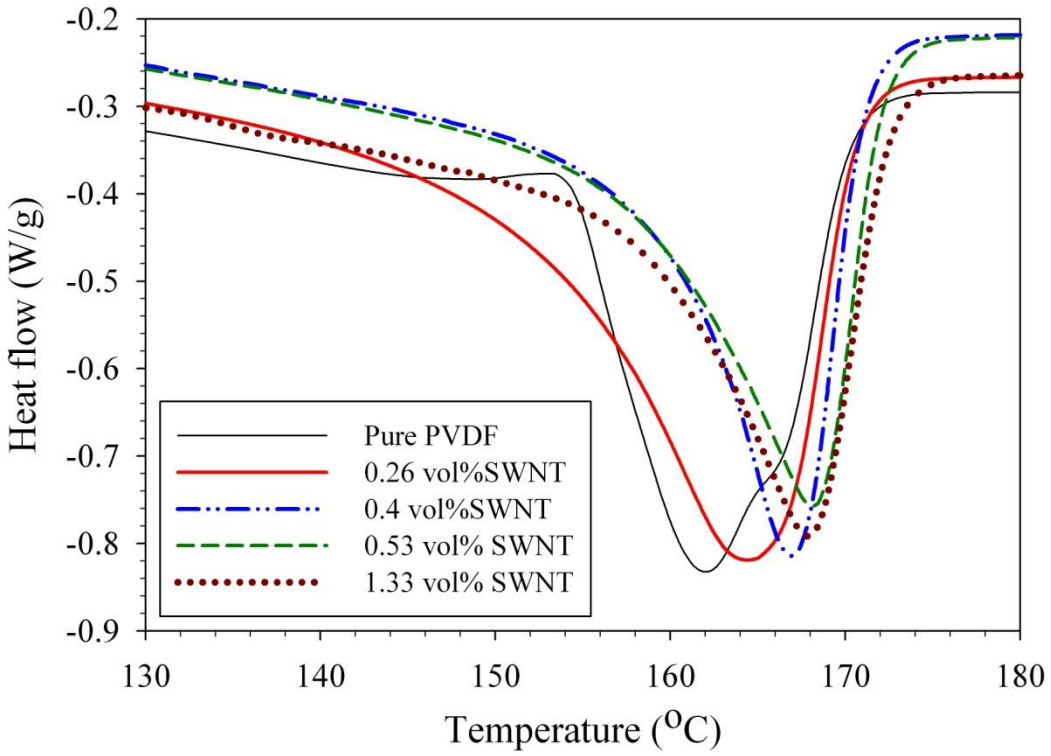

(a)

Figure 5.13 (a) DSC melting peaks for PVDF and SWNT-PVDF nanocomposites and (b) DSC crystallization peaks for PVDF and SWNT-PVDF nanocomposites.

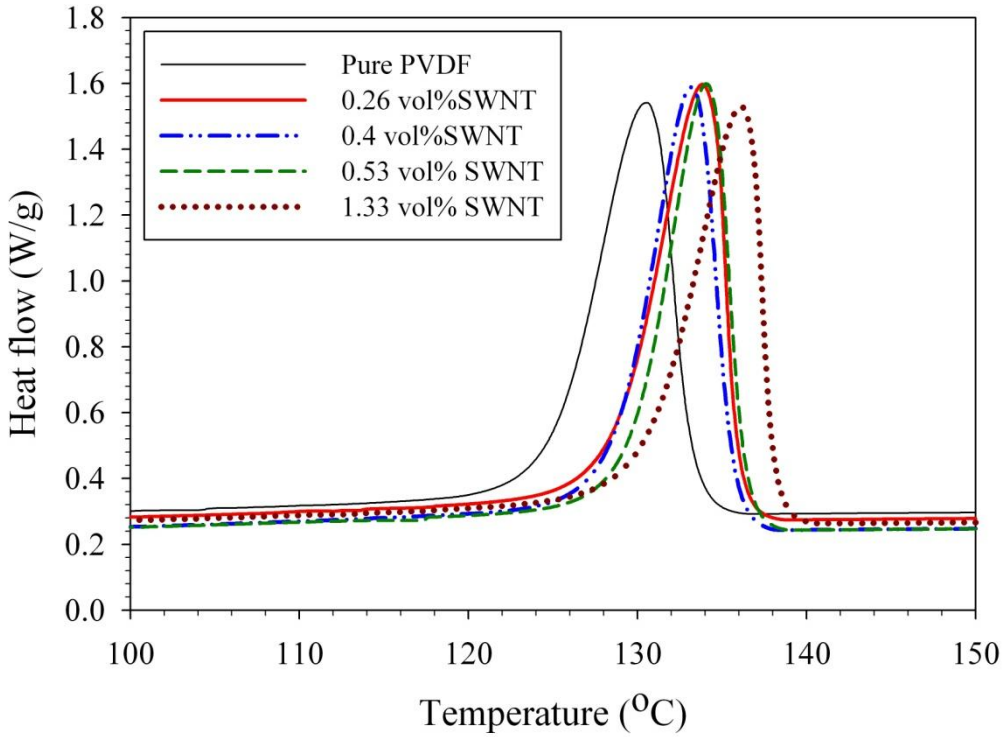

(b)

Figure 5.13 Continued.

Table 5.1. DSC results of SWNT-PVDF nanocomposites.

SWNT vol%	Melting Temperature (°C)	%Crystallinity	Crystallization Temperature (°C)
0	162	51	131
0.26	164	53	134
0.4	167	50	133.5
0.53	167.5	49	134
1.33	168	51	136

The hypothesis of SWNTs acting as nucleation sites is also confirmed by SEM studies of the surface of the PVDF and SWNT-PVDF films. Figure 5.14 shows the polygonal plates formed on the surface of the films. These features are a result of the

spherulite formation near the surface of the films[4, 122, 123]. Presence of SWNTs decreases the spherulite size indicating that SWNTs provide nucleation sites. The decrease in the spherulite size can also be related to the formation of the γ phase. β and γ crystals are generally smaller than the α crystals[124].

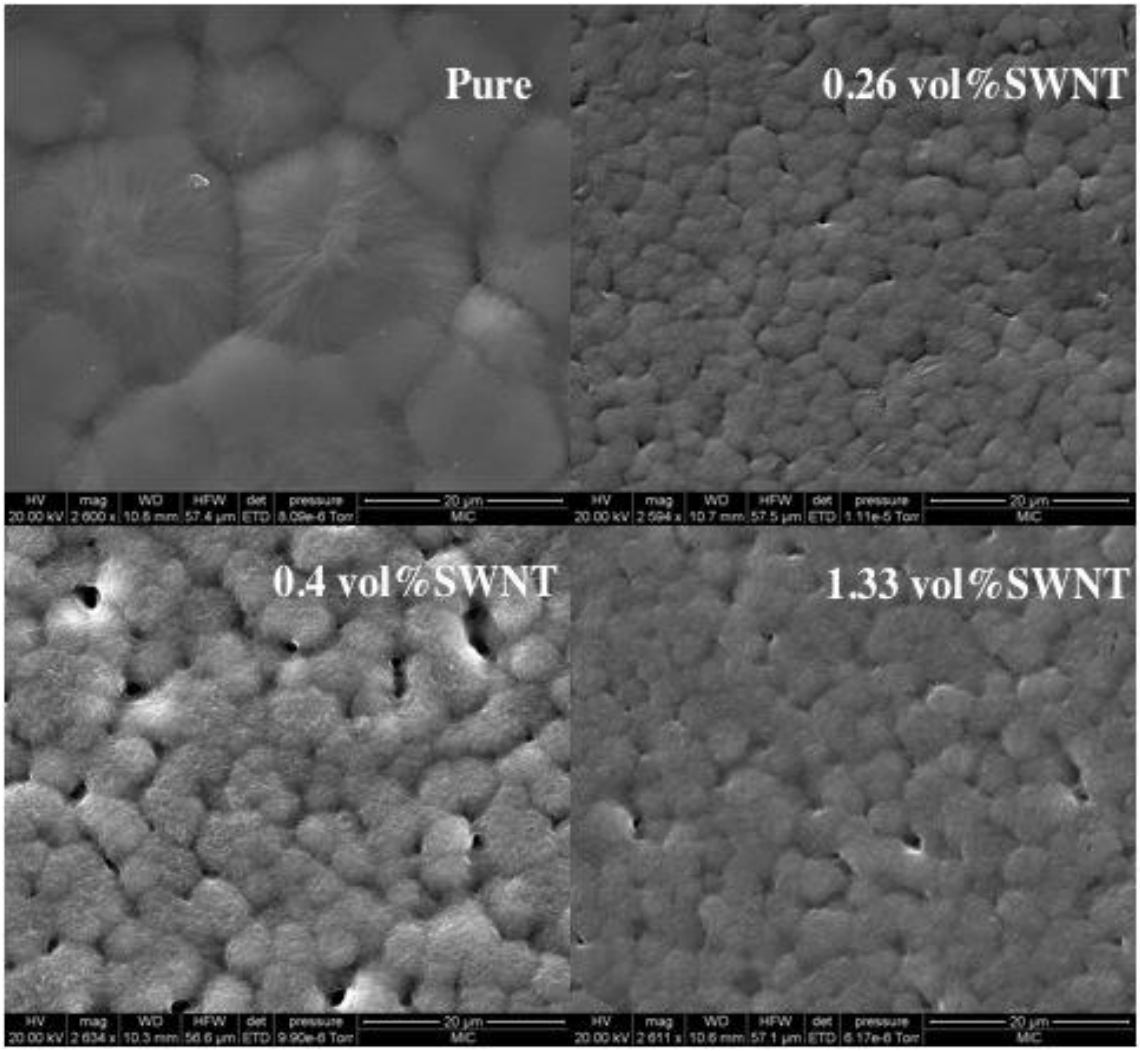

Figure 5.14 Effect of SWNTs on the polygonal plates observed on the surface of the SWNT films.

The strong SWNT-PVDF affinity, as evidenced by the Raman spectroscopy results (Figure 5.1), results in the non-polar to polar conformation change in PVDF. The

SWNT-PVDF noncovalent interaction is further confirmed in Figure 5.15. An upshift of 5 cm^{-1} is observed in the G band frequency of SWNTs between SWNT+DMAc and PVDF+1.33vol%SWNT+DMAc solution. This result confirms the interaction between SWNTs and PVDF as the cause of the upshift in the tangential G band frequency of SWNTs.

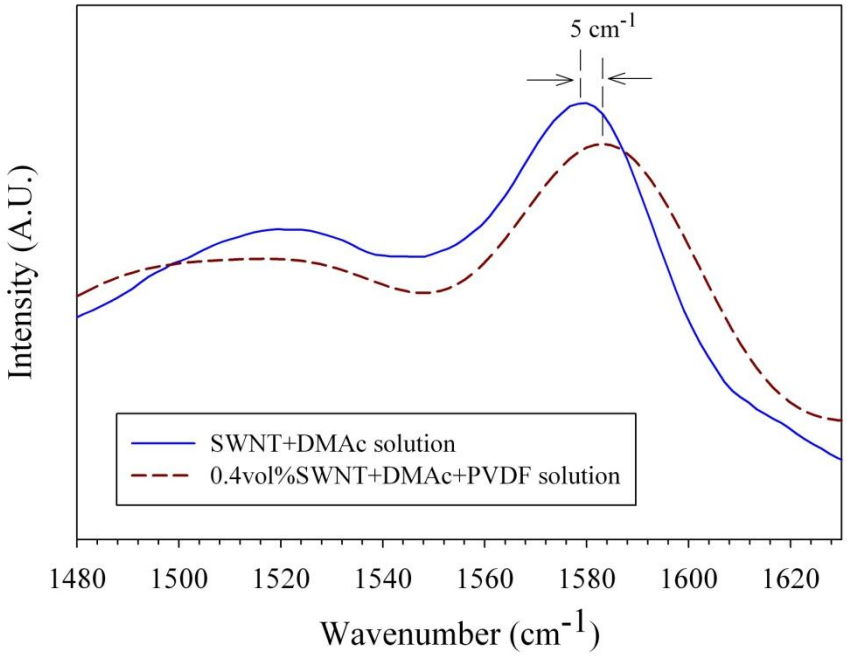

Figure 5.15 Upshift in tangential G band frequency of SWNTs in the 0.4vol% SWNT-PVDF solution.

The noncovalent interaction between the electronegative fluorine and SWNTs can cause a change of the non-polar α phase to a polar γ phase due to a change in alternating trans-gauche to the trans-trans type conformation of the polymer chain. Interactions between nanoinclusions like nanoclay and PVDF have been suggested to cause such conformation changes[125, 126]. The change in the chain conformation in our nanocomposites is however not complete and results in the TTTG conformation resulting in the γ phase. This can be attributed to internal chain rotations at higher temperatures as suggested by Ramasundram et al[126]. This could also be a result of a

weaker non-covalent interaction between SWNTs and PVDF as compared to the stronger ion-dipole interaction between nanoclay and PVDF[125, 126]. As mentioned above, this phase change is accompanied by decrease in the spherulite size as suggested by the SEMs in Figure 5.14 This scenario is illustrated as a schematic in Figure 5.16. The proposed scenario would explain the increase in the γ phase with SWNT content. Increasing SWNT content would result in more PVDF chains interacting with SWNTs resulting in further increase of the γ phase.

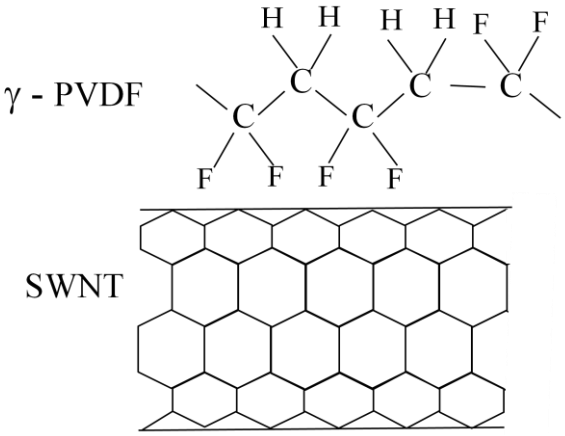

Figure 5.16 Schematic illustrating the possible scenario of the SWNT-PVDF interaction as the cause of α to γ phase change.

The increase in the crystalline γ phase with SWNT content can be quantified from FTIR-Transmission spectrum using the Lambert-Beer law as discussed by Gregorio et al[127]. The 510 cm^{-1} IR peak can be attributed to β phase as well as γ phase. However the FTIR-ATR and WAXs results from Figures 5.11 and 5.12 confirms the presence of γ phase and the absence of any β phase in our unstretched samples. Assuming the IR absorption in the transmission mode follows the Lambert-Beer law, the A_γ absorbency at 510 cm^{-1} can be expressed as:

$$A_\gamma = \log \frac{I^0}{I} = K_\gamma C X_\gamma L \qquad (5.1)$$

where I^0 and I are the incident and transmitted radiations, K_γ (=5.8 x 10^4 cm^2/mol) is the absorption coefficient at 510 cm^{-1} derived by Gregorio et al[127], X_γ is the crystallinity of

the γ phase, C is the monomer concentration that can be derived from the density of γ phase (1.94 g/cm^3 [128]) as 0.0303 mol/cm^3 and L is the thickness of the sample. The crystallinity of the γ phase can then be computed as:

$$X_\gamma = \frac{A_\gamma}{K_\gamma CL} \tag{5.2}$$

This technique gives a rough estimate of X_γ and can be used to compare γ crystallinity in pure PVDF and SWNT-PVDF composites. Figure 5.17(a) shows the transmission absorbance normalized by thicknesss L of the 510 cm^{-1} γ peak for pure PVDF and SWNT-PVDF nanocomposites up to 0.4wt% SWNT. The thickness of the 1.33 vol%SWNT samples was high (due to initial high viscosity of the nanocomposite solution) and hence could not give a discernible absorbance spectrum. The X_γ for the pure PVDF and SWNT-PVDF nanocomposites can be computed from equation 5.2 and is plotted in Figure 5.17(b). The X_γ shows a marked increase in the SWNT-PVDF nanocomposites that confirms the qualitative assessment of the FTIR-ATR and WAXs data discussed earlier. X_α computed for the pure PVDF using $K_\alpha = 6.1 \times 10^4$ cm^2/mol for the 766 cm^{-1} peak is around 0.28 (28%). Considering the X_γ for pure PVDF was computed as 0.18 (18%), the values computed for crystallinity using the Lambert-Beer law are marginally lower than those measured using DSC. The α peak at 766 cm^{-1} for the SWNT-PVDF nanocomposites however could not be distinguished convincingly over the noise in the spectrum and hence X_α was not computed for the nanocomposites using the Lambert-Beer law.

Takakubo et al[129] have computed a spontaneous polarization of 0.023 C/m^2 in the γ phase PVDF assuming a polar unit cell. The increase in the γ phase crystallinity shown in Figure 5.17 indicates an increase in polarization contributions from the polar crystalline microstructure in the SWNT-PVDF nanocomposites. Figure 5.18 depicts possible polarization resulting from micro/nano capacitors in the crystalline phase of SWNT-PVDF nanocomposites.

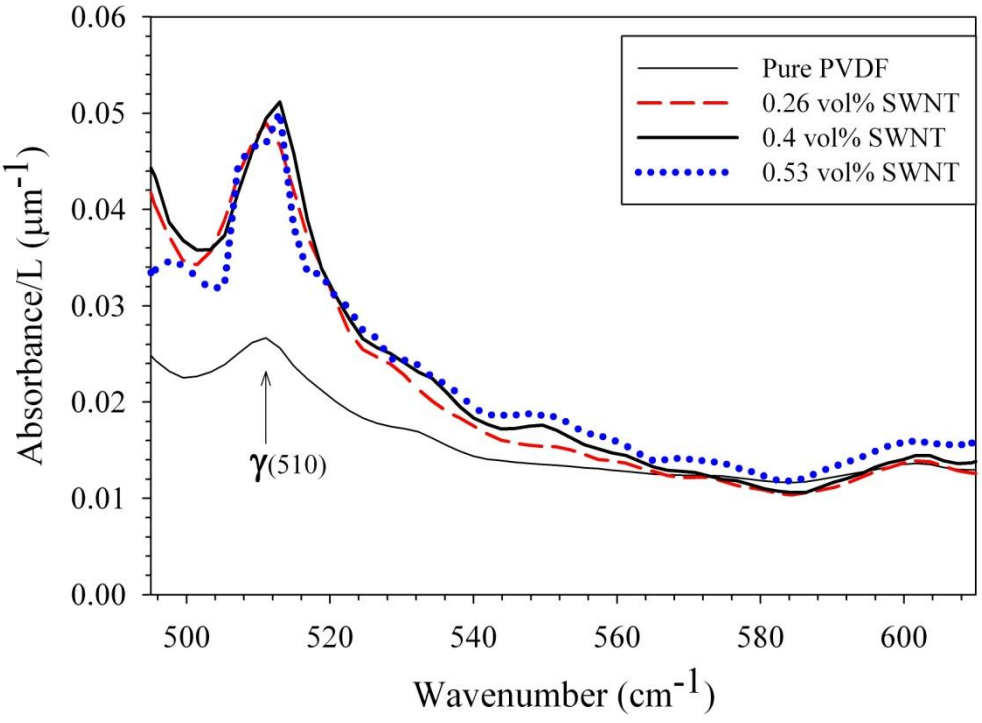

(a)

Figure 5.17 (a) FTIR-Transmission spectrum for 510 cm^{-1} γ peak for PVDF and SWNT-PVDF nanocomposites, (b) γ crystallinity computed from Lambert – Beer law as a function of SWNT vol%.

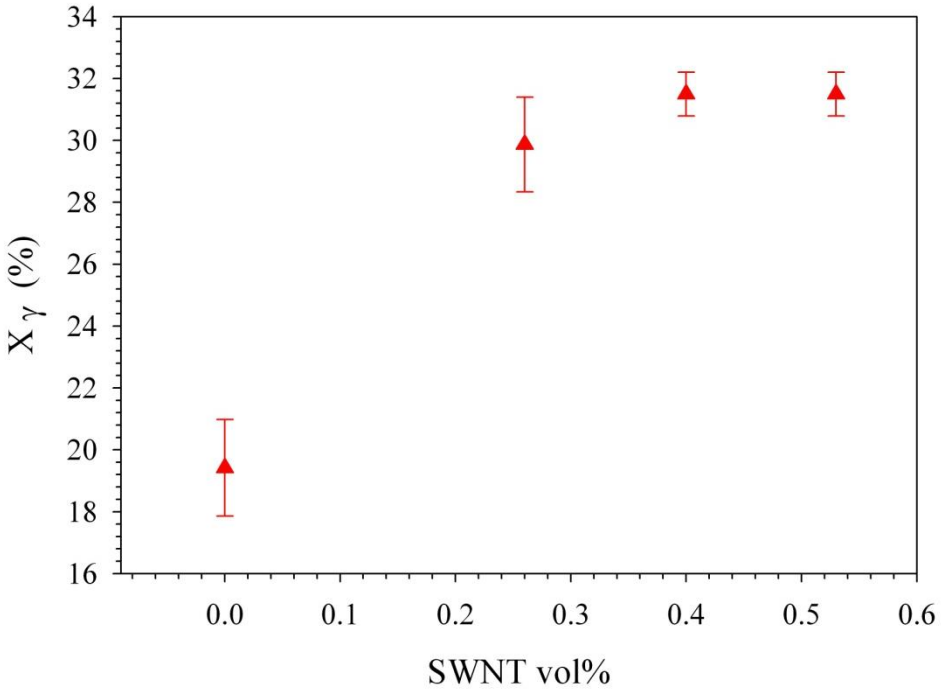

(b)

Figure 5.17 Continued.

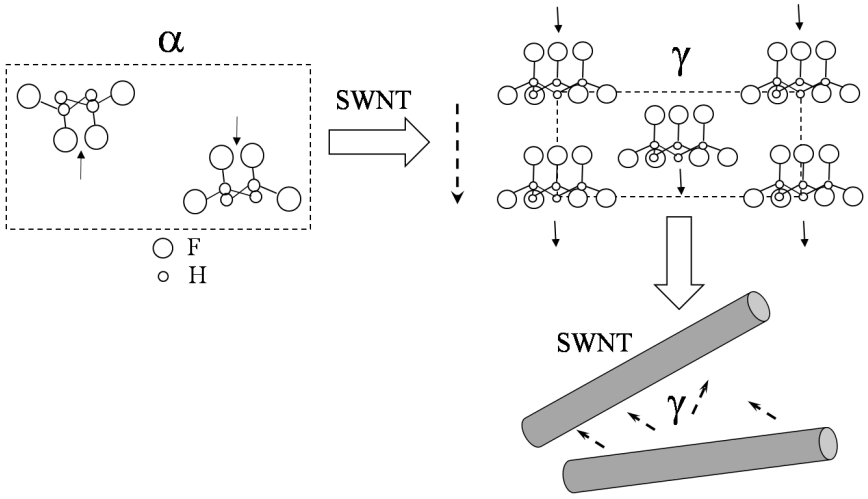

Figure 5.18 Polarization due to formation of crystalline polar γ phase by adding SWNTs (crystalline phase schematics adapted from[114]).

5.5.2.2 Polarization contributions from amorphous region

Figure 5.19 depicts dielectric constant ε_{33} vs temperature for pure PVDF and SWNT-PVDF samples. The dielectric constant shows a jump in value (dielectric relaxation strength, $\Delta\varepsilon$) around the glass transition temperature (T_g=-36 °C) for pure PVDF and this value increases with SWNT content. Figure 5.20 shows the tan (δ) peaks associated with this dielectric constant jump. These observations signify enhanced dipolar relaxation in the nanocomposite samples that is attributed to the α_A relaxation associated with the amorphous PVDF chains[130, 131]. Table 5.2 lists the increase in the dielectric relaxation strength with SWNT content. Figure 5.21 shows the predicted remnant polarization in the amorphous phase of SWNT-PVDF nanocomposites as a function of SWNT content based on equation 3.8. The results indicate an increased dipolar relaxation in amorphous PVDF chains due to the presence of SWNTs. This could result from (i) increased dipolar mobility due to the SWNTs acting as extension of electrodes or (ii) dipoles from SWNT – PVDF non-covalent electron-donor acceptor relationship. Thus increased polarization in SWNT-PVDF samples can be seen in both the crystalline and amorphous regions of the SWNT-PVDF nanocomposites. Figure 5.22 depicts the possible polarization scenarios in the amorphous phase of SWNT-PVDF nanocomposites resulting from SWNT-PVDF interaction and micro or nanocapacitors.

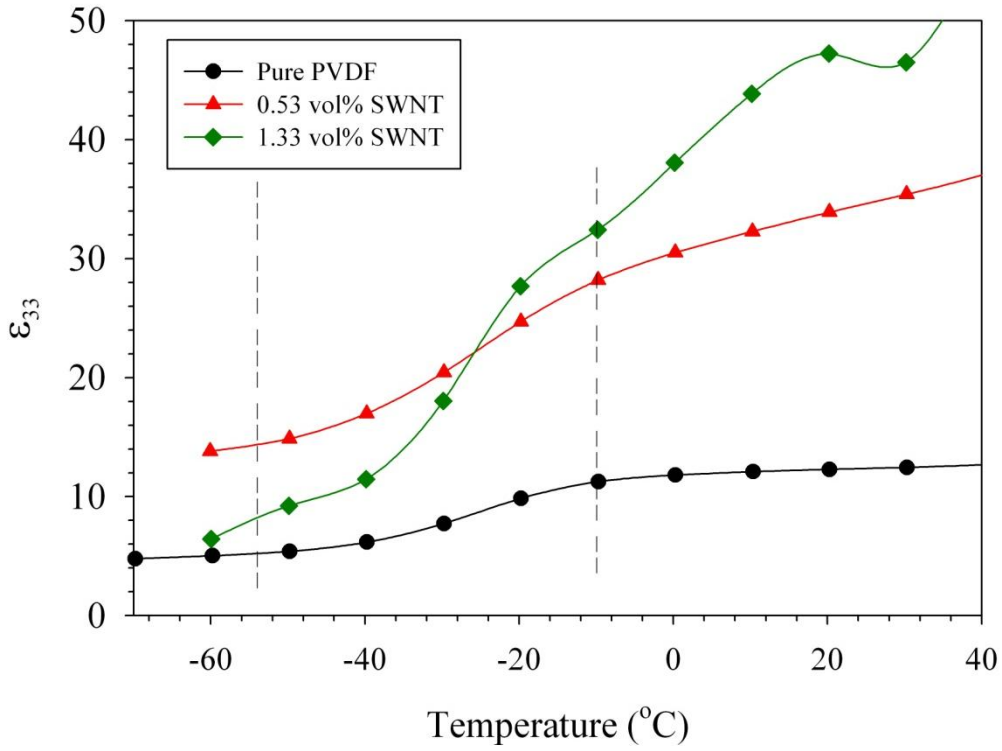

Figure 5.19 Dielectric constant ε_{33} vs temperature for SWNT-PVDF.

Table 5.2 Δε for SWNT-PVDF nanocomposites.

SWNT vol%	$\Delta\varepsilon_{500Hz}$
0	6
0.53	17
1.33	23

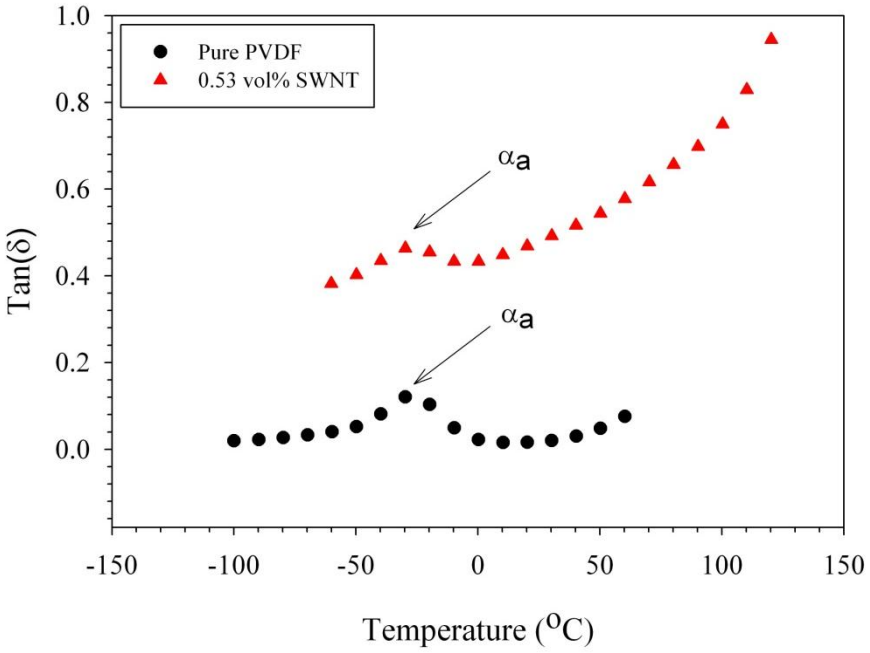

(a)

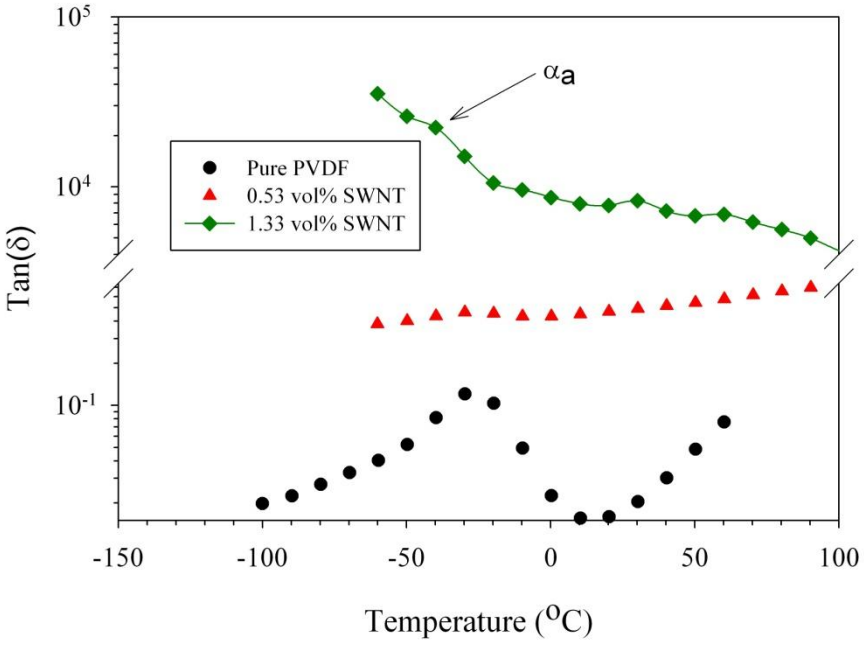

(b)

Figure 5.20 (a) Tan (δ) vs temperature without high SWNT content. (b) Tan (δ) vs temperature with high SWNT content.

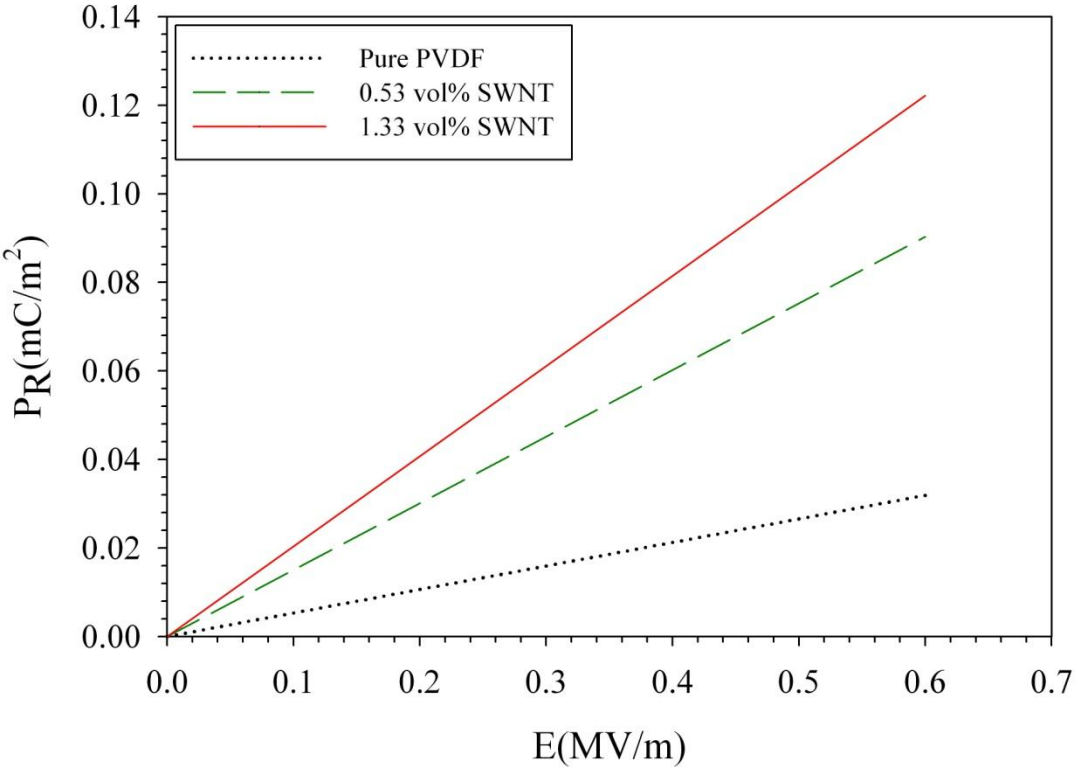

Figure 5.21 Remnant polarization predicted for SWNT – PVDF nanocomposites for the actuation electric fields used.

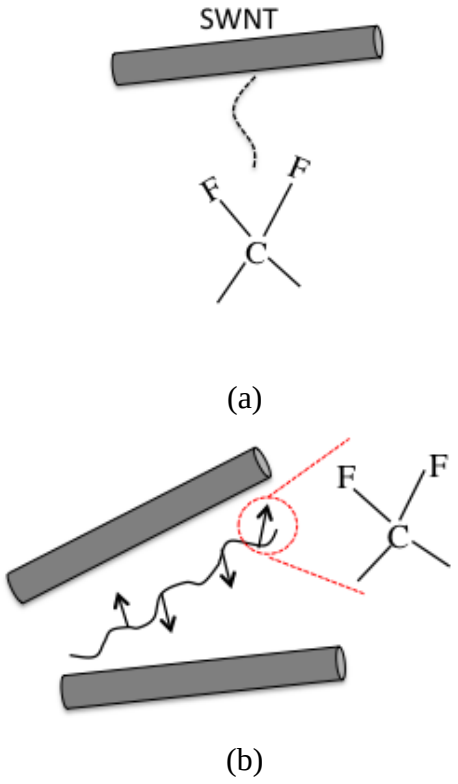

Figure 5.22 Polarization due (a) SWNT interaction and, (b) Micro/nano capacitors in amorphous phase of SWNT-PVDF nanocomposites.

5.5.3 Maxwell's stress

Calculations for electrostatic strains for SWNT-PVDF nanocomposites based on the methodology discussed for the polyimide nanocomposites leads to strains as low as 10^{-9} -10^{-10}. Table 5.3 lists the storage modulus of the SWNT-PVDF nanocomposites at room temperature used in the calculations. It is thus reasonable to assume that electrostatic actuation does not have a significant contribution in the electromechanical strains measured.

Table 5.3 Storage modulus E_s of SWNT-PVDF nanocomposites at room temperature.

SWNT loading (Vol%)	Storage Modulus E_s (MPa)
0	1600
0.4	1740
0.53	1680
1.33	2100

5.5.4 Joule heating

Finally the quadratic electromechanical response can also result from Joule heating. Figure 5.23 shows the increase in temperature of the nanocomposites with the 1 Hz AC sinusoidal electric field measured using a contact thermocouple. From Figure 5.23 it can be inferred that the temperature rise in the 0.4 vol% SWNT and 0.53 vol% SWNT samples is minimal. The temperature rise at the electric fields that caused thickness actuation for these nanocomposites (Figure 5.3) was less than 0.5 °C. An Infrared IR temperature gun also showed comparable temperature change data. The conductive 1.33 vol% SWNT samples however did show a temperature increase of about 4°C. Since PVDF is already above the glass transition temperature (T_g) at room temperature (T_g for PVDF is -35°C) Joule heating can have a possible contribution towards the strain response of 1.33 vol% SWNT content samples. Figure 5.24 (a) shows the projected Joule heating contributions and the corrected strain values of 1.33 vol% SWNT samples using the temperature increase data and the coefficient of thermal expansion (1.1×10^{-4} /°C, measured using the thermo mechanical analyzer (TMA)). Figure 5.24(b) shows the corrected M_{33} coefficient for the 1.33 vol% SWNT data. The Joule heating contributions to the measured strain response were not significant. For example at 0.32 MV/m applied AC field to 1.33 vol%SWNT samples the measured thickness strains are 0.11% while the projected Joule heating strains are around 0.02%. The M_{3333} value shows a change from 0.75 m^2/MV^2 to 0.52 m^2/MV^2, which was within

the standard deviation. Though the results so far indicate minimal Joule heating contributions, they need to be systematically studied by more precise techniques of temperature measurements like infrared thermal imaging.

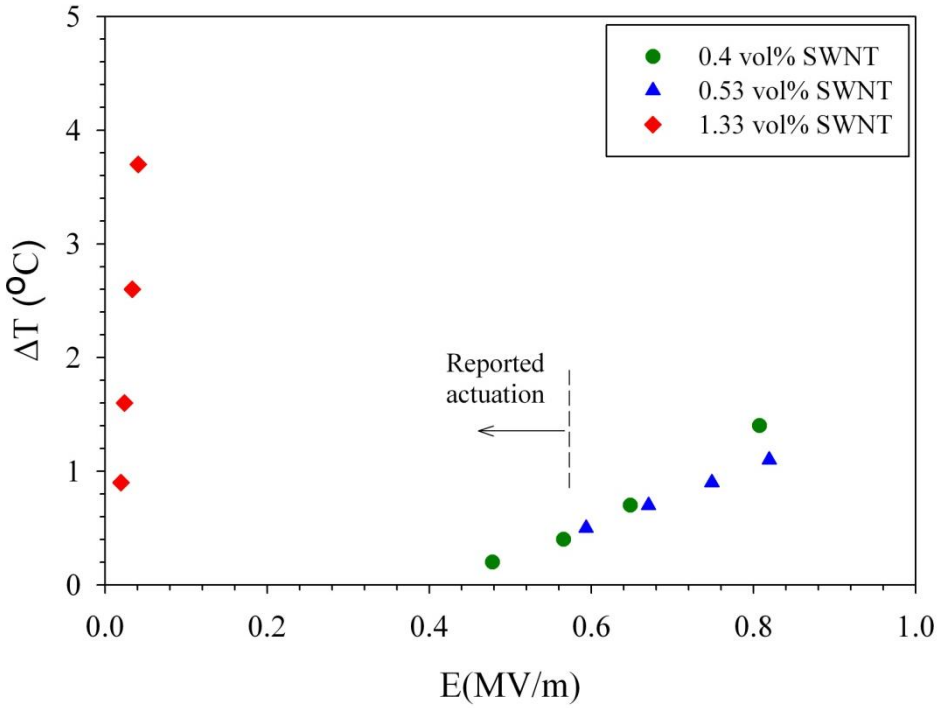

Figure 5.23 Temperature increase in PVDF nanocomposites due to Joule heating for 1 Hz AC signal.

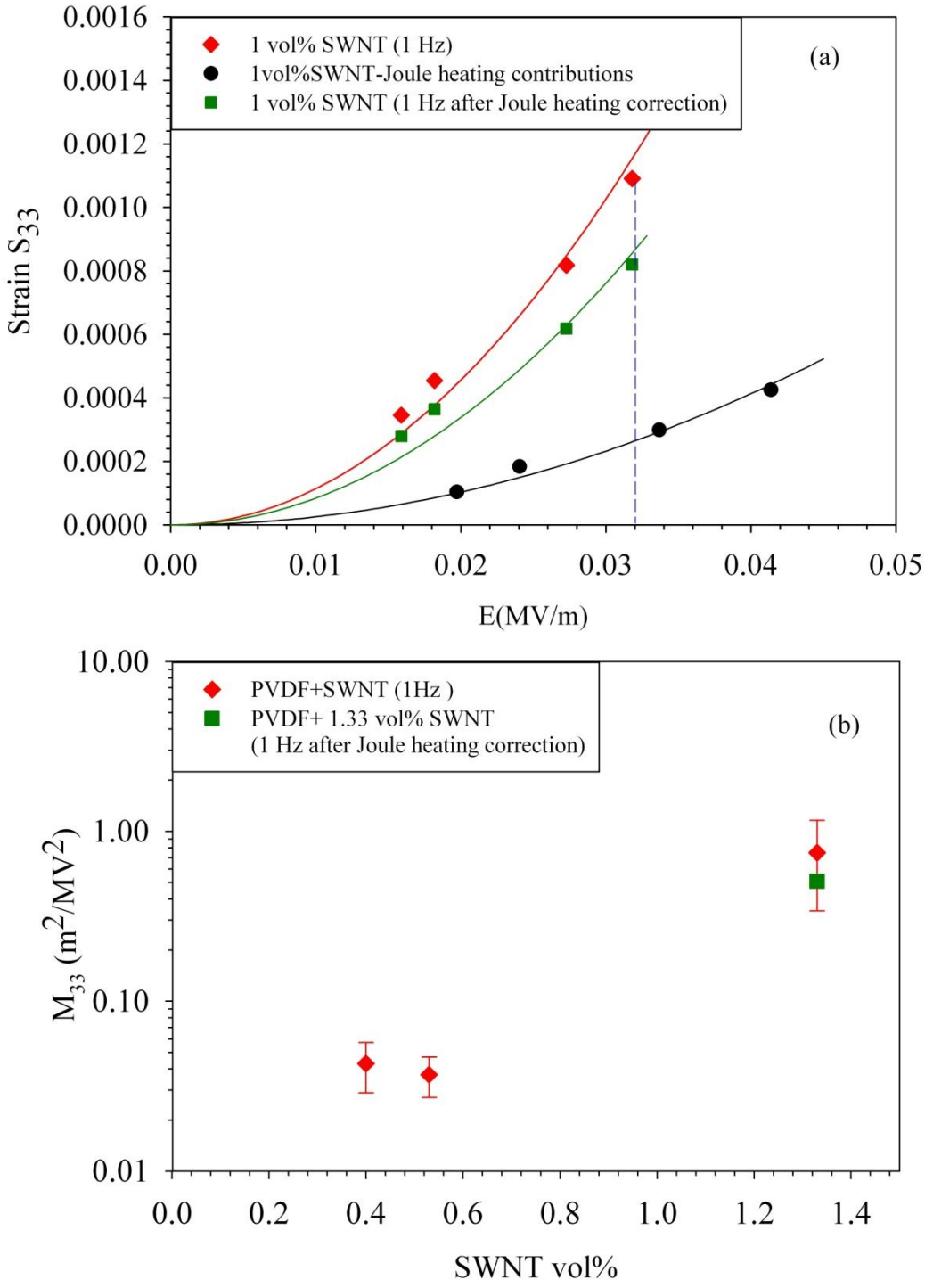

Figure 5.24 (a) Joule heating contributions to strain response of 1.33 vol% SWNT+PVDF composites, (b) M_{3333} value for 1.33 vol% SWNT+PVDF after Joule heating correction compared with measured M_{3333}.

5.6 Comparison of electrostrictive response of SWNT-PVDF with SWNT-polyimide nanocomposites

In this section the electromechanical strain response of SWNT-PVDF nanocomposites is compared with that of SWNT-CP2 and SWNT-(β-CN) APB ODPA nanocomposites. Figure 5.25 shows the M_{3333} (AC, 1Hz) coefficient for all three polymer nanocomposite systems. At low SWNT vol% (Inset Figure 5.25) the M_{3333} coefficients for the PVDF and (β -CN) APB ODPA nanocomposites were comparable with each other and higher than those of CP2. At high SWNT content, The M_{3333} coefficients appear to have values higher than CP2 but lower than (β -CN) APB ODPA. Figure 5.26 depicts the M_{1133} (DC) as a function of SWNT content for the three nanocomposite systems. The M_{1133} coefficients for the SWNT-PVDF samples at low SWNT content is much lower than those for SWNT-CP2 and SWNT-(β-CN) APB ODPA. This finding can potentially be attributed to the use of equation 3.3. The critical assumption in the equation was the thin skin (thickness ~ 50nm) constraining layer of the polyimide system[91]. However, if the thickness of the constraining layer increases, there arises a need to use a two-beam model. The higher contrast in the densities of SWNTs and PVDF as compared to SWNTs and polyimides can result in a thick constraining layer. In light of this observations, M_{3333} coefficient is a more accurate representation of the electromechanical response.

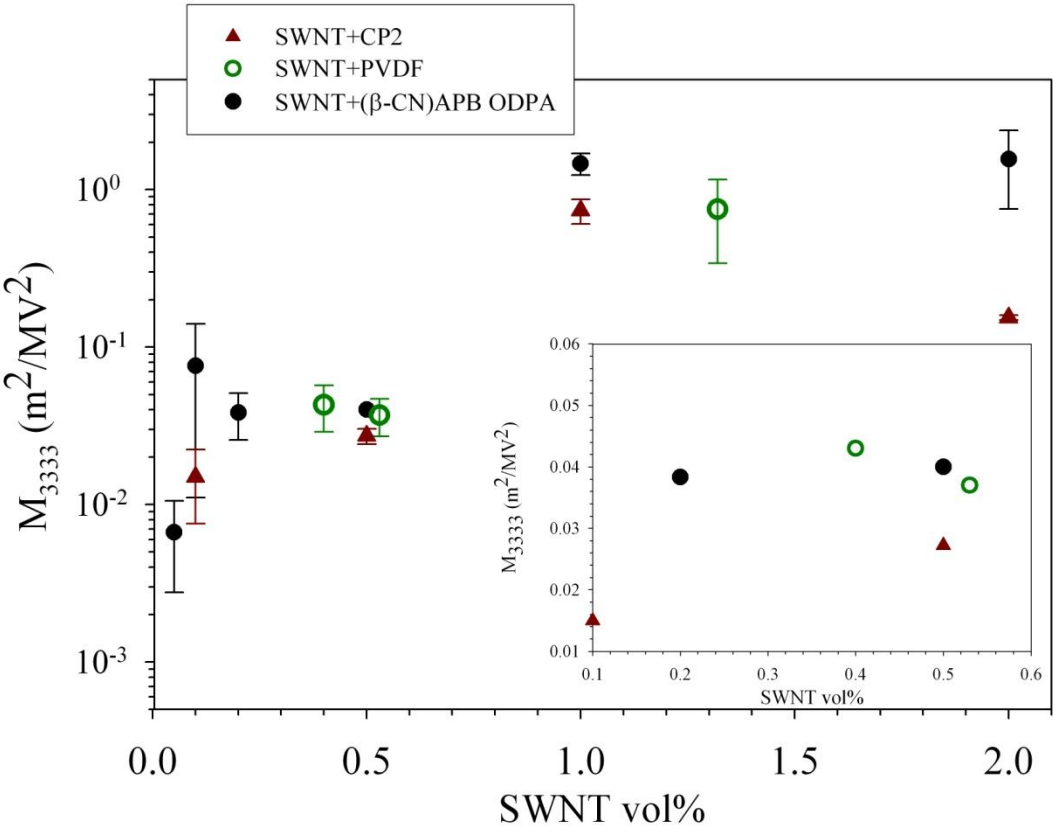

Figure 5.25 M_{3333} (1 Hz AC) vs SWNT vol% comparison between SWNT-PVDF, SWNT-CP2 and SWNT-(β-CN) APB ODPA nanocomposites.

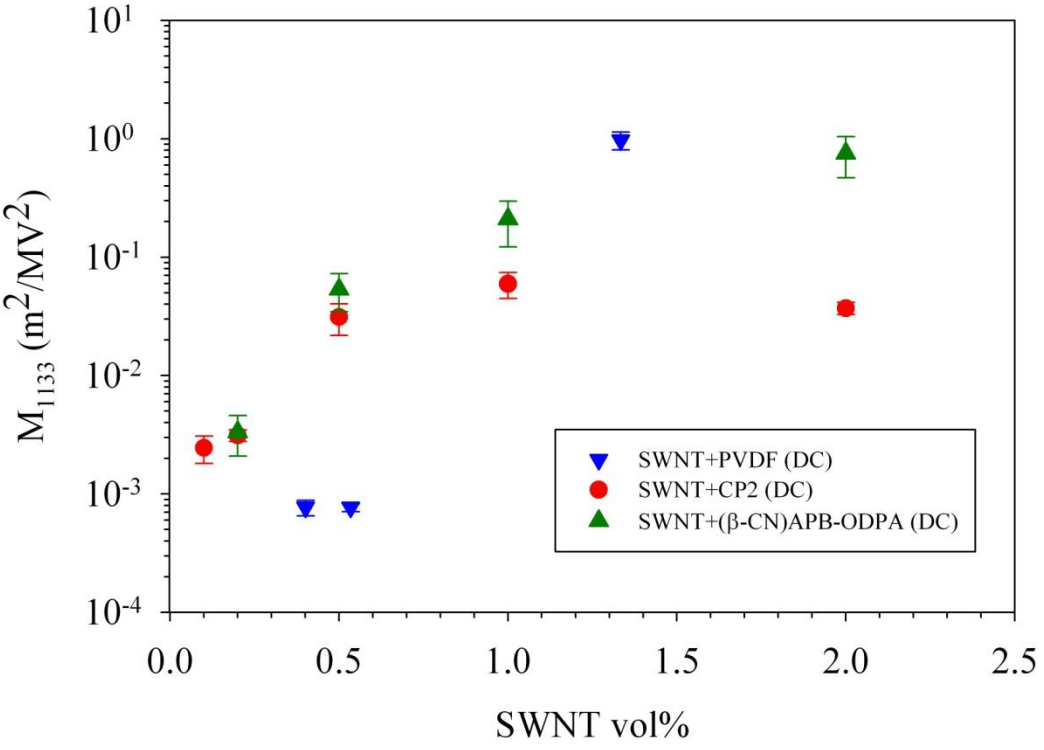

Figure 5.26 M_{1133} (DC) vs SWNT vol% comparison between SWNT-PVDF, SWNT-CP2 and SWNT-(β CN) APB ODPA nanocomposites.

The thickness electrostrictive response of SWNT-PVDF nanocomposites is comparable to that of SWNT-(β-CN) APB ODPA samples but higher than that SWNT-CP2 nanocomposites (Figure 5.25). Figure 5.27 shows the dielectric constant of PVDF nanocomposites compared with that of CP2 and (β-CN) APB ODPA nanocomposites. The dielectric constant values are comparable for all three nanocomposite systems. The comparable dielectric constant values do not explain the higher electrostrictive response in the polar (β-CN) APB ODPA and PVDF nanocomposites as compared to the CP2 samples.

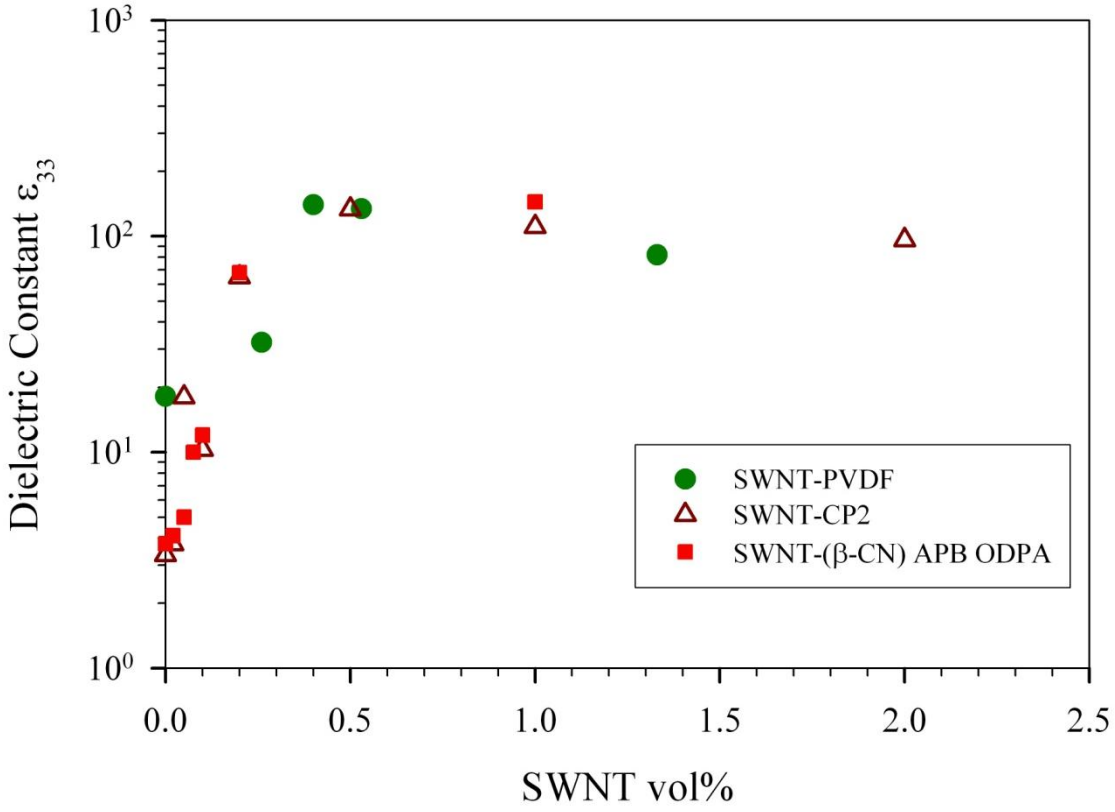

Figure 5.27 Dielectric constant comparison for SWNT-CP2, SWNT-(β-CN) APB ODPA and SWNT-PVDF.

The higher electrostrictive response can then be explained by higher dipole moment and SWNT-polymer interactions as was indicated in Section 4. Results presented in this section also reinforce this hypothesis.

PVDF shows the highest polarization amongst all three polymers discussed in this study. PVDF (β phase) can show a remnant polarization of 50 – 100 mC/m^2 as compared to 40 mC/m^2 of (β-CN) APB ODPA and also shows a non-covalent interaction with SWNTs. However the improvements in the electrostrictive response in the SWNT-PVDF nanocomposites is marginal. This can be attributed to:

a) Possible effects of a higher percolation threshold (~0.3 vol%) in the SWNT-PVDF nanocomposites as compared to the SWNT-polyimide systems (~0.05 vol%) and,

b) γ phase can show a maximum spontaneous polarization of only around 12 mC/m^2 (assuming 50% crystallinity) which is much lower than the polarization of 65 mC/m^2 shown by the β phase[114, 129].

Given these possible explanations, one potential technique to improve the electrostrictive response of SWNT-PVDF nanocomposites is to stretch these nanocomposites. Stretching the nanocomposites provides two advantages:

i) Stretching has been shown to transform the γ phase to β phase[132]. The β phase can show a spontaneous polarization of about 65 mC/m^2 (assuming 50% crystallinity)[114] that is much higher than the γ phase and

ii) Stretching the SWNT-PVDF nanocomposites can also decrease the conductive losses and contributions of Joule heating to the electromechanical response by disrupting the percolation structure of SWNTs through the thickness (direction of applied field).

The following section investigates the effect of stretching on the microstructure, electrical conductivity, dielectric constant and the thickness actuation response of the stretched SWNT-PVDF nanocomposites.

5.7 Characterization of stretched PVDF and SWNT-PVDF nanocomposites

The PVDF and SWNT-PVDF samples subject to the stretch ratio of 4:1 (using a Instron MTS tensile test machine) are characterized using FTIR, WAXs and DSC to evaluate and quantify the presence of β phase in the samples. Figure 5.28 indicates the direction of the stretch in the center of the necking region of the stretched samples.

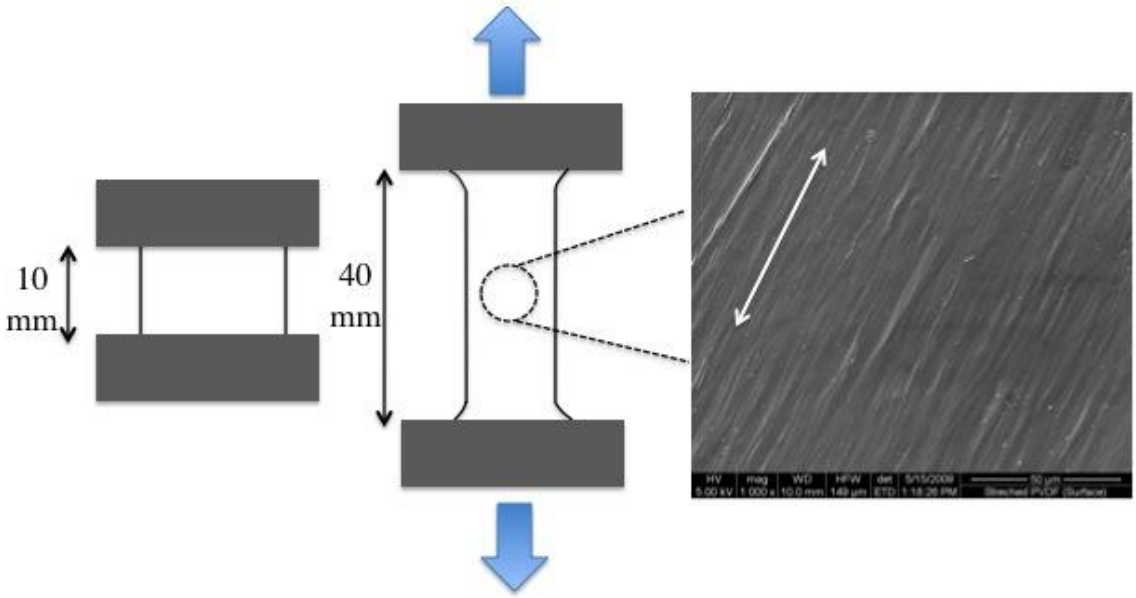

Figure 5.28 Stretch orientation of PVDF film.

5.7.1 Microstructure and polarization characterization

Figure 5.29(a) shows the FTIR-ATR spectrum of stretched PVDF and SWNT-PVDF nanocomposites. Stretched pure PVDF shows distinct β peaks at 509 cm^{-1}, 840 cm^{-1} and 1275 cm^{-1} along with the α peak at 766 cm^{-1}. Stretched SWNT-PVDF samples also show the β peaks along with a shoulder at 1233 cm^{-1} indicating presence of some γ phase but no α peaks. This is further clarified in Figure 5.29(b) that compares the 1.33 vol% SWNT sample before and after stretching. β peaks at 840 cm^{-1} and 1275 cm^{-1} in the stretched sample replace the γ peaks at 812 cm^{-1} and 834 cm^{-1} observed in the unstretched sample. However as mentioned previously the 1233 cm^{-1} γ peak appears as a shoulder in the stretched sample.

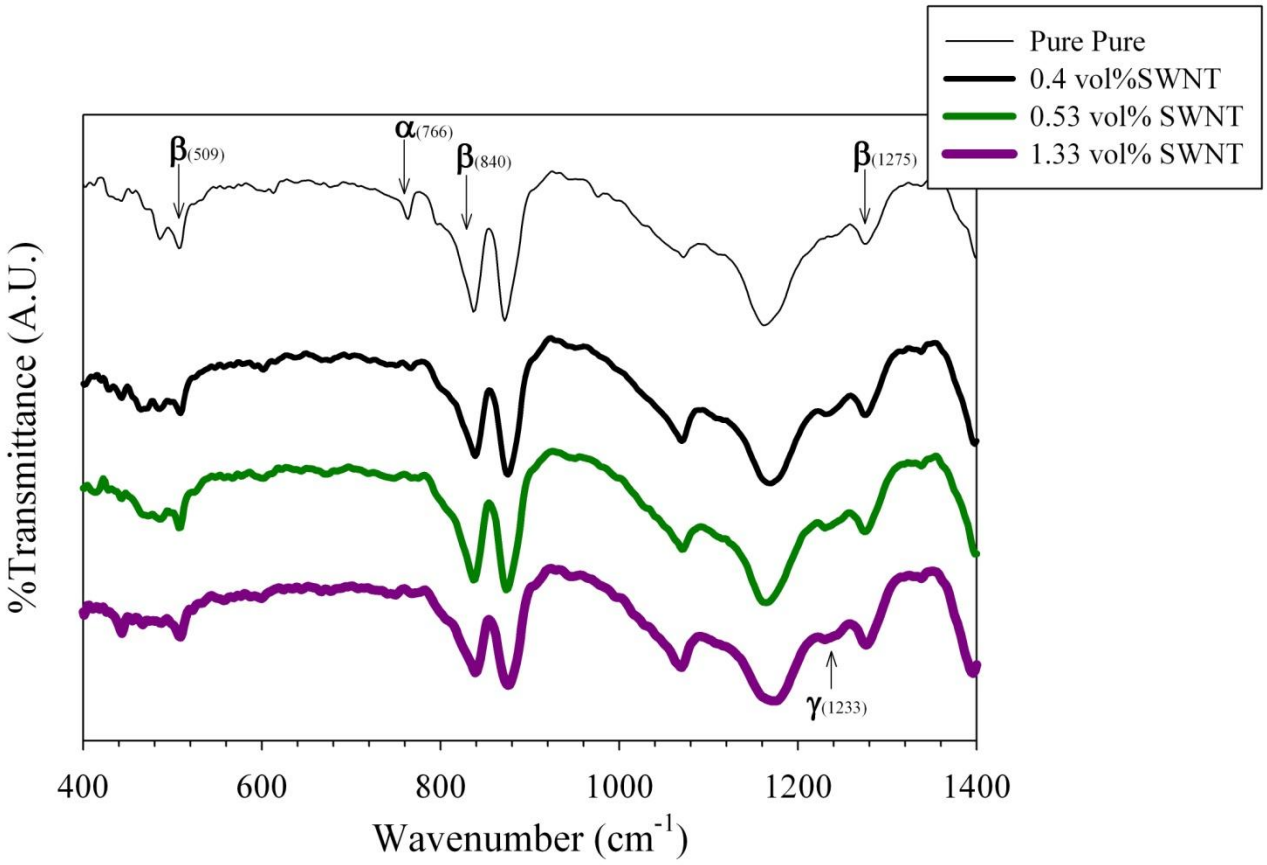

(a)

Figure 5.29 (a) FTIR-ATR spectrum for stretched PVDF and SWNT-PVDF nanocomposites, (b) FTIR-ATR showing transformation of γ to β phase in 1.33 vol%SWNT PVDF.

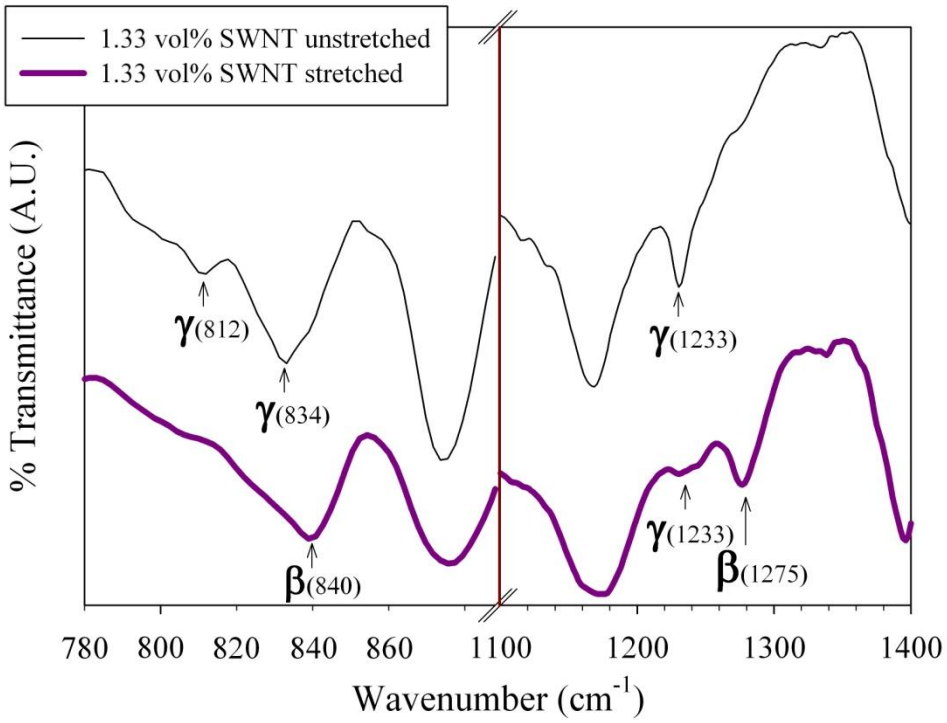

(b)

Figure 5.29 Continued.

The WAXs spectrum of the stretched samples (Figure 5.30) distinctly shows the 2θ β phase peaks at 20.7° and 36.5° in the pure PVDF and SWNT-PVDF nanocomposites. The pure PVDF also shows a shoulder at 18.6° that can be attributed to the α phase[119]. However the WAXs method is not sensitive enough to resolve the small γ phase present in the stretched SWNT-PVDF samples.

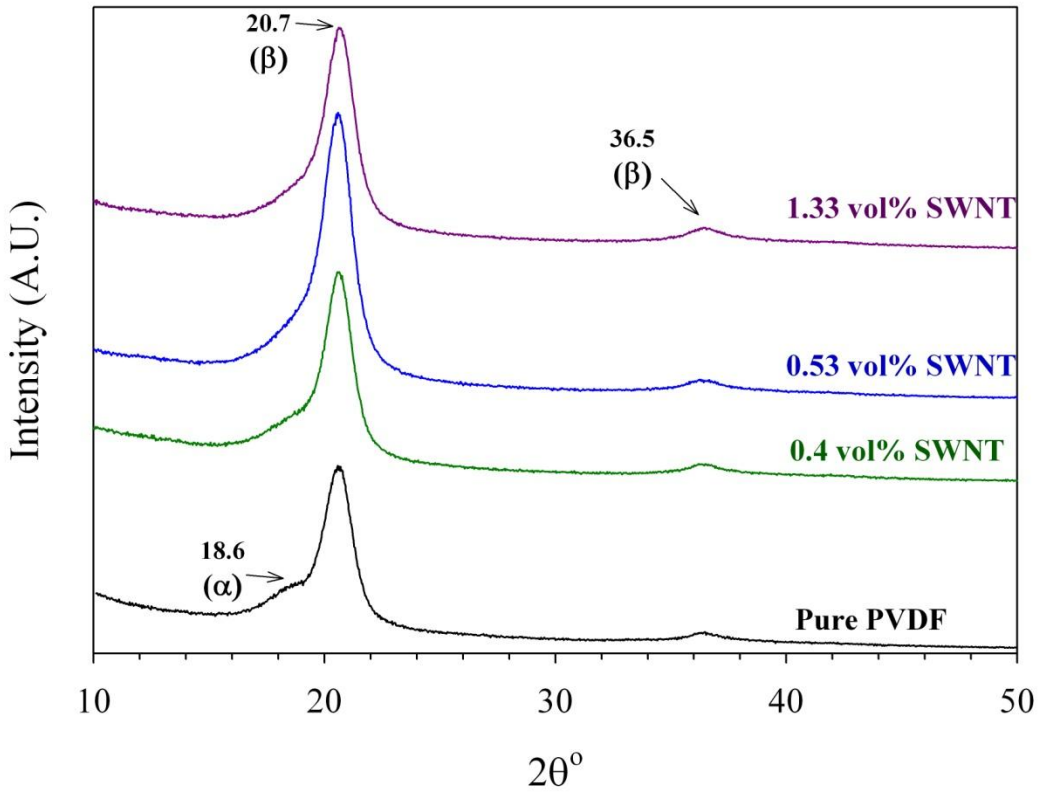

Figure 5.30 WAXs spectrum of unstretched PVDF and SWNT-PVDF nanocomposites.

Figures 5.31(a) and (b) show the DSC melting and crystallization peaks of pure PVDF and SWNT-PVDF nanocomposites. The melting temperature of the stretched samples is at 163 °C and remains largely unchanged and is attributed to the melting of β phase. In general the crystallization temperatures show an increase with SWNT content as was observed in the unstretched samples indicating that SWNTs act as nucleating agents. A marginal increase in the crystallinity is also observed with increase in SWNT content as is listed in Table 5.4.

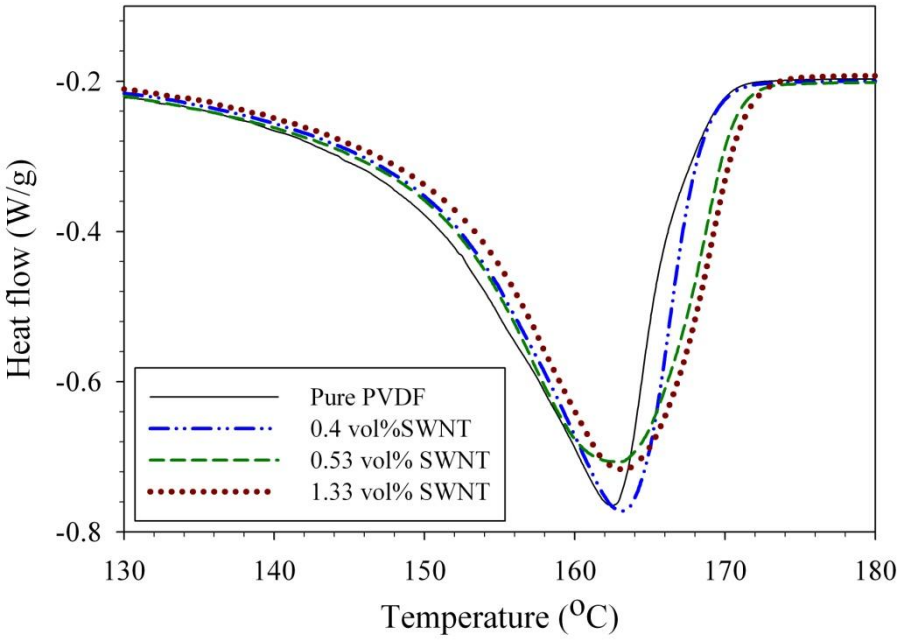

(a)

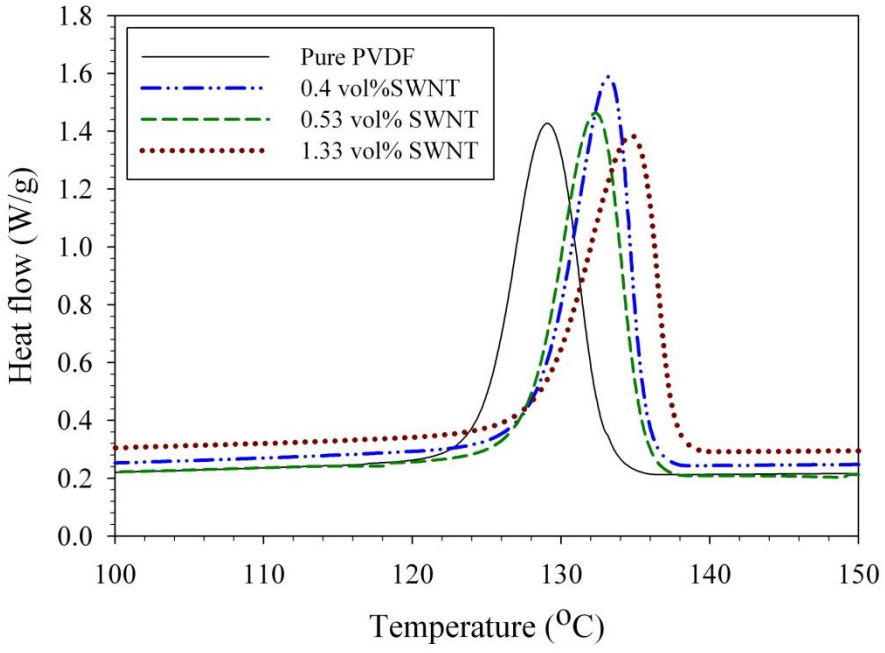

(b)

Figure 5.31 (a) DSC melting peaks for stretched PVDF and SWNT-PVDF nanocomposites and, (b) DSC crystallization peaks for stretched PVDF and SWNT-PVDF nanocomposites.

Table 5.4. DSC results of stretched SWNT-PVDF nanocomposites.

SWNT vol%	Melting Temperature (°C)	%Crystallinity	Crystallization Temperature (°C)
0	162	49	129
0.4	163	51	133
0.53	162	53	132
1.33	163	53	135

Stretched PVDF has a combination of β and α phases while stretched SWNT-PVDF have a combination of β and γ. Hence for comparison we need to quantify the amount of β phase present as a function of SWNT content in PVDF. Employing the Lambert-Beer law and using the absorbance (A_β) from transmission spectrum of the stretched samples we compute the β phase crystallinity (X_β) as:

$$X_\beta = \frac{A_\beta}{K_\beta C L} \tag{5.4}$$

where K_β (7.7 x 10^4 cm^2/mol[127]) is the absorbtion coefficient at 840 cm^{-1}, C is derived using the density of β phase (1.97 g/cm^3 [128]) as 0.0307 mol/cm^3 and L is the thickness of the samples. Figure 5.32(a) shows the transmission absorption spectrum at 840 cm^{-1} normalized by the thickness of the samples. The X_β of the stretched samples computed from equation 5.4 are plotted as a function of SWNT content in Figure 5.32(b). An increase in the X_β is seen in the SWNT content samples and plateaus off at higher SWNT content. A marked increase in X_β is seen between the stretched pure PVDF and the SWNT-PVDF nanocomposites. This can largely be attributed to the fact that γ phase is easily transformed to β phase by deformation[133, 134]. This is potentially due to very close chain conformation of γ (T_3GT_3G') phase than the α (TGTG') phase to the β (TTTT) phase. This close chain conformation would ensure more effective phase transformation in the predominantly γ phase SWNT-PVDF nanocomposites than pure PVDF. The increase in the β phase between 0.4 vol% SWNT to 0.53 vol % SWNT

stretched SWNT-PVDF nanocomposites seen in Figure 5.30(b) can be attributed to increase in crystallinity as seen in table 5.4.

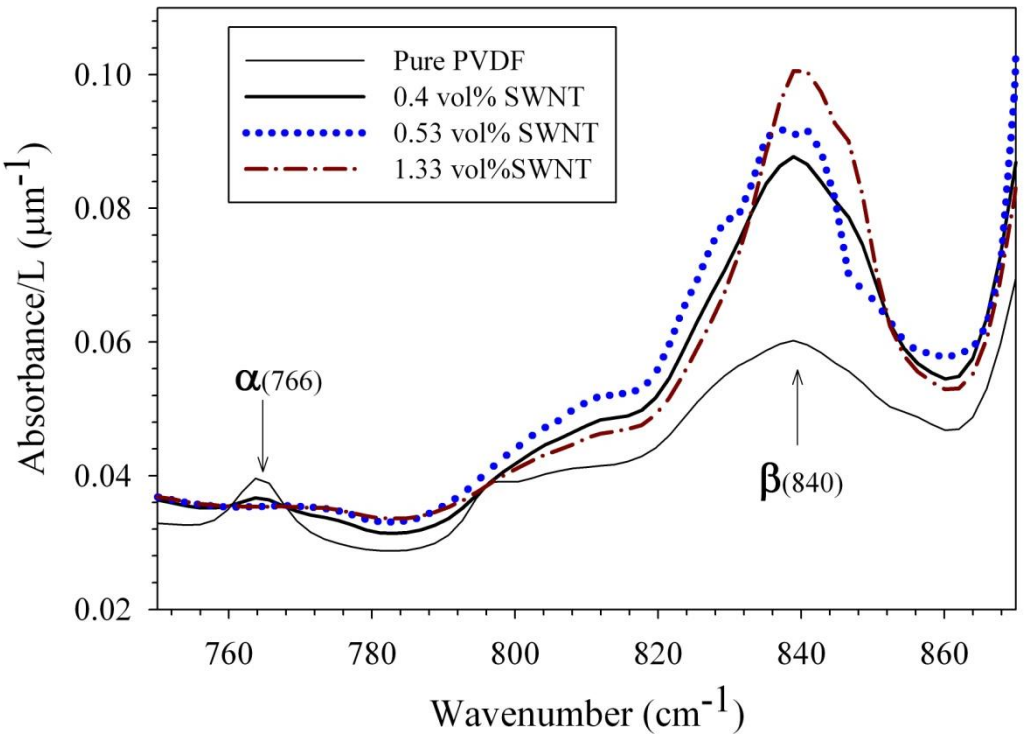

(a)

Figure 5.32 (a) FTIR-Transmission spectrum for 840 cm^{-1} β peak for PVDF and SWNT-PVDF nanocomposites, (b) β crystallinity computed from Lambert – Beer law as a function of SWNT vol%.

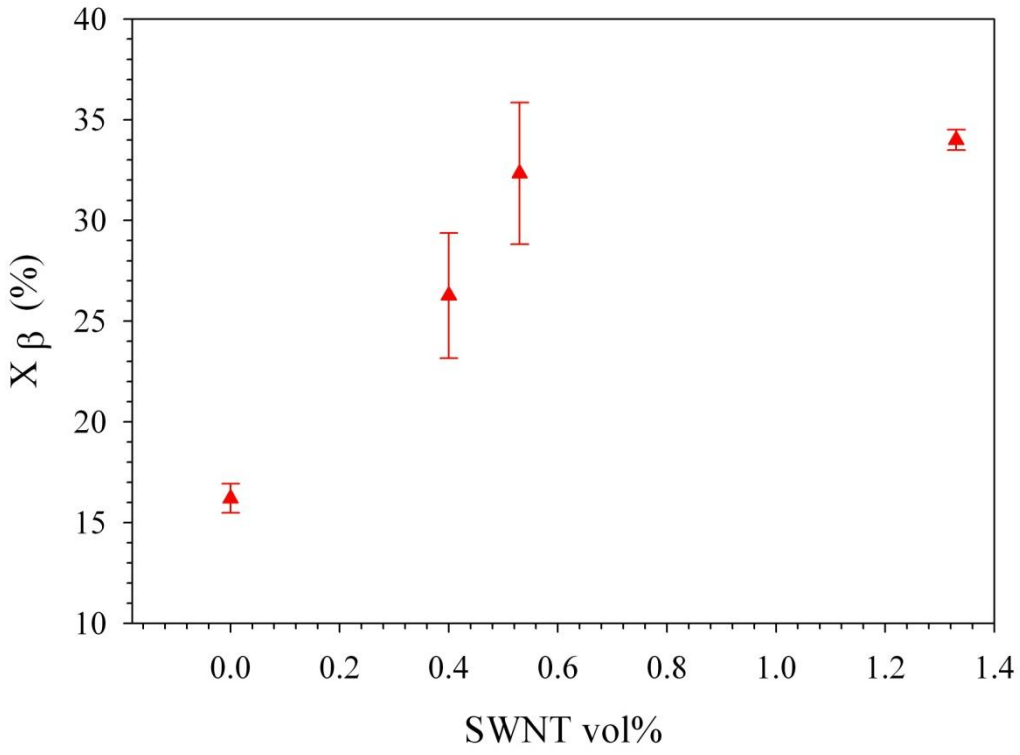

(b)

Figure 5.32 Continued.

The X_α computed for the pure stretched PVDF using the 766 cm^{-1} peak is about 0.1 (10%). Considering that the X_β computed from Lambert – Beer law is about 0.16 (16%) the result however does not agree with the total crystallinity measured using DSC. This suggests a limitation in computing the X_β using this method as it potentially under-predicts the X_β. Since the K_β derived by Gregorio et al[128] is for a solution cast film, this discrepancy could potentially be a result of the need to update K_β for β phase in stretched PVDF films. Also the presence of γ phase in the stretched nanocomposites cannot be quantified by this method currently as the K_γ derived is for the 510 cm^{-1} peak which is common to both γ and β phases. Computing the relative β crystallinity F(β) as done by various studies [135, 136] is also not a reliable option as the total percentage crystallinity in the stretched nanocomposites changes with SWNT content and hence cannot give an accurate comparison of the quantity of β phase present in the samples.

The Lamber-Beer law method provides a quantitative method to compare the presence of β phase but has a shortcoming for stretched films as it under-predicts X_β.

The spontaneous polarization in β phase crystals is 130 mC/m^2, which is greater than that of γ crystals by almost a factor of 5. From the β crystallinity increase with SWNT content depicted in Figure 5.32, it is clear that the stretched SWNT-PVDF nanocomposites reaches a much higher level of polarization compared to the unstretched nanocomposites given the similar levels of total crystallinity in the unstretched and stretched samples.

5.7.2 Electrical conductivity and dielectric constant

Joule heating is an electrical conductivity dependent phenomenon. Figure 5.33 shows the comparison of conductivity in the SWNT-polymer nanocomposites before and after stretching for 0.53 vol% and 1.33 vol% SWNT nanocomposites. The behavior of the 0.53 vol% SWNT samples changes from conductive (conductivity constant with frequency) to dielectric (conductivity increasing with frequency) while the conductivity of 1.33 vol% SWNT samples decreases by 2 to 3 orders of magnitude. This result suggests that stretching the SWNT-PVDF nanocomposites decreases the conductive losses and Joule heating contributions, as a result of disruption in the SWNT network.

Figure 5.34 compares the dielectric constant of the SWNT-polymer nanocomposites before and after stretching for 0.53 vol% and 1.33 vol% SWNT nanocomposites. A sharp decrease is seen in the dileectric constant for the nanocomposites after stretching. This can also be attributed to the disruption of the SWNT network as was also evident from the decrease in the conductivity seen in Figure 5.33 resulting in decreased interfacial and induced polarization.

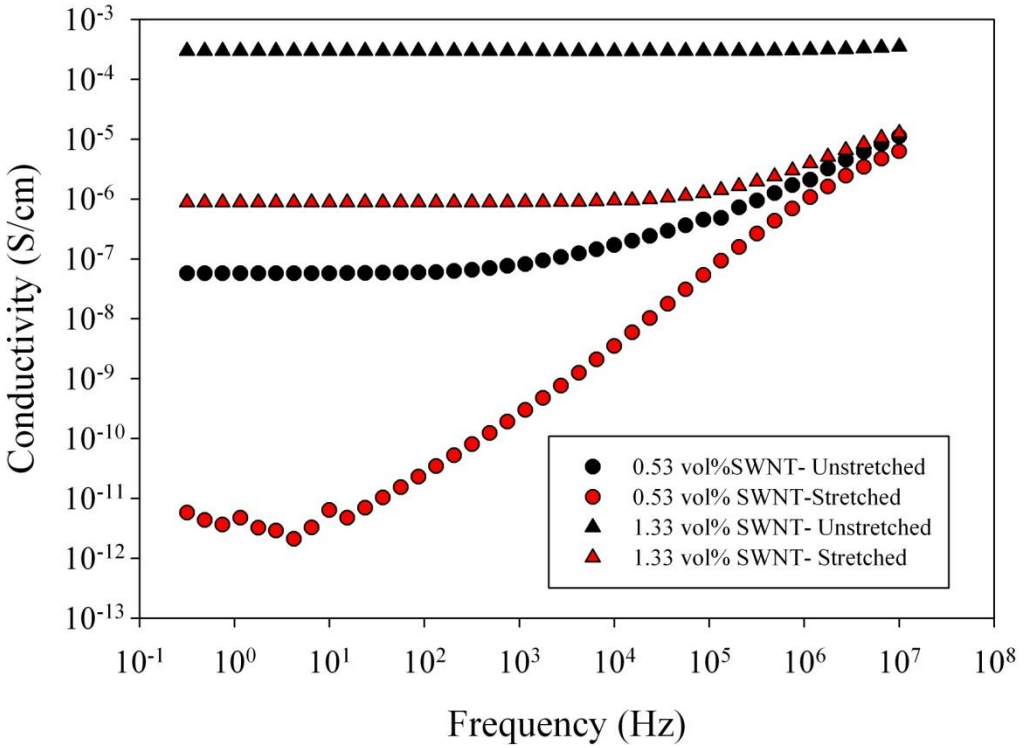

Figure 5.33 Electrical conductivity comparison for stretched and unstretched SWNT-PVDF nanocomposites.

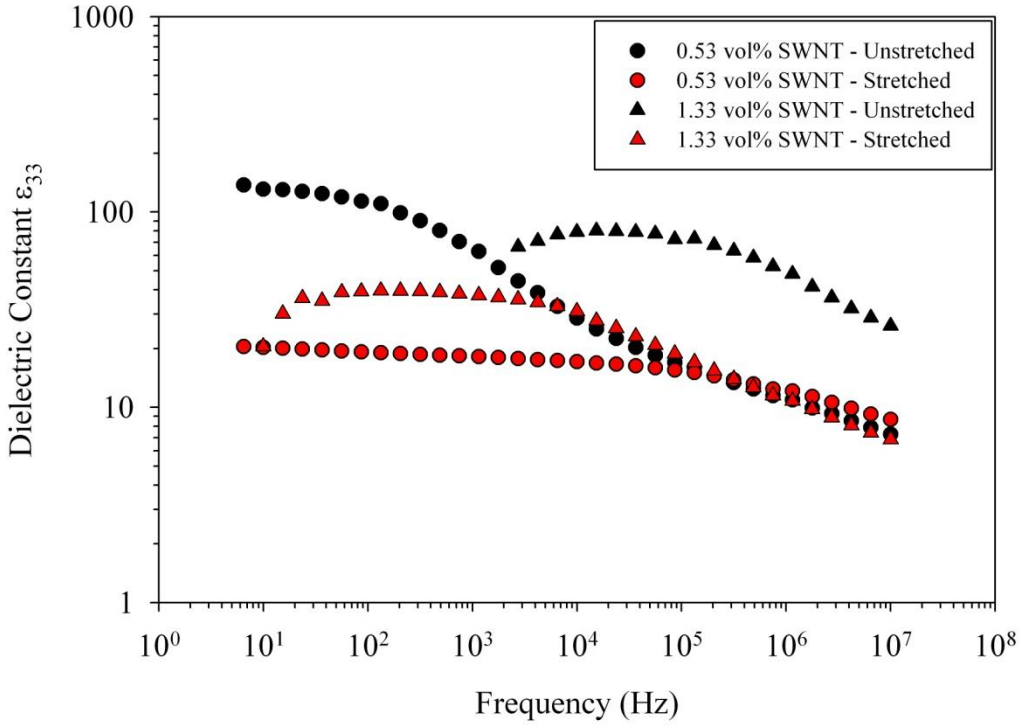

Figure 5.34 Dielectric constant comparison for stretched and unstretched SWNT-PVDF nanocomposites.

5.7.3 Thickness actuation

Figure 5.35 shows the transverse strain response of the stretched 1.33 vol% SWNT-PVDF samples compared with that of the unstretched samples. Lower SWNT concentration stretched sampled did not show any measurable actuation response. From Figure 5.35 (a) it can be seen that higher actuation electric field can be applied to the stretched nanocomposite samples which in turn is due to decrease in the electrical conductive losses. Figure 5.35 (b) compares the coefficient of electrostriction before and after stretching the nanocomposite samples. A sharp decrease is observed in the electrostrictive coefficient after stretching the samples. The decrease in the electrostrictive response after stretching indicates that the disruption of the SWNT network reflected in the decreased conductivity and dielectric constant values (Figures 5.33 and 5.34) is more critical than the increase in crystalline microstructure polarization. The homogenous dispersion of SWNTs in the polymer is essential for

enhanced interfacial polarization and also to take advantage of the polar microstructure via enhanced local electric fields. Thus stretching the nanocomposite samples does increase the polarization from the microstructure and decreases the conductive losses and Joule heating contributions, but it also leads to disruption of the SWNT network and decrease in the dielectric constant, resulting in a reduction in the electrostrictive response.

In this section we have documented the electrostrictive strain response of SWNT-PVDF nanocomposites. The contributions to the electrostrictive response from SWNTs, polar PVDF microstructure and SWNT-PVDF interactions are investigated. An increase in the interfacial polarization and dipolar polarization resulting from polar microstructure was observed with the SWNT content. The Joule heating contributions were also quantified at high SWNT content samples. The SWNT-PVF samples were also stretched to study the effect of increased microstructure polarization on the electrostrictive effect. It was found however that any contributions from the formation of the β crystalline phase were overshadowed by the disruption of the SWNT network.

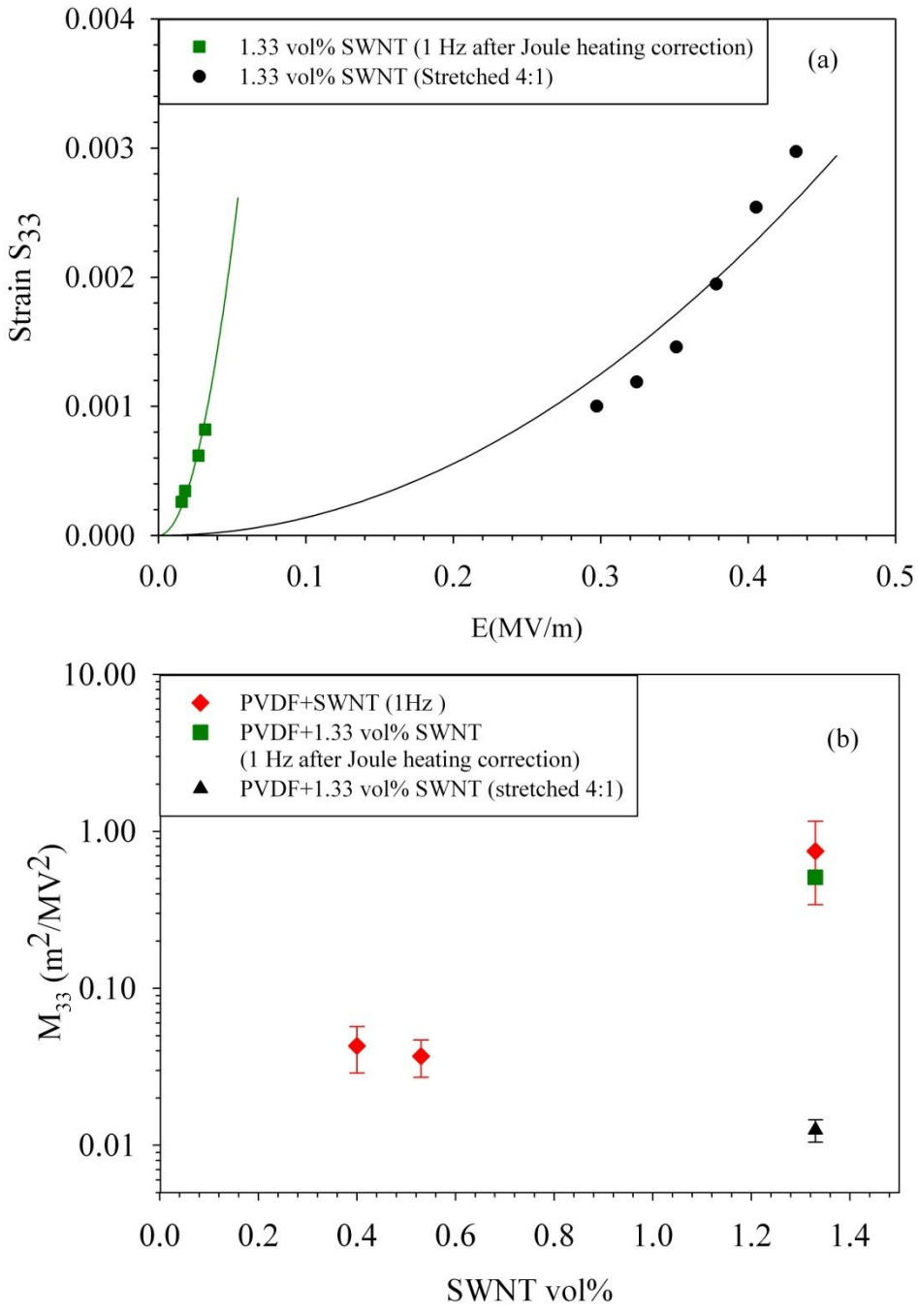

Figure 5.35 (a) Comparison of thickness strain response of unstretched and stretched 1.33 vol% SWNT+PVDF nanocomposites, (b) M_{33} comparison before and after stretching for 1.33 vol% SWNT+PVDF samples.

6. CONCLUSIONS AND FUTURE WORK

Single walled carbon nanotubes (SWNTs)-based polymer nanocomposites have been studied extensively for enhanced mechanical, electrical and even thermal properties. Open literature however shows limited investigations into the electromechanical response of SWNT-polymer nanocomposites. This research work has targeted a thorough investigation of the electromechanical response of SWNT- polymer nanocomposites and its dependence on SWNT content, polymer matrix and SWNT-polymer interaction. Towards that end, the focus is on three polymer matrices: a non-polar amorphous polyimide, CP2; a polar and weakly piezoelectric amorphous polyimide, (β-CN) APB ODPA; and a polar and piezoelectric smicrystalline polymer, PVDF.

In Section 3 we demonstrated the emergence of an electromechanical response in the non-electroactive, non-polar polyimide, CP2, in the presence of SWNTs. Transverse and longitudinal strains are measured as a function of DC and AC electric fields and SWNT content. The strains demonstrated a quadratic dependence on the applied electric field. The electromechanical response was observed at as low an electric field as 0.01 MV/m for 1vol% SWNT nanocomposites. The quadratic electromechanical coefficient was calculated and its dependence on SWNT content and applied electric field frequency was mapped. Using Raman spectroscopy, the contribution of SWNTs to the electromechanical strain response was determined to be negligeable. Maxwell's stress and Joule heating contributions to the strains were also determined to be minimal, indicating that electrostriction is the dominant mechanism driving the quadratic electromechanical response. Thermally stimulated current measurements (TSC) and dielectric relaxation spectroscopy experiments demonstrate enhanced induced polarization in the SWNT-CP2 nanocomposites in the presence of SWNTs. The enhanced induced polarization causes the electrostrictive response. The polarization is thought to result from three causes:

a) Interfacial polarization and
b) Augmentation in the total capacitance due to presence of micro/nanocapacitors
c) Increase in orientation polarization due to high local electric field resulting from SWNTs acting as extension of electrodes.

Previous studies in the open literature have shown enhanced electromechanical response in electroactive polymers in the presence of carbon nanotubes. In the present study, results in Section 3 show that an electromechanical response can be created in a non-electroactive polymer, namely CP2, in the presence of SWNTs; furthermore, this response can be tailored by choosing the SWNT content. A transverse electrostrictive coefficient of 0.74 m^2/MV^2 is measured, which is about seven orders of magnitude higher than known electrostrictive polymers like P(VDF-TrFE). Just as importantly, the electric field driving this actuation response is as low as 0.01 – 0.15 MV/m, about $1/100^{th}$ of that required to drive known electrostrictive polymers like polyurethane and P(VDF-TrFE).

The effect of the polymer matrix on the electrostrictive response is evaluated in Section 4. Electrostrictive response of a polar polyimide, (β-CN) APB ODPA, in the presence of SWNTs is quantified. (β-CN) APB ODPA has a relatively high dipole moment and also exhibits a noncovalent electron donor-acceptor relationship with SWNTs. The SWNT-(β-CN) APB ODPA nanocomposites are found to have higher electrostrictive strain response, higher electrostrictive material coefficient and higher strain rate than SWNT-CP2 nanocomposites. Thermally stimulated current measurements and dielectric relaxation experiments reveal a higher polarization in the SWNT-(β-CN) APB ODPA system than SWNT-CP2 one. The difference is attributed to the high dipole moment and SWNT-(β-CN) APB ODPA affinity. The effect of electric field frequency on the electromechanical response is also studied and the response is found to decrease with frequency, consistent with a dipole-driven actuation. The results in this section show that, along with the SWNT content, the electrostrictive response in SWNT-polymer nanocomposites can also be tailored by the choice of the polymer matrix. The electrostrictive response can be optimized by the choice of a

polymer that displays a high dipole moment and a strong interaction with the SWNTs, such as through a noncovalent donor-acceptor interaction. The electromechanical strain response for both polyimide-based nanocomposite systems showed the following salient features:

(i) The actuation electric fields required are orders of magnitude lower than those needed for other electroactive polymers (EAPs).

(ii) Electrostrictive coefficients that are four to seven orders of magnitude higher than those of known electroactive polymers.

(iii) Comparable gravimetric work densities to those of known EAPs.

Based on the observations of Sections 3 and 4, PVDF is selected as a polymer matrix to study the electromechanical response of SWNT-based nanocomposites. PVDF is a polar polymer with a higher polarization than both CP2 and (β-CN) APB ODPA when in the β phase. PVDF also demonstrates a non-covalent electron donor-acceptor relationship with the SWNTs. Like in the SWNT-polyimide nanocomposites, SWNT actuation and Maxwell's stress show no significant contributions to the observed quadratic electromechanical response. Since PVDF is a semicrystalline polymer, the polarization contributions from the crystalline and amorphous regions need to be quantified to fully evaluate the electrostrictive response of SWNT-PVDF nanocomposites. Fourier transform infrared spectroscopy (FTIR), wide angle X ray scattering (WAXs) and differential scanning calorimetry (DSC) are used to detect and quantify the polarization resulting from formation of the polar γ phase in PVDF due to presence of SWNTs. An increase is seen in the polar γ phase with SWNT content, resulting in an increase in the spontaneous polarization in PVDF. Dielectric relaxation spectroscopy also shows enhanced dipolar contributions from the amorphous regions of PVDF with SWNT content. Due to the low glass transition temperature of PVDF (T_g=-36 °C), the Joule heating contributions to the electrostrictive strains are also quantified. Small contributions are detected in the quadratic electromechanical strains due to Joule heating in high SWNT content samples. The coefficient of electrostriction is then calculated for high SWNT content samples based on these observations. Like in the case

of SWNT-polyimide nanocomposites, the SWNT-PVDF nanocomposites also show a low electric field (order of 10^{-2} MV/m) driven actuation response and two to seven orders of magnitude higher electrostrictive coefficient than known electroactive polymers. The electrostrictive response of SWNT-PVDF nanocomposites are compared with those of SWNT-CP2 and SWNT-(β-CN) APB ODPA samples. It is determined that the response of SWNT-PVDF samples is comparable with that of SWNT-(β-CN) APB ODPA samples and higher than that of SWNT-CP2 samples. The higher percolation threshold and lower polarization of γ crystalline phase (as compared to β phase) limit further improvement in the electrostrictive response.

The SWNT-PVDF samples are then stretched to convert the polar γ phase to the more polar β phase in an effort to evaluate the comparative importance of SWNT network and the polar microstructure. It was observed that the conductivity of the SWNT-PVDF nanocomposites decreases indicating that strain contributions from Joule heating also decrease. However stretching the nanocomposites also results in a decrease in the dielectric constant due to disruption of the SWNT network. As a result, a sharp decrease is observed in the electrostrictive response of the stretched nanocomposites in spite of the increase in polarization contributions from the polar microstructure. This is attributed to the need for a well-dispersed SWNT network to interact with the dipoles and augment the effective dielectric constant.

Suggestions for future work targeted at improving the electrostrictive response of SWNT based nanocomposites include:

a) Electrostrictive response in SWNT-polyimide nanocomposites: To improve the non-covalent interaction in SWNT-polyimide systems, which is a key to enhanced electrostrictive response, other polyimides like (4-CN) APB ODPA should be evaluated since they have the potential to exhibit even stronger affinity to SWNTs and more dipoles.

b) Enhanced electrostrictive response in SWNT-PVDF system: The higher percolation threshold in SWNT-PVDF nanocomposites is most likely due to dispersion. Lower percolation threshold may be a key in improving the electrostrictive response by

improving dispersion; therefore other co-solvents and use of coupling agents should be explored. Investigating enhanced piezoelectric properties of stretched SWNT-PVDF nanocomposites: this research has demonstrated an increase in the piezoelectric β phase in stretched PVDF due to the presence of SWNTs. Attempts at poling the unstretched SWNT-PVDF nanocomposites have been largely unsuccessful due to the high conductivity of the SWNT-PVDF nanocomposites. However, we have demonstrated a decrease in conductivity in stretched SWNT-PVDF nanocomposites as a result of breaking the 3D SWNT network. It follows that poling of the stretched nanocomposites should be possible. Once poled, the stretched SWNT-PVDF composites could potentially show evidence of a piezoelectric response.

REFERENCES

(1) Levi, N.; Czerw, R.; Xing, S.; Iyer, P.; Carroll, D. L. *Nano Letters* **2004,** *4*, (7), 1267-1271.

(2) Kang, J. H.; Park, C.; Gail, S. J.; Lowther, S. E.; Harrison, J. S. *NANO: Brief Reports and Reviews* **2006,** *1*, (1), 77-85.

(3) Kim, G. H.; Hong, S. M. *Molecular Crystals and Liquid Crystals* **2007,** *472*, 161-169.

(4) Manna, S.; Nandi, A. K. *Journal of Physical Chemistry C* **2007,** *111*, 14670-14680.

(5) Mago, G.; Kalyon, D. M.; Fisher, F. T. *Journal of Nanomaterials* **2008,** *2008*, 1-8.

(6) Zhang, S.; Zhang, N.; Huang, C.; Ren, K.; Zhang, Q. *Advanced Materials* **2005,** *17*, 1897-1901.

(7) Wikipedia, Types of Carbon Nanotubes, http://en.wikipedia.org/wiki/Image:Types_of_Carbon_Nanotubes.png, June 2006.

(8) Chem.tue.nl, MWNT, http://students.chem.tue.nl/ifp03/images/mwnt.gif, June 2006

(9) Endo, M.; Iijima, S.; Dresselhaus, M. S., *Carbon Nanotubes*. Elsevier Science Limited: New York, 1991.

(10) Zheng, L. X.; O'Connell, M. J.; Doorn, S. K.; Liao, X. Z.; Zhao, Y. H.; Akhadov, E. A.; Hoffbauer, M. A.; Roop, B. J.; Jia, Q. X.; Dye, R. C.; Peterson, D. E.; Huang, S. M.; Liu, J.; Zhu, Y. T. *Nature Letters* **2004,** *3*, 673-676.

(11) Treacy, M. M. J.; Ebbesen, T. W.; Gibson, J. M. *Nature* **1996,** *381*, 678-680.

(12) Li, F.; Cheng, M.; Bai, S.; Su, G.; Dresselhaus, M. S. *Applied Physics Letters* **2000,** *77*, (20), 3161-3163.

(13) Yu, M.-F.; Files, B. S.; Arepalli, S.; Ruoff, R. S. *Physical Review Letters* **2000,** *84*, (24), 5552-5555.

(14) Lu, J. P. *Journal of Physics and Chemistry of Solids* **1997,** *58*, 1649-1652.

(15) Zhou, G.; Duan, W. H.; Gu, B. L. *Chemical Physics Letters* **2001,** *333*, (5), 344-349.

(16) Wong, E. W.; Sheehan, P. E.; Lieber, C. M. *Science* **1997,** *277*, 1971-1975.

(17) Frank, S.; Poncharal, P.; Wang, Z. L.; de Heer, W. A. *Science* **1998,** *280*, 1744-1746.

(18) Sanvito, S.; Kwon, Y.-K.; Tománek, D.; Lambert, C. J. *Physical Review Letters* **2000,** *84*, (9), 1974-1977.

(19) Thess, A.; Lee, R.; Nikolaev, P.; Dai, H.; Petit, P.; Robert, J.; Xu, C.; Lee, Y. H.; Kim, S. G.; Rinzler, A. G.; Colbert, D. T.; Scuseria, G. E.; Tomanek, D.; Fischer, J. E.; Smalley, R. E. *Science* **1996,** *273*, 483-487.

(20) Hone, J.; Whitney, M.; Piskoti, C.; Zettl, A. *Physical Review B* **1999,** *59*, (4), R2514-R2516.

(21) Kim, P.; Lieber, C. M. *Science* **1999,** *286*, 2148-2150.

(22) Roth, S.; Baughman, R. H. *Current Applied Physics* **2002,** *2*, (4), 311-314.

(23) Baughman, R. H.; Cui, C.; Zakhidov, A. A.; Iqbal, Z.; Barisci, J. N.; Spinks, G. M.; Wallace, G. G.; Mazzoldi, A.; De Rossi, D.; Rinzler, A. G.; Jaschinski, O.; Roth, S.; Kertesz, M. *Science* **1999,** *284*, 1340-1344.

(24) El-Hami, K.; Matsushige, K. *Ultramicroscopy* **2005,** *105*, 143-147.

(25) Guo, W.; Guo, Y. *Physical Review Letters* **2003,** *91*, (11), 1-4.

(26) Andrews, R.; Jacques, D.; Minot, M.; Rantell, T. *Macromolecular Materials Engineering* **2002,** *287*, 395-403.

(27) Breuer, O.; Sundarajan, U. *Polymer Composites* **2004,** *25*, (6), 630-645.

(28) Ajayan, P. M.; Ebbesen, T. W. *Reports of Progress in Physics* **1997,** *60*, (10), 1025-1062.

(29) Moon, J. M.; An, K. H.; Lee, Y. H.; Park, Y. S.; Bae, D. J.; Park, G. S. *Journal of Applied Chemistry B* **2001,** *105*, (24), 5677-5681.

(30) Park, C.; Ounaies, Z.; Watson, K. A.; Crooks, R. E.; Smith, J. J.; Lowther, S. E.; Connell, J. W.; Siochi, E. J.; Harrison, J. S. *Chemical Physics Letters* **2002,** *364*, 303-308.

(31) Breuer, O.; Sundararaj, U. *Polymer Composites* **2004,** *25*, (6), 630-645.

(32) Kim, Y. K.; Lewis, A. F.; Patra, P. K.; Warner, S. B.; Calvert, P. *National Textile Center Research Briefs-Materials Competency* **2001**, *June*, 24-24.

(33) Mitchell, C. A.; Bahr, J. L.; Sivaram, A.; Tour, J. M.; Krishnamoorti, R. *Macromolecules* **2002,** *35*, (23), 8825-8830.

(34) Hirsch, A. *Angew. Chem. Int. Ed.* **2002,** *41*, (11), 1853-1859.

(35) Andrews, R.; Jacques, D.; Qian, D.; Rantell, T. *Accounts of Chemical Research* **2002,** *35*, 1008-1017.

(36) Biercuk, M. J.; Llaguno, M. C.; Radosavljevic, M.; Hyun, J. K.; Johnson, A. T.; Fischer, J. E. *Applied Physics Letters* **2002,** *80*, 2767.

(37) Qian, D.; Dickey, E. C.; Andrews, R.; Rantell, T. *Applied Physics Letters* **2000,** *76*, (20), 2868-2870.

(38) Vaia, R. A.; Wagner, H. D. *Materials Today* **2004,** *7*, (11), 32-37.

(39) Shaffer, M. S. P.; Windle, A. H. *Advanced Materials* **1999,** *11*, (11), 937-941.

(40) Gorga, R. E.; Cohen, R. E. *Journal of Polymer Science: Part B: Polymer Physics* **2004,** *42*, (14), 2690-2701.

(41) Meincke, O.; Kaempfer, D.; Weickmann, H.; Friedrich, C.; Vathauer, M.; Warth, H. *Polymer* **2004,** *45*, (3), 739-748.

(42) Liu, T. X.; Phang, I. Y.; Shen, L.; Chow, S. Y.; Zhang, W.-D. *Macromolecules* **2004,** *37*, (19), 7214-7222.

(43) Manchado, M. A. L.; Valentini, L.; Biagiotti, J.; Kenny, J. M. *Carbon* **2005,** *43*, (7), 1499-1505.

(44) Ramanathan, T.; Liu, H.; Brinson, L. C. *Journal of Polymer Science Part B: Polymer Physics* **2005,** *43*, 2269-2279.

(45) Miyagawa, H.; Drzal, L. T. *Polymer* **2004,** *45*, (15), 5163-5170.

(46) Hwang, G. L.; Shieh, Y. T.; Hwang, K. C. *Advanced Functional Materials* **2004,** *14*, (5), 487-491.

(47) Garg, A.; Sinnott, S. B. *Chemical Physics Letters* **1998,** *295*, 273-278.

(48) Santos, C. V.; Martinez-Hernandez, A. L.; Fisher, F. T.; Ruoff, R. S.; Castano, V. M. *Chemical Materials* **2003,** *15*, 4470-4475.

(49) Zhao, J.; Park, H.; Han, J.; Lu, J. P. *Journal of Physical Chemistry B* **2004,** *108*, 4227-4230.

(50) Chen, J.; Ramasubramaniam, R.; Xue, C.; Liu, H. *Advanced Functional Materials* **2006,** *16*, 114-119.

(51) Ounaies, Z.; Park, C.; Wise, K. E.; Siochi, E. J.; Harrison, J. S. *Composite Science and Technology* **2003,** *63*, 1637-1646.

(52) Wise, K. E.; Park, C.; Siochi, E. J.; Harrison, J. S. *Chemical Physics Letters* **2004,** *391*, 207-211.

(53) Bryning, M. B.; Islam, M. F.; Kikkawa, J. M.; Yodh, A. G. *Advanced Materials* **2005,** *17*, (9), 1186-1191.

(54) Martin, C. A.; Sandler, J. K. W.; Shaffer, M. S. P.; Schwarz, M. K.; Bauhofer, W.; Schulte, K.; Windle, A. H. *Composites Science and Technology* **2004,** *64*, (15), 1236-2309.

(55) Ramasubramaniam, R.; Chen, J.; Liu, H. *Applied Physics Letters* **2003,** *83*, (14), 2928-2930.

(56) Mierczynska, A.; Mayne-L'Hermite, M.; Boiteux, G. *Journal of Applied Polymer Science* **2007,** *105*, (1), 158-168.

(57) Schmidt, R. H.; Kinloch, I. A.; Burgess, A. N.; H., W. A. *Langmuir* **2007,** *23*, (10), 5707-5712.

(58) Blanchet, G. B.; Fincher, C. R.; Gao, F. *Applied Physics Letters* **2003,** *82*, 1290-1292.

(59) Bauhofer, W.; Kovacs, J. Z. *Composites Science and Technology* **2009,** *69*, 1486-1498.

(60) Wang, L.; Dang, Z.-M. *Applied Physics Letters* **2005,** *87*, (042903), 1-3.

(61) Pötschke, P.; Dudkin, S. M.; Alig, I. *Polymer* **2003,** *44*, (17), 5023-5030.

(62) Kim, B.; Lee, J.; Yu, I. *Journal of Applied Physics* **2003,** *94*, (10), 6724-6728.

(63) Kornbluh, R.; Pelrine, R.; Eckerle, J.; Joseph, J. *IEEE International Conference in Robotics and Automation* **1998,** *3*, 2147-2154.

(64) Zhang, Q. M.; Bharti, V.; Zhao, X. *Science* **1998,** *280*, 2101-2104.

(65) Madden, J. D. W.; Vandesteeg, N. A.; Anquetil, P. A.; Madden, P. G. A.; Takshi, A.; Pytel, R. Z.; Lafontaine, S. R.; Wieringa, P. A.; Hunter, I. W. *IEEE Journal of Oceanic Engineering* **2004,** *29*, (3), 706-728.

(66) Courty, S.; Mine, J.; Tajbakhsh, A. R.; Terentjev, E. M. *Europhysics Letters* **2003,** *64*, (5), 654-660.

(67) Lee, D. Y.; Park, I.-S.; Lee, M.-H.; Kim, K. J.; Heo, S. *Sensors and Actuators A: Physical* **2007,** *133*, 117-127.

(68) Akle, B. J.; Leo, D. J. *Journal of Intelligent Material Systems and Structures* **2008,** *00*, 1-11.

(69) Yu, S.; Zheng, W.; Yu, W.; Zhang, Y.; Jiang, Q.; Zhao, Z. *Macromolecules* **2009,** *42*, 8870-8874.

(70) Thess, A.; Lee, R.; Nikolaev, P.; Dai, H.; Petit, P.; Robert, J.; Xu, C.; Lee, Y. H.; Kim, S. G.; Rinzler, A. G.; Colbert, D. T.; Scuseria, G. E.; Tomanek, D.; Fischer, J. E.; Smalley, R. E. *Science* **1996,** *273*, 483-487.

(71) Guo, T.; Nikolaev, P.; Thess, A.; Colbert, D. T.; Smalley, R. E. *Chemical Physics Letters* **1995,** *243*, 49-54.

(72) Nikolaev, P.; Bronikowski, M. J.; Bradley, R. K.; Rohmund, F.; Colbert, D. T.; Smith, K. A.; Smalley, R. E. *Chemical Physics Letters* **1999,** *313*, 91-97.

(73) St Claire, A. K.; St Claire, T. L.; Slemp, W. S. 2nd international conference on polyimides: New York; Weber, W.; Gupta, M., Eds. Society of Plastics Engineers: 1987; 16.

(74) Simpson, J. O.; Ounaies, Z.; Fay, C. Materials Research Society Symposium 1997; CA; pp 53-55.

(75) Dillon, A. C.; Gennett, T.; Jones, K. M.; Allenman, J. L.; Parilla, A.; Heben, M. J. *Advanced Materials* **1999,** *11*, (16), 1354 - 1358.

(76) Chesnokov, S. A.; Nalimova, V. A.; Rinzler, A. G.; Smalley, R. E.; Fisher, J. E. *Physical Review Letters* **1999,** *82*, (2), 343-346.

(77) Ramamrutham, S.; Narayan, R., *Strength of Materials*. Dhanpat rai and sons: New Delhi, 1993.

(78) Sundar, V.; Newnham, R. E. *Ferroelectrics* **1992,** *135*, 431-446.

(79) Banda, S. Characterization of aligned carbon nanotube/polymer composites. Thesis, Virginia Commonwealth University, Richmond, VA, 2004.

(80) Wikipedia, Dielectric Spectroscopy, http://en.wikipedia.org/wiki/Dielectric_spectroscopy, June 2006

(81) Frohlick, H., Dipolar molecules in gases. In *Theory of Dielectrics*, 1st ed.; Oxford university press: Oxford, U.K., 1958; p 15.

(82) Ounaies, Z.; Young, J. A.; Harrison, J. S. *NASA/TM-1999-209359* **1999**.

(83) Bucci, C.; Fieschi, R.; Guidi, G. *Physical Review* **1966,** *148*, (2), 816-823.

(84) Teyssedre, G.; Mezghani, S.; Bernes, A.; Lacabanne, C., Thermally stimulated current of polymers. *Dielectric spectroscopy of polymeric materials*, Runt, J. P.; Fitzgerald, J. J., Eds. American Chemical Society: Washington, DC, 1997.

(85) Belana, J.; Mudarra, M.; Calaf, J.; Canadas, J. C.; Menendez, E. *IEEE Transaction on Electrical Insulation* **1993,** *28*, (287-293).

(86) Setaram, Thermally Stimulated Current Measurement, http://thermal-analysis.setaram.com/thermal-analysis/fiche_produit.aspx?id=114, June 2006

(87) Runt, J. P.; Fitzgerald, J. J., *Dielectric Spectroscopy of Polymeric Materials*. American Chemical Society: Washington DC, 1997; p 230.

(88) Sauer, B. B.; Avakian, P.; Starkweather, H. W. J.; Hsiao, B. S. *Macromolecules* **1990,** 23, 5119-5126.

(89) Banda, S.; Ounaies, Z.; Park, C.; Harrison, J. S., Dynamic Mechanical Analysis of Single Wall Carbon Nanotube Polyimide Composite. *In preparation*, Texas A&M University: 2006.

(90) Watanabe, M.; Yokoyama, M.; Ueda, T.; Kasazaki, T.; Hirai, M.; Hirai, T. *Chemistry Letters* **1997**, (8), 773-774.

(91) Sellinger, A. T.; Deshmukh, S. J.; Ounaies, Z.; Kim, S. N.; Vaia, R. A. Proceedings of SPIE smart structures/NDE San Diego, CA, 2010; pp 1-9.

(92) Hartman Kok, P. J. A.; Kazarian, S. G.; Briscoe, B. J.; Lawrence, C. J. *Journal of Colloid and Interface Science* **2004,** *280*, 511-517.

(93) Harnau, L.; Dietrich, S. *Physical Review E* **2002,** *65*, (021505), 1-5.

(94) Guillot, F. M.; Balizer, E. *Journal of Applied Polymer Science* **2003,** *89*, 399-404.

(95) Cronin, S. B.; Swan, A. K.; Ünlü, M. S.; Goldberg, B. B.; Dresselhaus, M. S.; Tinkham, M. *Physical Review Letters* **2004,** *93*, (16), 1-4.

(96) Cronin, S. B.; Swan, A. K.; Ünlü, M. S.; Goldberg, B. B.; Dresselhaus, M. S.; Tinkham, M. *Physical Review B* **2005,** *72*, (035425), 1-8.

(97) Hadjiev, V. G.; Iliev, M. N.; Arepalli, S.; Nikolaev, P.; Files, B. S. *Applied Physics Letters* **2001,** *78*, (21), 3193-3195.

(98) Newnham, R. E.; Sundar, V.; Yimnirun, R.; Su, J.; Zhang, Q. M. *Journal of Physical Chemistry B* **1997,** *101*, 10141-10150.

(99) Hilczer, B.; Malecki, J., *Electrets*: *Studies in Electrical and Electronic Engineering*; Elsevier: New York, 1989.

(100) Glatkowski, P. J. World Intellectual Property Organization Patent WO 02/076724 A1 2002.

(101) Benedict, L. X.; Louie, S. G.; Cohen, M. L. *Physical Review B* **1995,** *52*, (11), 8541-8549.

(102) Krupke, R.; Hennrich, F.; Löhneysen, H. V.; Kappes, M. M. *Science* **2003,** *301*, 344-347.

(103) Hedvig, P., *Dielectric Spectroscopy of Polymers*; John Wiley and Sons: New York, 1977.

(104) Ounaies, Z.; Park, C.; Wise, K. E.; Siochi, E. J.; Harrison, J. S. *Composites Science and Technology* **2003,** *63*, (11), 1637-1646.

(105) Dean, J. A., Lange's Handbook of Chemistry, 15th ed.; McGraw-Hill: New York, 1999.

(106) Hinkley, J. A.; Dezern, J. F. *Crystallization of Stretched Polyimides: A Structure Property Study*; NASA Langley Research Center, NASA/TM-2002-211418 (2002): 2002.

(107) Siochi, E. J.; Lillehei, P. T.; Wise, K. E.; Park, C.; Rouse, J. H. *Design and Characterization of Carbon Nanotube Nanocomposites*; NASA Langley Research Center: Hampton, VA, 2003.

(108) Banda, S. Electric Field Manipulation of Polymer Nanocomposites: Processing and Investigation of Their Physical Characteristics, Dissertation, Texas A&M University, College Station, 2008.

(109) Harrison, J. S.; Ounaies, Z. *Piezoelectric Polymers*; 2001-43; NASA langley research center: Hampton, Virginia, 2001; pp 1-26.

(110) Young, J. A.; Farmer, B. L.; Hinkley, J. *Polymer* **1999,** *40*, 2787-2795.

(111) Dean, J. A., *Lange's Handbook of Chemistry*. 15th ed.; McGraw-Hill INC: 1999.

(112) Hinkley, J. A.; Dezern, J. F. NASA Langley Research Center CASI (301) 621-0390.

(113) Makowski, M. P. *Computational polymer science* **1993,** *3*, 1-8.

(114) Nalwa, H. S., *Ferroelectric Polymers : Chemistry, Physics, and Applications*. CRC Press: New York, 1995.

(115) Owens, F. J.; Jayakody, J. R. P.; Greenbaum, S. G. *Composites Science and Technology* **2006,** *66*, 1280-1284.

(116) Wise, K. E.; Park, C.; Siochi, E. J.; Harrison, J. S. *Chemical Physics Letters* **2004,** *391*, 207-211.

(117) Su, J.; Harrison, J. S.; St Claire, T. L. IEEE International Symposium on Application of Ferroelectrics, 2000; HI; pp 811-819.

(118) Bormashenko, Y.; Pogreb, R.; Stanevsky, O.; Bormashenko, E. *Polymer Testing* **2004,** *23*, 791-796.

(119) Esterly, D. M.; Love, B. *Journal of Polymer Science: Part B: Polymer Physics* **2004,** *42*, 91-97.

(120) Park, Y. J.; Kang, Y. S.; Park, C. *European Polymer Journal* **2005,** *41*, 1002-1012.

(121) Gregorio, R. J. *Journal of Applied Polymer Science* **2006**, *100*, 4, 3272-3279

(122) Cheng, L.-P.; Lin, D.-J.; Yang, K.-C. *Journal of Membrane Science* **2000,** *172*, 157-166.

(123) Yong, T.-H.; Lin, D.-J.; Gau, J.-J.; Chuang, W.-Y.; Cheng, L.-P. *Polymer* **1999,** *40*, 5011-5021.

(124) Dillon, D. R.; Tenneti, K. E.; Li, C. Y.; Ko, F. K.; Sics, I.; Hsiao, B. S. *Polymer* **2006,** *47*, 1678-1688.

(125) Yu, L.; Cebe, P. *Polymer* **2009,** *50*, 2133-2141.

(126) Ramasundram, S.; Yoon, S.; Kim, K. J.; Park, C. *Journal of Polymer Science: Part B: Polymer Physics* **2008,** *46*, 2173-2187.

(127) Gregorio, R. J.; Cestari, M. *Journal of Polymer Science: Part B : Polymer Physics* **1994,** *32*, 859-870.

(128) Hasegawa, R.; Takahashi, Y.; Chatani, Y.; Tadokaro, H. *Polymer Journal* **1971,** *3*, (5), 600-610.

(129) Takakubo, M.; Teramura, K. *Journal of Polymer Science: Part A: Polymer Chemistry* **1989,** *27*, 1897-1905.

(130) Sasabe, H.; Saito, S.; Asahina, M.; Kakutani, H. *Journal of Polymer Science: Part A-2* **1969,** *7*, 1405-1414.

(131) Yano, S. *Journal of Polymer Science: Part A-2* **1970,** *8*, 1057-1072.

(132) Imamura, R.; Silva, A. B.; Gregorio, R. J. *Journal of Applied Polymer Science* **2008,** *110*, 3242-3246.

(133) Prest, W. M. J.; Luca, D. J. *Journal of Applied Physics* **1975,** *46*, (10), 4136-4143.

(134) Hasegawa, R.; Kobayashi, M.; Tadokaro, H. *Polymer Journal* **1972,** *3*, (5), 591-599.

(135) Salimi, A.; Yousefi, A. A. *Journal of Polymer Science: Part B: Polymer Physics* **2004,** *42*, 3487-3495.

(136) Gregorio, R. J.; Capitao, R. C. *Journal of Materials Science* **2000,** *35*, 299-306.

VITA

Name:	Sujay Jaysing Deshmukh
Address:	Department of Aerospace Engineering, H. R. Bright Building, Rm 701, Ross Street- TAMU 3141, College Station, TX, 77843-3141
Email Address:	Sujay.deshmukh@gmail.com
Education:	B.E., Mechanical Engineering, University of Pune, 2003 M.S., Aerospace Engineering, Texas A&M University, 2006